Design and Fabrication of an Inflation-activated FPCB MEMS-based Electrode for Bio-signal Recording with an In-canal Fixation Capability

by

Ehsan Ranjbar

A thesis presented to the Faculty of Graduate Studies
in fulfillment of the thesis requirements for the degree of

Master of Science

Biomedical Engineering Program,
Department of Electrical and Computer Engineering,
University of Manitoba
Winnipeg, Manitoba, Canada 2024

Copyright © 2024 by Ehsan Ranjbar

Abstract

This research aims to propose a design and fabrication process for a novel miniaturized electrode which can be potentially exploited to record EVestG signals and ear electrical activity from the middle inner parts, including semicircular canals and otolith organs, by an extra-tympanic electrode. This thesis covers EVestG signal recording, its currently used electrode, and the associated current challenges, followed by a review of micro-fabrication techniques, including Micro Electro Mechanical Systems (MEMS) conventional fabrication techniques (sputtering), 3D-printing micro-fabrication technologies (Stereo-lithography or SLA), and Bio-MEMS electrode fabrication for new electrodes design with their associated technical challenges. It also presents some methodologies to cope with the challenges in our design, studying their feasibility. Then, it adopts one of the presented methodologies, which seem more feasible regarding our accessible facilities and resources. The methodology was chosen for a new needle-electrode design (potentially for EVestG recording) and it was fabricated using various technologies such as air-actuation using medical balloons, Flexible Printed Circuit Board (FPCB), 3D-printing, and MEMS fabrication. The fabrication process, from basic steps to the latest developments, is reported illustratively. Finally, the performance of the designed and fabricated micro-needle electrodes from impedance against pressure variation is investigated via some in-vitro experiments. The experiments demonstrate impedance reduction of the fabricated plastic silver-sputtered SLA-3D-printed micro-needle electrodes as the pressure increases.

Acknowledgements

I want to thank my advisors, committee members, parents, and all my family members who supported me along the way to achieve my academic aims. I am grateful and thankful to work under my advisors' and co-advisors' supervision. I appreciate all their advice. I also thank all my committee members' guidelines and comments.

Notice:

It should be stated that the proposed electrode design, application, and fabrication procedures presented and discussed in this thesis are just experimental and have not been confirmed medically safe, standard and commercial, and have not been approved by any medical or standard organizations.

Contents

Abstract i

Acknowledgements i

List of Figures xviii

List of Tables xix

List of Symbols xxi

1 Introduction 1

1.1 Motivation 3

1.2 Objective 4

1.3 Thesis organization 5

2 Background 7

2.1 Bio-MEMS electrode microfabrication 7

2.2 Fabrication technologies and tools 21

2.2.1 Sputtering 21

2.2.2 3D-printing 24

2.2.3 Medical balloons 26

2.3 EVestG signal 28

2.4 Currently-used EVestG electrode 30

3 Methodology **37**

3.1 Problem statement 37

3.2 Ideal conceptual schematic solution of an inflatable electrode unimplemented methodology 39

3.3 Simplifying the ideal scheme of the inflatable electrode unimplemented methodologies 42

3.4 Development of the tip of the unactuated cottonwool electrode 53

3.5 Final practical adopted methodology to be implemented 58

4 Fabrication and experimental set-ups **60**

4.1 FDM/SLA 3D-printing of different basic plastic electrode models . . 60

4.2 Fabrication of wired copper-plate (disc) electrodes and their assembly on the Foley balloon catheter 64

4.3 Modification of the unactuated electrode tip 68

4.4 Assembly of the FPCB electrode on the Foley balloon catheter 69

4.5 Assembly of the FPCB electrode on the PTCA balloon catheter . . . 70

4.6 Assembly of FPCB, copper-plate and ball electrodes over pediatric/neonatal Foley balloon catheter and camera at its tip 70

4.7 SLA 3D-printing of micro-needle electrode and its conductive/metal coating 72

4.8 Fabrication of Foley balloon catheter-based electrodes with various μEl configurations 74

4.9 Measurement of the impedance of micro-needle electrodes vs balloon pressure variation 76

5 Results and discussion **115**

6 Future research directions **124**

References **133**

List of Figures

2.1 A block diagram of an integrated bio-instrumentation system. 11

2.2 Different shapes of balloons: (a) Standard (b) Square (c) Spherical (d) Elliptical (e) Canonical (f) Stepped (g) Dog bone (h) Peanut (i) Tapered (j) Offset (k) Canonical spherical (l) Spherical-square. (m) Geometrical parameters of a typical balloon. 28

2.3 Hearing and balance system physiology: (a) Sound energy is transmitted to the perilymph, tectorial membrane, cilia, and mechanical-gated channels of hair cells, generating an AP. (b) Angular momentum moves the endolymph, bending the cupula inside the Ampullae in different directions with various strengths, producing an AP by the hair cells in the cupula. 31

2.4 (a) and (b) Current state-of-the-art EVestG electrode and its different components. (c) Embedment of the active and passive electrodes within the middle ear canal. 34

2.5 (a) Bottlenecks in EVestG recording using the current electrodes, (b) A conceptual schematic immature solution for EVestG recording to over come the bottlenecks. 35

2.6 (a) and (b): A sample EVestG field potential and frequency spectrum. 36

3.1 Trend of investigation of different methodologies, from a basic ideal immature methodology to more implementable ones, leading to a practical solution, regarding our accessible facilities and resources. . . 38
3.2 Conceptual schematic design of a MEMS-based miniaturized recording system including two major parts: 1) Disposable electrode, 2) Control, actuation and measurement circuitry. 40
3.3 Three stages of embedment of the disposable electrode into the canal. 41
3.4 Fabrication process of the electrode pads on a flexible polyamide substrate. The polyamide substrate is supposed to be embedded on a PDMS/Silicone/Latex/Polyethylene/Nitrile/rubbery adjustable (yellow) holder or balloon in Fig. 2.5b. 43
3.5 Active electrode: the geometrical dimensions and cross-sectional views illustrate three layers of the electrode including Polyamide, Copper, and Gold/Nickel. 44
3.6 Passive electrode: the geometrical dimensions and cross-sectional views are presented. 45
3.7 Application of 3D-printing technology to build the active and passive electrodes; the conductive (metal) and non-conductive (non-metal) parts of the active and passive electrodes can be 3D-printed by PBF or DMLM and SLA technologies, and be assembled afterwards. 46
3.8 Conceptual schematics of a simplified solution for an electrode design with in-canal fixability and impedance reduction capability. The picture shows its future potential for EVestG recording; the active and passive electrodes are mounted (adhered to) around the medical balloon to contact with A and B points, respectively, when the balloon inflates. 47

3.9 Application of (silver-droplet ink-jet) 3D-printing technology to build the active electrode; the attachment of polyamide substrate over the balloon membrane is challenging. 48
3.10 The electrode surface in contact with the canal can possibly be assumed to be a cylindrical shell with a length of 4 mm and a radius of 3.5 mm. The radius is half of the ear canal diameter. 48
3.11 (a) A network of in-plane vertically and horizontally connected metal pads to increase flexibility, contact area and decrease fracture chance. The distribution enhances contact when the canal surface has roughness or corrugation. (b) and (c) Copper tracks connect the pads length and width-wise, respectively. 50
3.12 Conceptual schematics of electrode pads ring. The electrode pads strip is wrapped around the balloon. It is made up of polyamide substrate, copper tracks, copper pads, and gold/nickel pads. The pads are connected with copper tracks and are distributed in 360° to contact the canal circumferentially. 51
3.13 Conceptual application design of a balloon catheter for the electrode signal acquisition, using electrode pads ring. 51
3.14 PPCB: metal is sputtered/3D-printed on the copper pad and track. In sputtering, the metal bumpy surface is fabricated over a silicon/plastic structural layer. The metal bump contacts the canal when the balloon inflates. The rectangular/circular pad area is 7.33 mm^2. (a) and (b) Sputtering, (c) and (d) 3D-printing. 52
3.15 Process design of a MEMS micro-needle based on conventional techniques of photolithography, silicon wet etch and sputtering. The height value is just a typical one and not designed nor calculated. . . 53

3.16 Micro-fabrication process of doped silicon discs without SiO_2 etch stop layer which is not time-efficient nor cost-efficient due to mm etch depth. 54
3.17 Micro-fabrication process of doped silicon discs with SiO_2 etch stop layer which is not time-effective nor cost-effective because of mm etch depth. 55
3.18 Micro-fabrication process of copper discs which is not time-efficient nor cost efficient due to mm etch depth of copper. 56
3.19 Fabrication process of PDMS metal-covered discs. 57

4.1 Plastic 3D-printed models: (a) Our lab FDM 3D-printer and (b) its printed models, (c) FDM 3D-printer in the Fabrication shop and (d) its printed models, (e) SLA 3D-printer in the Fablab and (f) its printed models. All these printed models are our attempts to build models similar to the active electrode in Fig. 3.5. 61
4.2 Different filaments: (a) PLA, (b) TPU. They show rigidness and flexibility characteristics, respectively 62
4.3 (a) to (g): PLA FDM 3D-printed pyramidal and conic micro-needles. (h) Comparison between TPU and PLA micro-needles; PLA 3D-printed features better than TPU ones. 63
4.4 Trying to FDM-3D-print micro-needles on flexible TPU; the results are not satisfactory even after changing parameters while converting STL file to G-code. Some of the pictures are the same and presented from different light angles to enhance illustration. Some are pyramidal, conic, and dots. Different sizes have been also tried. 65

4.5 FDM 3D-printed pyramidal micro-needles with a base of 4 mm by 4 mm after setting the parameters in the process of conversion of STL file to G-code. (a) Before trimming under microscope (b) Trimming under microscope. (c) After trimming. (d) The result of bad setting of parameters in the file conversion process. 66
4.6 SLA 3D-printed pyramidal micro-needles with a base of 4 mm by 4 mm. 66
4.7 Fabrication process of an electrode using copper (Cu) plate (disc) and Foley balloon catheter: (a) Equipment for cutting tiny Cu plates. (b) Cu-plate electrode with an area of 4 mm by 4 mm and thickness of 0.52 mm. (c) Cu-plate electrode soldering to the wire. (d) 14 fr-size Foley balloon catheter. (e) to (g) Assembly of the electrode on the balloon. (h) to (i) Soldering Cu-plate electrode onto the middle of the wire. (j) and (k) Cu-plate electrode assembled over the balloon. (l) and (m) Inflation of the balloon. 79
4.8 14 fr-size balloon catheters equipped with copper-plate wire electrodes. 80
4.9 (a) to (g) Fabrication of approximate ear canal models with different sizes to test the Foley balloon catheter-based electrodes: (h) Approximate ear canal FDM 3Dprinted models. 80
4.10 Test of the copper-plate (disc) electrode assembled over the Foley balloon catheter inside the approximate ear canal model. 81
4.11 (a) and (b) FPCBs designed in KiCad. (c) Fabricated FPCBs each with a contact square pad of 4-by-4 mm. (d) to (g): FPCB electrode; development to the current electrode. (h) and (i): Comparison between the FPCB-tipped electrode and the cotton-wool-tipped electrode. (j) and (k): Design of double-sided round-shape electrodes in KiCad with different areas. 82

4.12 Sputtering silver over the copper balls to be used as a new tip for the unactuated silicone-tube wire electrode. 83
4.13 Development to the tip of the unactuated silicone-tube wire electrode (copper/silver ball tip) and its placement inside the FDM 3D-printed approximate ear canal model. 83
4.14 (a) and (b) Development to the tip of the unactuated silicone-tube wire electrode (double-sided FPCB tip) and it placement inside the FDM 3D-printed approximate ear canal model. (c) and (d) Placement of the unactuated silicone-tube wire cotton-wool electrode inside the FDM 3D-printed approximate ear canal model. It is voluminous due to not being gel-smeared. 84
4.15 (a): Resistance of the electrolyte gel. (b): Input-output signal of the gel. (c) to (d): Input-output signal for the FPCB electrode. (e) to (f): Input-output signal for the copper and silver ball electrodes. (g) to (h): Input-output signal for the cotton-wool electrode. 84
4.16 Frequency response of the FPCB electrode. 85
4.17 Frequency response of the ball electrodes: (a) to (c) copper ball electrode, (d) to (g) silver ball electrode. The output sinusoidal waveform is not noisy nor attenuated. 85
4.18 Frequency response of the cotton-wool electrode. The output sinusoidal waveform is noisy and attenuated. 85

4.19 (a) Glue used for sticking the FPCB electrode over the balloon. (b) Assembly of the FPCB electrode over the balloon using the glue. (c) to (e): Problem of the glue curl-up. (f): Testing the FPCB electrode inside the approximate ear canal model. (g) Balloon deformation due to usage of different kinds of glue. (h) Sticking the FPCB over the balloon using tape. (i), (j), and (k) Sticking the FPCB electrode over the balloon using elastic band (or ligature). 86

4.20 (a) Cutting the balloon catheter tip. (b) to (f) Using double-sided glue tape for assembly of the FPCB electrode over the balloon and its status while inflated and deflated. (g) Balloon status after multiple inflation and deflation, using double-sided glue tape. 87

4.21 Assembly of the FPCB electrode over a PTCA balloon catheter. . . . 87

4.22 (a) to (d) Assembly of the FPCB electrode over a 6 fr-size balloon catheter. The catheter tip should be cut very carefully not to damage the inflated balloon. FPCB trimming and cutting of the catheter tip are suggested to be done under microscope. 88

4.23 Cutting the FPCB under the microscope to trim the size for passive and especially active electrodes. 88

4.24 (a) to (c) 3D-printing a camera head to check if it will be accommodated inside the catheter tube. (d) to (g) Putting the 3D-printed camera head model inside the catheter tube. The actual camera, which is suggested for being put inside the catheter tube, can be OVM6948 image sensor. The cross sectional size of its cubic structure is 0.65 mm by 0.65 mm which can be accomodated by the catheter tube. 89

4.25 Fabrication of the electrode using a 6 fr-size silicone Foley balloon catheter with a round ball active electrode at the tip and an FPCB electrode as the passive electrode touching the canal. 89
4.26 Assembly of the copper-plate (Cu-disc) electrode over the FPCB electrode to increase the electrode height. 89
4.27 Painting plastic SLA-3D-printed micro-needles: (a) Silver conductive paint used, (b) to (d) Building a painting chamber, (e) SLA 3D-printed micro-needles, (f) and (g) Painted micro-needles inside the chamber. (h) Silver paste not used for our painting. 90
4.28 (a) SLA-3D-printed micro-needles with smaller size; (b) and (e) with a base of 4 mm by 4 mm, (c) and (d) with a base of 2 mm by 2 mm. 90
4.29 Digram of SLA-3D-printed micro-needles with smaller size; (a) and (b) with a square base of 2 mm by 2 mm. The height changes from 0.1 to 1 mm with an step of 0.1 mm. There are some other taller microneedles just for later testing of 3D-print quality. (c) and (d) with a square base of 4 mm by 4 mm. The height of microneedles are 0.5, 0.75, 1, 1.5, and 2 mm. (e) Pyramidal structure with the height of 2 mm on a square base of 2 mm by 2 mm. 91
4.30 Diagrams of the microneedles and other electrodes used in the experiments discussed in the next chapter. 92
4.31 Silver-sputtering of the plastic SLA-3D-printed pyramidal micro-needles. 93
4.32 Silver-sputtering of the plastic SLA-3D-printed conic and pyramidal microneedles. (a) to (c) Micro-needles inside the sputtering chamber, (d) to (i) 4 mm and 2 mm square micro-needles after sputtering. . . . 94

4.33 8 fr-size latex Foley balloon catheters equipped with different types of electrodes: (a) to (d): Using fibre optic strands, ball tip and FPCB electrodes. (e) to (g): Electrode with double FPCB and a camera-like head inside the tube. (h) to (k): Electrode with double side FPCB and ball tip. (l) to (n): Using ball tip and FPCB electrodes as active and passive electrodes. 95

4.34 8 fr-size latex Foley balloon catheters equipped with different types of electrodes and various configurations: (a) to (d): Using three ball tips and FPCB electrode as active and passive electrodes. (e) to (h): Using two ball tips and FPCB electrode as active and passive electrodes. (i) to (l): Using single ball tip and FPCB electrode as active and passive electrodes. 96

4.35 8 fr-size latex Foley balloon catheters equipped with different types of electrodes and various configurations: (a) to (d): Using two ball tips and FPCB electrode as active and passive electrodes. (e) to (j): Using three ball tips and FPCB electrode as active and passive electrodes. . 97

4.36 6 fr-size silicone Foley balloon catheters equipped with different types of electrodes and various configurations: (a) to (e): Using one single FPCB electrode as active electrode. (f) 3D-printed LED chamber. (g) to (k): Using three ball tips and FPCB electrode as active and passive electrodes. 98

4.37 6 fr-size silicone Foley balloon catheters equipped with different types of electrodes and various configurations: (a) to (d): Using one ball tip and FPCB electrode as active and passive electrodes. (e) to (h): Using two ball tips and FPCB electrode as active and passive electrodes. (i) to (m): Using one ball tip and FPCB electrode as active and passive electrodes. 99

4.38 6 fr-size silicone Foley balloon catheters equipped with different types of electrodes and various configurations: (a) to (d): Using three ball tips and FPCB electrode as active and passive electrodes. (e) to (i): Using one ball tip and FPCB-Cu-plate electrode as active and passive electrodes. (j) to (n): Using one ball tip and FPCB electrode as active and passive electrodes. 100
4.39 6 fr-size silicone Foley balloon catheters equipped with different types of electrodes and various configurations: (a) to (e): Using cotton-wool tip and FPCB electrode as active and passive electrodes. (f) to (g): Using two ball tips as active electrode. 101
4.40 8 fr-size latex Foley balloon catheter equipped with different types of electrodes: (a): Micro-needle attachment over the FPCB. (b) and (c): The Foley balloon catheter is equipped with three different kinds of active electrodes. 101
4.41 Dual-balloon two-way Foley catheter equipped with active and passive FPCB electrodes. 102
4.42 (a): Hydration of the skin phantom. (b) to (l): DC measurement (resistance measurement) of the FPCB electrode when the volume of the catheter balloon is increased. They are sequential read-outs at different times. 103
4.43 (a) to (b) Using silver epoxy for attachment of micro-needles on FPCB. (c) to (i) Sample micro-needles attached via silver epoxy on FPCB electrodes. 104
4.44 Main tools and experimental setup for measurement of impedance variation of the electrodes vs pressure change (both AC and DC measurements). 105
4.45 Checking the skin phantom frequency response. 105

4.46 FPCB electrode impedance variation vs pressure change (thin structure with a sqaure base of 4 mm by 4 mm and a height of almost zero). 106
4.47 FPCB electrode impedance variation vs pressure change (thin structure with a sqaure base of 4 mm by 4 mm and a height of almost zero). 106
4.48 FPCB electrode impedance variation vs pressure change (thin structure with a sqaure base of 4 mm by 4 mm and a height of almost zero). 107
4.49 Copper-plate electrode impedance variation vs pressure change (cubic structure with a sqaure base of 4 mm by 4 mm and a height of 520 μm).107
4.50 Variation of micro-needle electrode impedance vs pressure change (cone structure with a base radius of 0.5 mm and a height of 1.5 mm). 108
4.51 Variation of micro-needle electrode impedance vs pressure change (cone structure with a base radius of 0.75 mm and a height of 1.5 mm). 108
4.52 Variation of micro-needle electrode impedance vs pressure change (cone structure with a base radius of 0.5 mm and a height of 0.75 mm). 109
4.53 Variation of micro-needle electrode impedance vs pressure change (pyramid structure with as square base of 4 mm by 4 mm and a height of 2 mm). 109
4.54 Variation of micro-needle electrode impedance vs pressure change (cone structure with a base radius of 0.75 mm and a height of 0.9 mm). 110

4.55 Variation of micro-needle electrode impedance vs pressure change (cone structure with a base radius of 0.4 mm and a height of 1.5 mm). 110
4.56 Variation of cotton-wool electrode impedance vs pressure change (an ellipse with diameters of 2.5 and 6 mm). The electrode contact with the phantom is enhanced by increasing the inflated balloon pressure. . 111
4.57 Cotton-wool electrode impedance in different frequencies without applying any pressure. The electrode is fixed on the phantom with visually complete contact via a sticking plaster. It is not subjected to the varying balloon pressure. No increasing pressure (inflated balloon) is applied here in this experiment. 111
4.58 Variation of micro-needle electrode impedance vs pressure change (thin structure with a sqaure base of 4 mm by 4 mm and a height of almost zero). 112
4.59 Variation of micro-needle electrode impedance vs pressure change (cone structure with a base radius of 0.5 mm and a height of 1.5 mm). 112
4.60 Variation of micro-needle electrode impedance vs pressure change (cone structure with a base radius of 0.75 mm and a height of 1.5 mm). 113
4.61 Variation of micro-needle electrode impedance vs pressure change (cone structure with a base radius of 0.5 mm and a height of 0.75 mm). 113
4.62 Variation of micro-needle electrode impedance vs pressure change (cone structure with a base radius of 0.4 mm and a height of 1.5 mm). 114

6.1 Concept of a simulation platform for EVestG electrode testing inside the ear canal models. 126
6.2 (a) Reconstruction of a signal via a CSV file from an AWG: the data can be sent to the AWG via a flash memory disc or a LAN port from the computer (MATLAB). A noisy EVestG signal can be generated by MATLAB (Fig. 6.2b), converted to CSV (Fig. 6.2c) and sent to AWG. 126
6.3 Schematic block diagram of an integrated amplifier-electrode circuit on a single FPCB to reduce noise and enhance CMRR. 127
6.4 Circuits of the block diagram in Fig. 6.3 including AD524 instrumentation amplifier, high pass filter, low pass filter, and notch filter. We may recommend AD844 or AD829 op-amps for building the filter circuits as well as secondary stage gains/buffers, regarding low noise, low offset, great slew rate and high bandwidth. 128
6.5 IR send/receive obstacle detection/sensing circuit. 130
6.6 SLA 3D-printed molds with cut-extruded half spheres and drilling holes to make holes inside the balls. 131
6.7 Schematics of application of SPCB and flexible micro-needles to reduce glue usage and decrease glue curl-up. 131
6.8 Diagram of the shielded unactuated tube-wise electrode for reducing noise (cross-sectional view). 132

List of Tables

2.1 ECG/EEG/ECoG/EMG MEMS electrode fabrication: current state-of-the-art. 22

3.1 Values of the geometrical parameters for a typical balloon design (displayed in Fig. 2.2m): they are suggested for electrode actuation purposes, regarding the canal geometry (7 mm in diameter and 2.5 cm in length) and electrode sets dimensions in Fig. 3.5 and 3.6. One design question can be stated as how the radial and axial stresses, as well as burst pressure, function in the constrained parameters and material characteristics. 49

List of Symbols

σ_r	Radial stress
σ_l	Axial stress
p	Balloon pressure
P_b	Balloon burst pressure
d	Balloon diameter
t	Balloon thickness
T_{rs}	Radial tensile strength
$Area$	Electrode area
s	Arc length
l_c	(Electrode) Cylinder length
r	Canal radius
d_c	Canal diameter
θ	(Electrode) Sector in radian
V_{in}	Input voltage
R_e	Electrode interfacing resistance in the experiment
R_2	$1\,k\Omega$ resistor
i	Electrode current
V_1	Input voltage
V_2	$1\,k\Omega$ resistor voltage
$\lvert Z_e \rvert$	the absolute value of the electrode interfacing impedance
f	Input voltage frequency in Hz

R	Resistance (of a typical electrode)
ρ	Resistivity (of the electrode)
l	(Electrode) Resistor length
A	(Electrode) Resistor area
C	(Electrode) Capacitance
ϵ_0	Vacuum permittivity
ϵ_r	Relative permittivity
d_{cap}	Capacitor plates distance (in association with the electrode)
A_{cap}	Capacitor plates area (in association with the electrode)
ω	Frequency in rad/sec
Z	(Electrode) Impedance
X_c	(Electrode) Reactance
d	Balloon inflated diameter
L	Electrode mounting length over the balloon
L_t	Balloon total length without considering balloon necks
L_{pn}	Balloon proximal neck length
L_{dn}	Balloon distal neck length
β	Balloon canonical angle
d_{ip}	Internal diameter of the proximal neck of a balloon
d_{ep}	External diameter of the proximal neck of a balloon
t_{pn}	Wall thickness of the proximal neck of a balloon
t_{dn}	Wall thickness of the distal neck of a balloon
d_{id}	Internal diameter of the distal neck of a balloon
d_{ed}	External diameter of the distal neck of a balloon
t_{eb}	Thickness of the expandable body of a balloon
El	Electrode
fr	French size; 1 fr = $\frac{1}{3}$ mm

Cu	Copper
Ni	Nickel
Au	Gold
Al	Aluminum
Si	Silicon
Pt	Platinum
Ti	Titanium
Cr	Chromium
$PtCl$	Platinum chloride
Ag	Silver
$AgCl$	Silver chloride
IrO_x	Hydrated oxohydroxide of Iridium
SiO_2	Silicon oxide
Si_3N_4	Silicon nitride
HF	Hydrofluoric acid
KOH	Potassium hydroxide
SU-8	A commonly used epoxy-based negative photoresist
PEDOT:PSS	Poly(3,4-ethylenedioxythiophene) polystyrene sulfonate
MWCNTs	Multi-walled carbon nanotubes
HNA	Acidic mixture of hydrofluoric, nitric, and acetic attacking silicon
DI	Deionized or Demineralized (water)
PDMS	Polydimethylsiloxane; a biocompatible elastomer
IPA	Isopropyl Alcohol
EDOT	Ethylenedioxythiophene (organosulfur compound)
PSS	Polystyrene sulfonate
CHF_3	Fluoroform (trifluoromethane) for plasma etching of SiO_2 and Si_3N_4
γ-MPS	γ-methacryl-oxypropyl-trimethoxysilane (adhesion promoter)

S_c	Area of conic microneedle electrode
S_p	Area of pyramidal microneedle electrode
S_{cw}	Area of elliptic cotton-wool electrode
a_s	Length of the base square side
n_m	Number of the cones in a microneedle electrode
r_m	Cone base radius in a microneedle electrode
h_m	Cone height in a microneedle electrode
h_p	Pyramid height in a microneedle electrode
a_{cw}	Ellipse minor axis diameter
b_{cw}	Ellipse major axis diameter

1

Introduction

Nowadays, non-invasive electrophysiological measurements are common, safe and relatively cheap. Some well-known ones include Electro-cardiography (ECG) for monitoring/diagnostics of the cardiac muscle, Electromyography (EMG) for measurement of muscle electrical activity in response to its nerve stimulation, Electroencephalography (EEG) for detection of brain electrical activity, and Electroretinography (ERG) for detecting function of the retina, photo-receptors (rods and cones), and light and ganglion cells. The frequency range of the signals is between 0.01 to 10 kHz, while their amplitudes span from μV to mV. These measurement systems mainly comprise three parts: electrodes (signal transducers), instrumentation electronic circuits, and hardware/software filtering/signal conditioning/signal-processing-and analysis tools. As probably the most crucial part and the first intermediate touching the human body or bio-tissue, the electrodes may usually be built or enhanced by MEMS micro-fabrication technologies.

Bio-MEMS are MEMS used in medical/biological applications or are devices which have medical/biological/physiological functions. As an example, one may refer to three famous commercialized Bio-MEMS applications as follows: 1)

An insulin level monitoring and control device including a micro-pump, micro-needle, and glucose sensor; 2) A pacemaker including a MEMS accelerometer to detect movements of cardiovascular walls; 3) A cochlea implant which comprises microphone, processor, transmitter, receiver and micro-electrode array implanted in the cochlea.

It is worthwhile mentioning that the Bio-MEMS can be applied topically, in-vitro, or in-vivo. One may prepare a vast categorization of Bio-MEMS as follows: Drug synthesis, Drug delivery, Nano-surgery, Nano-therapy, Genome synthesis, Diagnostics, Medical actuators and sensors, Artificial organs and implants, Bio-compatible materials, Bio-micro-fluidics, Lab-on-a-chip (LOC), Organ-on-a-chip (OOC), Biochips, Pinch flow fractionation, Micro mixer, Electro-osmosis (EO) Micro pumps, Particle separation, Tissue level, Gene level, Enzyme level, Single-cell analysis, Stem cell, Biochemical separation, Micro-electrodes and micro-needles: Electrical stimulation, Brain deep stimulation, Neurotransmitter modulation and micro-signal sensing at the cell level: Organic Electronic Ionic Pump (OEIP) technology, Complementary Metal-oxide Semiconductor (CMOS) bio-technology, Organic transistors, and Bio micro cantilevers. In most of these devices and applications, micro-electrodes function as transducers to transform biological signals into electrical signals and vice-versa, significantly affecting the whole device's performance.

The MEMS micro-fabrication technologies are exploited to build Bio-MEMS, such as bio-signal recording electrodes or enhance their properties. A bio-electrode is a conductor that is designed to serve as an interface between biological structures and electronic systems. Its function is to either sense and measure the electrical activity within the biological structure (passive micro-function) or stimulate it by inducing external electrical potential (active micro-function) [51]. We may need bioelectrodes that are hundreds to tens of micrometeres or hundreds of nanometers in

size, called Bio-MEMS electrodes. We may even apply a MEMS fabrication process to bio-electrodes (especially on their contacting surface), whose size is measured in millimetres, to enhance biological and electrical contact properties.

1.1 Motivation

The measurement systems mentioned above, ECG, EMG, EEG, and ERG, are used to diagnose cardiac disorders, neuromuscular system diseases, brain seizures, and visual system ailments, respectively. In addition to these types of diseases, neurological disorders also grow more problematic nowadays, causing a considerable percentage of total deaths around the world, and we may suffer from negative impacts soon regarding lifestyle complexities.

Given the above challenge, there is a considerable need to design and fabricate medical devices and hardware-software diagnostic tools for data acquisition and the characterization of neurological responses and bio-signals. Cochlear and vestibular electrical activity may represent clues for diagnosing some neuro-degenerative diseases. The technique for recording cochlear electrical activity brought about by acoustic stimulus is called Electrocochleography (ECOG). In contrast, the method for recording electrical activities of vestibular organs caused by a whole body-tilt stimulus is called Electrovestibulography (EVestG) [42, 63, 8]. ECOG is primarily applicable for Ménière's Disease (MD) diagnostics [64, 90], while EVestG suits the diagnosis of Parkinson's Disease (PD) [27, 28], Depression [39] and Schizophrenia [42]. Similar EVestG applications are found and discussed in [34, 88, 89]. But what are the main functions and applications of the intricate EVestG signal? We can measure the nerve function by addressing the signal features and comparing it with a healthy model. It can lead to the diagnosis of nerve disorders such as Depression, Schizophrenia, PD, and MD.

The benefits of EVestG analysis can include low cost, simplicity/quickness in diagnosis, early diagnosis before noticeable symptoms, the establishment of an early treatment process, more accuracy and biological feedback in drug prescription, decrease of the burdens over the health system, applicability as a confirmation tool for effectiveness of therapies, e.g., repetitive Transcranial Magnetic Stimulation (rTMS), and usability by a medical technologist. An efficient EVestG recording system can analyze neurological disorders qualitatively and possibly quantitatively.

The set of tools for EVestG signal acquisition chiefly go as follows: 1) Electrodes placed in the ear canal near the Tympanic Membrane (TM), 2) Bio-instrumentation amplifiers and digitalization tools, 3) Multi-axis tilting chair which accommodates the patient and generates movement stimulation, and 4) Computer and analysis software. Regarding the existence of a mature bio-instrumentation system and great software developments, it seems that some enhancements to the currently used EVestG electrode are required as part of the whole system optimization. Although we do not present implemented solutions for those enhancements here in this thesis, they are briefly mentioned in Chapters 2 and 3 to clarify more where our motivation originated from during our early stages of research. The part that we are concerned with in this thesis is the design of an electrode with an in-canal fixability that might be potentially used in the future after further modification for bio-signal recording from the ear canal. It may enhance the electrode's electrical contact with the canal while subjected to the chair movement in the future.

1.2 Objective

This thesis aims to design and fabricate a miniaturized electrode that might be used for EVestG recording in the future. First, we propose some conceptual schemes and development designs to an electrode that can be used for bio-signal recording from

a canal, probably similar to an ear canal. Later, we discuss the defects with the proposed schemes and designs (initial and immature methodologies), and then we aim to opt for a more feasible and evolved methodology. To achieve this objective, we review micro-fabrication techniques of Bio-MEMS bio-potential recording electrodes to do a feasibility study and adopt an appropriate solution regarding the tools we have at the access. Our main objective is to design and fabricate some air-actuated electrodes (with inflatable substrate) using medical balloons, Flexible Printed Circuit Board (FPCB) technology, Micro Electromechanical Systems (MEMS) microfabrication techniques (sputtering), and additive manufacturing (3D-printing technology especially stereo-lithography), showing potential conformability, and fixability inside a canal. Finally, we propose to test the impedance performance of the fabricated plastic metal-coated micro-needle (as the significant end-effector of the whole electrode device) vs actuation pressure in in-vitro experiments, demonstrating pressure impact over a reduction of interfacing impedance.

1.3 Thesis organization

We have adopted the following organization for this thesis. While Chapter 1 addressed our motivation and objective, the remaining parts of the thesis are organized as follows: Chapter 2 presents some reviews, including the micro-fabrication of electrodes for recording electro-physiological bio-potentials and their micro-fabrication techniques. It also presents the current electrode structure and the challenges of using it for EVestG signal acquisition. It also briefly discusses medical balloon technology. Chapter 3 discusses the problem and distinct methodologies for fabricating a suitable electrode. Ultimately, it proposes the most feasible solution regarding our research questions, assumptions and accessible facilities. Chapter 4 describes the fabrication path covered, and the experiments carried out to test the

functionality of our built electrodes, presenting experimental results at the end of the chapter. Afterwards, discussion about the results and conclusion are presented in Chapter 5. Finally, Chapter 6 puts forth a short discussion on future research potentials and draws a big picture of future works into one's prospective.

2

Background

In this chapter, we review some papers on fabricating BioMEMS electrodes to record some important and the most used bio-potentials. Then, only the significant processes with which we are concerned in our research and the primary methodologies (discussed in Chapter 3 and adopted in Chapter 4) are reviewed because the microfabrication technologies for building MEMS devices are numerous and well-explained in many references. A review of the fabrication technologies, including sputtering and 3D printing, is followed by a short discussion on medical balloons. At the end of the chapter, a description of the currently-used electrode for EVestG signal recording and an introductory discussion over the problems using it are expressed to inspire us with some hints for designing an electrode which may show some potentials for EVestG application in future, having covered a concise description on auditory/vestibular function and EVestG signal as well.

2.1 Bio-MEMS electrode microfabrication

Early in 2001, Judy [49] reviewed Bio-MEMS, their categories, and their fabrication process. Stieglitz and Gross [87] presented a MEMS fabrication technology to build double-sided multichannel electrodes for neural prostheses and bio-hybrid

systems. They were applicable in micro-devices showing some flexibility in their structures, using polyamide as backside insulation and protection layer. Cheung et al. [18] enhanced neural recording by introducing roughness or nano-structures on the electrode surface, reducing contact impedance. They exploited Reactive Ion Etching (RIE) to build high aspect ratio pillar-like poly-silicon nano-structures. Aziz and Genov [9] fabricated 16x16-El μarray in μV and mV modes for monitoring electrochemical activity equipped with onboard-connected gain amplifiers, tunable filters, sample-and-hold circuits, and A/D converters. Korsmeyer et al. [54] presented a CAD-for-MEMS philosophy, a computer-aided design and analysis methodology for Bio-MEMS development with examples of electrostatic actuation, separation lab-on-a-chip, a digital fluidic processor, on-chip optics, and electro-spray ionization. Chiou et al. [22] fabricated and characterized dry MEMS-based silicon spiked EEG electrode array without conducting gel or scalp preparation. Cheung and Renaud [19] reviewed implantable flexible micro-electrodes embedded in thin-film polymer foils for neural applications and eye pressure measurement. The fabrication process that was discussed was based on the spin-on of polyamide on silicon, metal electrode patterning, and RIE for contact opening and structure definition. Yu et al. [104] proposed a new micro-machined ECG electrode with hollow silicon μ-needles with piercing capability to lower the impedance and no need for skin preparation. Focusing on micro-needle electrode arrays, Paul et al. [77] reviewed advancements in their silicon-based μ-structures, material characterization methods, and mechanical μ-systems. Zargaran Yazd [106] investigated the major constructive blocks required to enhance recorded signal quality from the viewpoint of MEMS and microelectronics. James et al. [91] reviewed μ-electrodes such as neuro-probes and regenerative electrodes for signal recording. Farina et al. [36] micro-fabricated implantable polyamide-based platinum/PtCl electrodes for EMG recordings of the gastrocnemius muscle of rabbits. Lee et al. [58] designed and

fabricated a liquid crystal polymer gold μ-electrode in which platinum and IrO_x could be replaced with gold due to their well-established sputtering techniques for Optical Coherence Tomography (OCT) recording in rabbits. Rajaraman et al. [79] micro-fabricated metal-transfer micro-moulded 3D micro-needle array electrodes for transcutaneous nerve tracking application, demonstrating a better electrode-skin-electrode impedance than standard wet electrodes. Padmaraj et al. [75] presented the design and fabrication process of gold μ-electrode working with Ion Sensitive Field Effect (ISFE) transistors for bio-signal recording in mitochondria medicine. Rubehn et al. [81] designed and fabricated a micro-machined 252-channel Electrocorticography (ECoG) electrode array, which comprised a thin polyamide substrate embedding sputtered platinum electrode spots and conductive tracks. Kim et al. [52] fabricated MEMS ECG electrodes by approaching two methodologies: MEMS conventional fabrication procedures and FPCB, which performed better than commercial ECG electrodes. Chi et al. [20] reviewed dry-contact MEMS ECG electrodes compared to other types, including metal plates, wet-contact gel-based Ag/AgCl, thin-film insulated metal plates, and non-contact metal plates with cotton coupling. Chang et al. [16] designed and fabricated silicon dry MEMS EEG electrodes that are superior to wet electrodes in terms of conductivity, signal intensity, and small dimensions. Ruff et al. [110] developed an EMG μ-electrode whose structure comprised polyamide substrate and platinum metal contact parts and was surgically fixable during implantation. Blau reviewed [13] the latest design advancements in flexible polymer micro-electrode arrays. Jackson et al. [48] proposed a novel movable implantable electrode to record a new set of neurons with a $9\mu m$-resolution displacement, which is especially beneficial while the neural signal deteriorates. Zdanovich [107] developed MEMS glucose cantilever electrodes for in-vivo blood sugar monitoring. Seker et al. [83] reviewed the latest progress in MEMS technologies associated with disease studies and therapeutic solutions. Wang et al.

[99] exploited cutting, isotropic wet-etching and sputtering to build a pyramidal EEG μ-needle electrode for long-term recordings. Wu et al. [102] fabricated a flexible, chemically-stable dry μ-needle EEG electrode with fine shielding, small dimension, easy assembly, good mechanical strength, and painless applicability. Thongpang et al. [93] built a stretchable and flexible 3D-platform of thin film MEMS ECoG electrode array for Brain-Computer Interfacing (BCI) application and epileptic activity monitoring, reducing pressure over the brain and allowing subcranial radial positioning of multiple electrodes from a solitary craniotomy.

A variety of research in Bio-MEMS studies is focused on bio-electrode fabrication for either input (stimulation), output (recording) signalling, or both. More importantly, their building procedures have been chiefly exploiting MEMS conventional fabrication processes, which are not time or cost-effective methods. However, they seem inevitable to a considerable extent in enhancing the bio-electrode properties. The following issues concerning passive bio-electrodes (bio-signal-recording) have required solutions exploiting MEMS fabrication: 1) Bio-compatibility, 2) Low impedance, 3) Conformability, 4) Penetration or implantation, 5) Low noise and high Common Mode Rejection Ratio (CMRR), and 6) Integration with electronics in terms of compatibility and miniaturization (See Fig. 2.1). Regarding our review, bio-electrodes for bio-potential recording may be mainly categorized into the four following types:

1. EMG for recording muscles' electrical activity, which can be non-invasive or invasive,
2. ECG for non-invasive recording of heart electrical activity from the skin of chest, arms, and legs,
3. EEG for non-invasive recording external brain electrical activity from the scalp,
4. ECoG for invasive recording of internal brain electrical activity from the brain cortex.

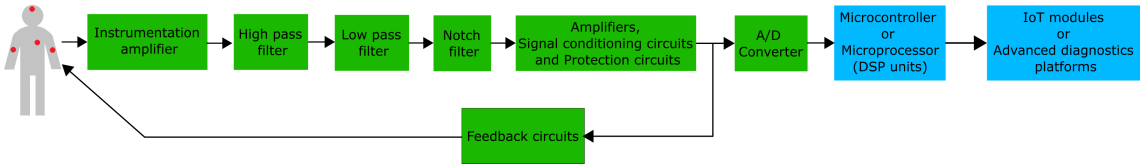

Figure 2.1: A block diagram of an integrated bio-instrumentation system.

Now, we review some articles that are more detailed and narrowly concerned with fabricating bio-electrodes for recording the four biopotentials mentioned above.

Chang and Chiou [17] designed and fabricated silicon metal-coated micro-needles for ECG recording. They did not require conductive gel (dry electrodes) and were capable of penetrating Stratum Corneum (SC) and reaching Stratum Germinativum (SG) layers of the epidermis. The fabricated electrodes showed low-noise and low-power, proposing a chopper-stabilized differential instrumentation amplifier. Their fabrication process stages were based on a two-stage etch process of silicon: isotropic and anisotropic etch: 1) Photolithography to provide etching protection hard mask, 2) Isotropic HNA etch, 3) Anisotropic RIE, 4) Release of the hard mask via wet etch, 5) Titanium/Platinum DC-sputtering technique for high conductivity, 6) Cut-out of electrodes from the silicon wafer, and 7) Mounting electrodes on FPCB using silver glue. Similar topics and approaches were also presented in [16]. The results of the test of the device compared the impedance of the conventional AgCl electrode (accompanied by conductive gel) with the surface-mounted dry (SMD) electrode. SMD electrode demonstrated a considerably low impedance due to penetration into SC and reaching SG [16].

Tseng et al. [95] and wang et al. [97] proposed dry foam electrodes for ECG monitoring systems. The fabrication process included different stages: 1) Electrically polymer conductive foam (urethane) was used. 2) A 200 micron taffeta was used to cover the foam. 3) A 0.2 nm adhesion layer of gold is added to the coverage. 4) Nickel-copper is deposited over the gold layer to make the electrode resemble silver electrode properties [95, 97]. The electrodes were applied to the skin using

an elastic vest belt to test the device. The correlation between the two signals, obtained by wet electrodes and the fabricated foam-based dry ones, was about 98 or 99%. The frequency spectrum demonstrated a low impedance of the foam-based fabricated electrode compared with the conventional ECG wet electrodes. Time duration had less effect on the impedance using foam-based electrodes. The foam-based dry electrodes also showed better robustness against motion artifacts [95, 97].

Hsu et. al [46] designed and fabricated barbed electrodes for monitoring ECG. The design advantages were dryness (no conductive gel usage), sturdier attachment and fixedness, cheapness, and the ability to reach SC and get fixed without bleeding. The fabrication stages were as follows: 1) Adoption of a P-type standard 100 orientation silicon wafer, 2) Deposition of SiO_2/Si_3N_4 over the silicon wafer to make a KOH anisotropic etch mask, 3) Photolithography for patterning SiO_2/Si_3N_4 masks, 4) KOH etch for building pyramidal structures, 5) Removal of the SiO_2/Si_3N_4 mask via HF acid etch, 6) Deposition of SU-8 and patterning it, 7) HNA isotropic etch, 8) Photo-resist removal by Piranha etchant (solution), and 9) Titanium and silver sputtering to enhance the skin contact conductivity. The two electrodes were applied to the skin to test the device using chest pads. The impedance frequency response for the fabricated dry electrode is considerably much better and has lower magnitude compared with the gel-based conventional electrode [46].

Wang et. al [98] presented a flexible MEMS-based capacitive electrode for ECG measurement. Dryness, conductive gel-freeness, bendability, flexibility and conformability with the torso were among the advantages of their design. The fabrication process may be described as follows: 1) Sputtering of chromium and copper over silicon wafer as a seed layer for prospective electroplating, 2) Photo-lithography and patterning to build a photo-resist mold, 3) Electroplating nickel over the copper to fabricate a sensing layer, 4) Deposition of Parylene over the sacrificial photo-resist mold and the nickel deposited layer as an insulation layer against the

active shield, 5) Deposition of copper as a seed layer, 6) Spin-coating of photo-resist and patterning it to build another mold, 7) Electroplating nickel, and 8) Deposition of Parylene as another insulation layer over the active shield. The three electrodes were applied onto the patient's T-shirt via a fixable vest belt to test the device. There was no significant difference between the AC properties of the two signals (P-wave, QRS Complex, T-wave). The only difference was the DC gain between the conventional gel-based and dry fabricated capacitive electrodes.

Kim et al. [52] fabricated flexible PCB-based MEMS ECG electrodes. Two electrodes instead of three were used for ECG recording, which can result in lower cost. Two fabrication processes were designed and implemented: Flex-PCB and Polyamide-based MEMS electrodes. The first one included: 1) Lamination of a negative dry film over a copper layer, 2) UV-exposure and development to build a special underlying pattern of copper, 3) Chemical etching of the copper layer, 4) Development of the dry film mask in acetone, 5) Fabrication of interconnection line on flexible PCB, and 6) Connection of the interconnection lines and the electrodes via a flexible PCB connector. The second process went as follows: 1) Deposition of SiO_2, 2) Deposition of Polyamide resin over SiO_2 and curing it, 3) DC-sputtering of titanium/copper over the SiO_2 layer, 4) Photolithography for subjected and underlying pattern of the copper and titanium layer, 5) Etching of the copper by a mixed solution of phosphoric acid, acetic acid and nitric acid, 6) Etching of titanium by HF acid and DI water, and 7) Etching SiO_2 via HF to release the polyamide structure off the carrier silicon wafer. Flexible PCB-based electrodes and MEMS electrodes were tested in comparison with the 3-electrode configuration. The results were satisfactory, especially for the MEMS electrode. The correlation was so close to 100% for the larger diameter of the electrode (4 mm in comparison with 2 mm and 1 mm) [52].

Mathias et al. [68] developed a non-contact MEMS ECG electrode. It was capable of ECG recording using dry electrode technology without using gel and with the

ability of contact-less bio-potential pick-up in a distance of 500 μm. The fabrication process was intricate, including too many consecutive stages: 1) Cleaning a polyamide substrate, 2) RF-sputtering titanium/copper on polyamide as a seed layer, 3) Negative photolithography to construct a photo-resist mold, 4) Electroplating copper to build a reference copper plate, 5) Etching the titanium/copper layer up to the polyamide layer after building a negative photo-resist mask, 6) Removal of the photo-resist, 7) Deposition of SU-8 as an insulation layer and patterning it, 8) RF-sputtering titanium/copper over the whole product, 9) Deposition of negative photo-resist and patterning it to form a mold, 10) Electroplating copper to build the sensing electrode, 11) Deposition of photo-resist and patterning it to construct a mask for etching titanium/copper seed layer, 12) SU-8 coating and patterning to insulate the sensing electrode, 13) RF-sputtering titanium/copper to build another seed layer, 14) Photo-resist deposition and patterning it to build the mold for electroplating the remainder of the reference electrode, 15) Electroplating copper, 16) Photo-resist removal, and 17) Coating with SU-8 as the insulation. For testing the device, once it was connected to a well-defined simulated ECG and the contact ECG was evaluated, there was no difference between the measured and primary signal. In the second experiment, the two chief electrodes were put inside a cotton pocket which had a thickness of 0.5 mm and the third electrode was tape-attached to the skin. The recordings with the MEMS-designed electrodes were comparable in both simulation and experiment [68].

Yuan et al. [105] proposed a design of elastic dry EEG electrode, which its main advantages were conductive gel-freeness and reduced scalp preparation time. The fabrication process was designed and implemented as follows: 1) Glass substrate cleaning, 2) Sputtering chromium/copper on glass as a seed layer, 3) Photolithography and development to construct a photo-resist structure, 4) PDMS spin-coating over the seed layer to cover around the photo-resist and over the seed

layer as well, 5) Photo-resist removal by acetone to build a PDMS mold mounted over the seed layer, 6) Electroplating copper over the seed layer in the gaps to form the vias, 7) Sputtering chromium/copper over the PDMS and copper via structures, 8) Deposition of photo-resist and patterning it to build a mold for patterning wires, 9) Electroplating thin layer of copper to construct the wires, 10) Photo-resist removal by acetone, 11) Deposition of photo-resist and patterning it to build a mold for the subsequent electroplating over the copper wires, 12) Electroplating nickel rods as the standing piercing parts of the electrode array, 13) Electroplating gold over the nickel, and 14) Photoresist removal by acetone. Test results demonstrated similar characteristics of the signals obtained by conventional wet electrodes and the dry fabricated electrodes [105].

Arai et al. [7] fabricated a polymer-based dry EEG electrode. Some of their main design advantages were no conductive gel usage, penetration to SC, low impedance and time-reduced scalp preparation in EEG recording. Their fabrication process goes as follows: 1) Negative SU-8 photolithography, patterning and development by Fresnel diffraction of UV light to build an SU-8 mold, 2) Spin-coating PDMS over the SU-8 mold, curing and peeling off the mold to create a PDMS micro-needle, 3) Coating PDMS with Parylene-film as a release layer, 4) Spin-coating PDMS over the PDMS micro-needle and curing it to build a hollow pyramidal mold of PDMS for SU-8 micro-needle casting, 5) Spin-coating PDMS mold with SU-8 photo-resist, 6) SU-8 exposure and hardening, 7) Peeling off PDMS mold, 8) Sputtering silver over the SU-8, 9) Deposition of nano-porous Parylene over the silver layer to hinder silver separation when the electrode is inserted, 10) Deposition of copper at the back side of the SU-8, and 11) Connecting wire with the copper thin plate. The device test results demonstrated similar characteristics of the signals obtained by conventional wet electrodes and the dry fabricated micro-needle electrodes both in the time domain and much better recognizable in the frequency domain [7].

Some other research [22, 16] has been done to fabricate MEMS EEG electrodes to detect and monitor drowsiness, and their pivotal advantages remained their smaller size, lack of conductive gel, penetration to SC/SG, lower impedance and decreased preparation time. The fabrication process was mainly comprised of the following stages based on isotropic and anisotropic etch processes of silicon: 1) Deposition of photo-resist on silicon to build a hard thick mask, 2) Isotropic HNA etch of silicon, 3) Anisotropic RIE of silicon, 4) DC-sputtering titanium/platinum, 5) Cutting the electrode set (short release etch), and 6) Mounting electrodes on FPCB using silver glue. Five dry electrodes and five wet electrodes were placed in five regions close to each other to test the fabricated dry electrode. The signals were obtained, recorded and compared; the comparison showed similar characteristics [22, 16].

Other research [60, 45] focused on alternative design and fabrication of micro-ECoG electrode array for a spatiotemporal recording of epileptic electrophysiological activity from brain regions. The main benefits of the design proposed in [60] include the capability of μECoG recording by using flexible (PDMS-Parylene-PEDOT:PSS-MWCNT) electrodes, electrode conformability, fine spatiotemporal resolution, high sensitivity, low impedance, flexibility, small size, bio-compatibility, good mechanical and chemical stability, low impedance, consistency and high signal-to-noise ratio (SNR) as well as epilepsy monitoring. The electrode was constructed of a PDMS layer, Parylene thin layer, gold layer, Parylene thin layer and MWCNT/PEDOT-PSS. Their fabrication process goes as follows: 1) Sputtering aluminum over the glass wafer as a sacrificial layer, 2) Spin-coating PDMS over the aluminum layer, 3) Deposition of Parylene over the PDMS layer, 4) Sputtering chromium/gold over the Parylene, 5) Photo-resist deposition and patterning it for the etch (corrosion) process of gold and chromium, 6) Photo-resist removal, 7) Treatment of the underlying Parylene by O_2 plasma, 8) Deposition of Parylene over the chromium/gold and the previous Parylene layer, 9) Photo-resist deposition and patterning it to subject

the deposited Parylene layer, 10) RIE patterning of Parylene, 11) Photo-resist removal by acetone, 12) Adding MWCNT/PEDOT:PSS polymer solution, and 13) Electrochemical deposition of the polymer over the exposed gold within the Parylene layer. The performance of the bare gold electrode was compared against the MWCNT-PEDOT:PSS coated electrode. It demonstrated a higher impedance in the frequency spectrum [60].

HE et al. [45] designed and fabricated MEMS polymer-based electrode array for micro electro-corticography monitoring epileptic activities in the brain. It could record in-vitro epileptic discharge in rat hippocampal slices with more hydrophilicity, great performance, low impedance, small phase delay, high SNR, and good bio-compatibility. The fabrication process was carried out within the framework of the following stages: 1) Spin-coating photo-resist over the glass, 2) Photolithography, patterning and development, 3) Sputtering chromium/gold, 4) Patterning by lift-off process, 5) Deposition of three layers of SiO_2, Si_3N_4 , and SiO_2 (layer for hydrophilicity) by Low Pressure Chemical Vapour Deposition (LPCVD), 6) RIE of the dielectric layer at all places except for the metal electrode by CHF_3, 7) Deposition of photo-resist and patterning it to expose chromium/gold in electrode places, 8) Sputtering gold and lift-off to generate the pattern, and 9) Electrochemical deposition of MWCN/PEDOT:PSS over the gold. The process of preparation of MWCNT/PEDOT:PSS solution included carboxylation, ultrasonic dispersion, adding PSS and EDOT polymers. MWCNT/PEDOT:PSS results in lower impedance, higher SNR, and bio-compatibility. The performance of bare gold against the MWCNT-PEDOT:PSS-coated electrode was compared, and a higher impedance in the frequency spectrum and higher phase delay (absolute value) were demonstrated [45].

Ledochowitsch et al. [57] designed and fabricated Parylene-based dense MEMS electrode array for micro electrocorticography. It was capable of micro ECoG using

an array of electrodes with high spatiotemporal resolution, high SNR, greater area coverage, lower impedance, non-invasiveness, novel communication prosthetics and as a means for addressing the outstanding issue of spatial sampling, and electrode size. The significant advantages are similar to the previous one: excellent spatiotemporal resolution, bigger area coverage, non-invasiveness, and addressability. The fabrication process goes as following stages: 1) Cleaning a Borofloat glass carrier wafer by sonication in water, IPA and acetone, 2) Deposition of Parylene, 3) Plasma-treating the Parylene surface to achieve better metal adhesion, 4) Spin-coating photo-resist and patterning it, 5) Deposition of platinum and patterning it via an acetone lift-off process, 6) Vapor-deposition of a monolayer of γ-MPS (as a standard Parylene adhesion promoter), 7) Deposition of the second layer of Parylene over the metal, 8) Deposition of the second Parylene layer, 9) Photo-resist deposition and patterning, 10) Patterning vias in the Parylene by O_2 plasma RIE, 11) Sputtering platinum and pattering it by lift-off, 12) Vapor-deposition of a monolayer of γ-MPS, 13) Deposition of the third and final layer of Parylene over the platinum and the previous Parylene layer, 14) Photo-resist deposition and patterning, 15) RIE patterning of vias and metal surface for establishing a contact between tissue and electrodes, and 16) Photo-resist removal by acetone. Electrochemical impedance spectroscopy was done to obtain the real and imaginary parts of the impedance with respect to frequency to test the fabricated electrode. The electrode was placed over the hippocampal auditory cortex by subjecting the rat to acoustic stimulation. After the onset of the stimulation, the response is quite sensible. The control test is also done by putting the electrode far from the auditory cortex region, resulting in no reaction after acoustic stimulation [57].

Zia et al. [112, 111] designed and fabricated a flexible 3D multi-electrode array for EMG recording out of expiratory songbird muscles. The design's main benefit was EMG recordings with a high SNR. The fabrication process was done in the

following way: 1) Spin-coating a polyamide layer on a silicon carrier wafer, 2) Curing the polyamide to build a thick film of polyamide layer, 3) Spin-coating photo-resist over the polyamide layer, and patterning it, 4) Sputtering titanium/gold over the patterned photo-resist and the polyamide layers, 5) Metallization via lift-off, 6) Photoresist removal by acetone, 7) Dome-shaping of the photo-resist over the gold layer on electrode sites by a reflow process, 8) Deposition of another thin layer of photo-resist and patterning, 9) Sputtering titanium/copper over the photo-resist, 10) Lift-off of titanium/copper at the dome sites to build a photo-resist mold, 11) Electroplating nickel to cover the dome shapes, 12) Phot-resist removal by acetone, 13) Coverage of nickel parts with gold via electro-less plating (electro-less immersion process), 14) Deposition of PDMS and making photo-resist patterned, 15) Etching PDMS at the dome sites to expose dome-shaped electrodes, and 16) Peeling polyamide off the silicon wafer. The fabricated electrode was tested to record EMG activities of air sac muscles in a songbird and demonstrated a good function for peak detection [112, 111].

Table 2.1 summarizes the review of papers on the following bio-electrodes for recording of different bio-potential signals: ECG, EEG, ECoG, and EMG electrodes. It compares different electrode designs and fabrications. By and large, we can state the following conclusion about this review:

- The MEMS fabrication procedures are capable of improving electrical, mechanical and chemical characteristics and bio-compatibility properties as well.
- The MEMS fabrication procedures can be used for both micro and macro bioelectrodes.
- They might eliminate the application of conductive gel as a kind of electrical impedance reducer.
- Chiefly, they decrease electrical impedance by taking advantage of piercing

capability and improved contact-surface of micrometer-sized features brought about by MEMS fabrication.

- Micro-needle geometry design can remarkably decrease impedance and eliminate conductive gel usage.
- They might improve spatiotemporal resolution and reduce financial costs and patient time preparation. They provide device portability and make point-of-care and self-usage accessible to consumers.
- The most applied procedures are photolithography, wet etch, RIE, LPCVD, sputtering, PDMS casting, and plasma surface treatment.
- The MEMS bio-electrodes can be integrated with instrumentation amplifiers on a single electronic board.
- The MEMS bio-electrodes possibly show more robustness against corrosion in long-time durations.
- The MEMS fabrication procedures have been mainly exploited for the following bio-electrodes deeming the signal range (milli and micro volts): EMG, ECG, and EEG.
- Most of the materials exploited in the fabrication of MEMS bio-electrodes are doped silicon, titanium, chromium, gold, copper, and silver as conductive material, Polyamide, PDMS, SU-8, and Parylene as insulation and structural material, and some polymers as the end-interfacing bio-compatible material.
- Bio-electrodes with structural materials of Polyamide, PDMS, Parylene and other types of flexible/stretchable polymers could be exploited to enhance conformability.
- Modified polymers and recent technologies such as MWCNT and PEDOTPSS could be exploited to improve electrical conductivity and bio-compatibility, which might be deposited via electrodeposition, sputtering or 3D printing.
- Flexible/stretchable printed circuit board technology can be considered a

supplementary asset to mount Bio-MEMS recording electrodes and their instrumentation electronic circuits as a whole, reassuring one of the integration concepts.

2.2 Fabrication technologies and tools

Among fabrication technologies for building bio-electrodes, the main ones with which we are primarily concerned here in our research, methodologies, and our discussed/adopted (implemented) fabrication process in the next chapters (3 and 4), are sputtering, Fused Deposition Molding (FDM)/Fused Filament Fabrication (FFF) 3D-printing, and Stereo-lithography (SLA) 3D-printing. We will also exploit medical balloons as an inflatable actuation substrate (tool) for mechanical actuation of our designed and fabricated electrodes (in different sections of Chapter 4, mainly Section 4.8).

2.2.1 Sputtering

Sputtering is one of the Physical Vapour Deposition (PVD) methods, which is a transfer of a solid material (target) onto a substrate with the aid of crash-bombarding energy of inert gas molecules (ions). There are four different types of sputtering: DC, RF, Magnetron, and Reactive sputtering, among which DC and RF methods are used more.

In DC sputtering, depositing material and the underlying material are fastened over the cathode and anode electrodes inside the chamber. They are called the target and substrate of the chamber, subjected to a vacuum with a pressure range of (1,100) mTorr. Ar gas is injected into the chamber, and the power supply is switched ON to apply a DC negative voltage to the cathode to establish a plasma environment and ionize Ar to Ar^+. Ionized atoms are attracted towards the cathode. Ar^+ bombard the

Table 2.1: ECG/EEG/ECoG/EMG MEMS electrode fabrication: current state-of-the-art.

Reference	Bio-signal	Main advantages	Major fabrication technologies
[17]	ECG	Dry electrode without requiring conductive gel, penetrating SC and reaching SG layer in epidermis, low-noise, and low-power	Si wet isotropic etch, RIE, DC sputtering, FPCB, Silver gluing
[95, 97]	ECG	Dry foam electrode for wearable ECG, noninvasive, no conduction gel used, good signal quality, disposable and low-cost, good mechanical stability upon attachment on the skin, good conductivity	Using conductive foam, Metallization via sputtering
[46]	ECG	Dry barbed electrode, Sturdier attachment, no conductive gel need, low-cost, simplicity	LPCVD, Si anisotropic/isotropic wet etch, Photolithography, Sputtering
[98]	ECG	Gel-free dry recordings, extremely thin bendable electrodes, ease for the patient, no skin preparation, fitted to the human torso	Photolithography, Sputtering, Electroplating
[52]	ECG	Recordings with two electrodes instead of commercial three-electrode configuration	Lithography, Cu lamination, Cu wet etch, FPCB, Photolithography, Sputtering, Polyamide spin-coating
[68]	ECG	Dry electrode without using gel, contact-less bio-potential pick-up at a distance of 0.5 mm	RF sputtering, Photolithography, Electroplating, Cu wet etch, Polymer spin-coating, Polyamide substrate usage
[105]	EEG	Gel-free recordings, comfort for the examinee, reducing skin time preparation	Photolithography, PDMS molding, Sputtering, Electroplating, Glass substrate usage
[7]	EEG	Gel-free dry recordings, Penetrating the SC, No skin treatment, High-quality measurements, Comfort for examinee, Low impedance for hours	Photolithography, PDMS casting, CVD, Parylene usage as over-layer, 3D-printing
[22, 16]	EEG	Dry electrode without requiring conductive paste or scalp preparation, Piercing the skin SC, Superior electrical conduction in electrode-skin interface impedance, signal intensity, less size over the conventional (wet) electrodes	Photolithography, Si isotropic wet etch, RIE, Sputtering
[60]	ECoG	Recording using flexible (PDMS-Parylene-PEDOT:PSS-MWCNT) electrodes, conformability, fine spatiotemporal resolution, high sensitivity, low impedance, and high SNR, epilepsy monitoring	Sputtering, PDMS spin-coating, Photolithography, RIE, Electrochemical deposition
[45]	ECoG	Capable of in-vitro epileptic discharge recording in rat hippocampal slices with more-hydrophilicity, great performance, low impedance, small phase delay, high SNR and good bio-compatibility	Photolithography, Sputtering, Lift-off, LPCVD, RIE, Electrochemical deposition
[57]	ECoG	Array of electrodes with high spatiotemporal resolution, high SNR, greater areal coverage, lower impedance, non-invasiveness, novel communication prosthetics as a means of addressing the issue of spatial sampling and electrode size	Photolithography, E-beam evaporation, Lift-off, CVD, RIE
[112, 111]	EMG	Capable of high SNR EMG recordings from the expiratory muscle of a songbird	Photolithography, Sputtering, Lift-off, Electroplating, Electrochemical deposition

target, separates atoms from the target material and convert to Ar, having accepted electron from the cathode. The separated atoms touch down the underlying material over the substrate. Gas is sucked out of the chamber at the end. DC method is a cost-effective method for various types of metal thin deposition. It has limitation in deposition of dielectric nonconductive targets because they are electrically charge-accumulated gradually, leading to problems of arcing and target *charge-poisoning* and causing the sputtering process to stop [55].

RF sputtering is employed for depositing dielectric materials in which the target connects to an impedance-matching network connected with an RF power supply. The AC power prevents Ar^+ from gathering up over the target material and prevents the process from stopping when sputtering a dielectric target material. The reason goes as follows. After establishing the plasma, a charge builds up around the target and substrate electrodes. The charge density over the target becomes greater than the charge density over the substrate because the substrate area is larger than the target area. Consequently, the target voltage increases more than the substrate voltage, bringing more sputtering around the target than the underlying material over the substrate. This voltage ultimately leads to a net charge from the target to the substrate, establishing a net film deposition from the target to the substrate.

Sputtering's primary advantages are as follows: 1) Many types of material can be sputtered (metals, metal oxide/nitride such as TiN [24], alloys [70, 74, 55], ceramics [14, 69, 38, 103], dielectrics such as Si_3N_4 [84, 37] and SiO_2 [10], polymers [11, 56]), 2) Great step coverage, 3) Control of the deposited layer characteristics and 4) Sputtering chemical compositions. The reasons for improved side-wall coverage in sputtering compared with other methods such as thermal evaporation go as follows: similar target size and substrate size, decreased mean free path, and great surface mobility. Furthermore, step coverage is enhanced by non-vertical crash/incidence and high energy of sputtered atoms compared to evaporated atoms. The parameters

for controlling the characteristics of the deposited layer include RF/DC power, substrate temperature, substrate bias, gas mixture, gas pressure, and gas dynamics. For example, they may be used to handle stress [66, 15, 33].

2.2.2 3D-printing

3D printing, as an *in-situ* additive, time-effective and cost-effective layer-by-layer fabrication method, uses a CAD model to build an entity. The 3D-printing history returns to 1984 [47], using resin to deposit the material layer-by-layer and do a UV-curing. Then, Selective Laser Sintering (SLS) was introduced in 1989 by [31] for metal deposition. Fused Deposition Modeling (FDM) and Material Jetting (MJ) were introduced in 1992 [25] and 1999, respectively. Most 3D-printing technologies are recently advancing to build micro/milli-sized elements of metals, polymers, and ceramics for modern applications [30, 92, 12, 76, 35, 67, 44, 29].

Material extrusion apparatus comprises five sections: heater/piezo element (liquefier), nozzle, z-displaceable plate, and build/support material spools. The feeding material is a thermoplastic wire. It becomes semi-melted and is deposited over the building plate. The melted feeding material contacts the low-temperature surface of the building plate. A material extrusion apparatus with a triple-nozzle was exploited in [65] to fabricate a MEMS capacitive force sensor using poly-lactic acid. FFF or FDM machines are material extrusion apparatuses that warm up a thermoplastic polymer to its glass transition temperature, leading to the deposition and solidification of the material on the fabrication plate. Thickness, step resolutions and stress properties can be controlled by nozzle size, temperature or speed. PDMS additive manufacturing was used by Li et. al [61] for making micro-fluidic chips intended for micro-mixing and droplet generation. FDM was applied by Tothill et al. [94] to build a micro-fluidic device for analyzing glucose.

Stereo-lithography (SLA) apparatus is based upon layer-by-layer UV-curing

of a photo-polymerizable thermoset polymer (resin). Certain wavelengths develop crosslinks and cause the solidification of the resin. SLA has been employed for building MEMS devices, including micro bone tissue scaffolds [23], cell-culturing micro-fluidic chips [53], micro-bio-structures [100, 101], and micro-needle electrode arrays [85]. SLA is grouped into two main categories: free and constrained surface SLAs. The SLA light sources are categorized into Laser-based and Digital Light Processing (DLP) SLAs. The laser-based SLA uses a lonesome UV laser, whereas DLP exploits a UV projection matrix. DLP SLA has been used by researchers [96, 41, 29, 108] to fabricate micro-ceramic and polymer devices for microfluidic applications such as micro-pumps, micro-valves, and fuel cells.

Powder Bed Fusion (PBF) apparatus is made up of a z-displaceable plate, powder boxes, re-coating roller, powder nozzle, optics guide, and laser/e-beam gun. This additive manufacturing machine melts metal powder as the building material layer by-layer and uses the powder as the support material [21]. Laser-based PBF was applied by Qu et al. [78] to form intricate Cu micro-structures with a wall thickness of 100 μm. This might be used to fabricate MEMS devices indirectly. For making a MEMS force sensor, stainless steel was metal-printed by Kamat et al. [50] to build a metal micro-mold for casting PDMS. Laser beams are exploited in Direct Metal Laser Melting (DMLM) and Selective Laser Sintering (SLS) to melt metal powder and granular thermoplastic polymers, respectively. It leads to layer-by-layer production of structures with remarkably great resolutions. SLS was developed by Roy et al. [80] to make structures with resolutions greater than 5 μm. Surface roughness of about 1.3 μm was obtained by Nagarajan et al. [71]. We can see that FDM, SLA, and PBF show great potentials for building Bio-MEMS devices.

2.2.3 Medical balloons

High-pressure balloons were developed in 1970 and are used for angioplasty to cross out fatty masses in blood vessels. Nowadays, high-pressure medical balloons with considerable strength and minimal dimensions are applied in minimally invasive medical diagnostic and therapeutic procedures. Their shape, diameter, length, and strength can be customized, and there is a reasonably limited freedom in choosing their constructive material [1]. Figure 2.2 depicts various known shapes for medical balloons. Figure 2.2m typically displays different parts of a canonical-spherical medical balloon. The applications include dilation, positioning, occlusion, heat transfer, light transfer, and drug delivery [40]. The balloon dilation type might be non-compliant, semi-compliant and compliant. Each differs from the other two in pressure, material, compliance range, achievable size and bursting pressure. The bursting pressure may span from 1 to 30 atm depending on the type. The material could be Polyethylene terephthalate (PET), Urethane, and Nylon with low/medium/high durometer and some feasible coatings.

Two fundamental varieties of balloons are exploited in medical applications: 1) force-application balloons, 2) fixation and occlusion (removal) balloons. The former are high-pressure nonelastic balloons used for angioplasty and dilatation. The latter are low-pressure elastomeric balloons. The first type of constructive material is PET, Nylon, and PVC. The second type of material is latex or silicone. The first category is non-compliant or semi-compliant, while the second group is compliant types [1].

High-pressure balloons are usually made in three stages: 1) extruding a tube, 2) cross-linking the extrusion, 3) reheating and stretch–blow molding of the extrusion into the desired geometry. An ordinary dilatation balloon is comprised of a cylinder, two conical tapers, a proximal neck and a distal neck [1].

When the balloon inflates, it will be subjected to stress, which needs to be controlled not to damage the organ. There are two types of stress in a medical

balloon: hoop (radial) stress and axial (longitudinal) stress [82], which are expressed by the following equations, respectively:

$$\sigma_r = pd/2t\,, \tag{2.2.1}$$

$$\sigma_l = pd/4t\,, \tag{2.2.2}$$

where p, t, and d are balloon pressure, thickness and diameter [1, 2, 5]. Radial tensile strength, designated by T_{rs}, is obtained as follows:

$$T_{rs} = P_b d/2t\,, \tag{2.2.3}$$

P_b, d, and t are burst pressure, reached (as made) diameter, and reached thickness because tensile strength is the maximum stress a material can tolerate when stretched or pulled before breakage [1]. Recently, research has been developed to model balloon inflation dynamics. For instance, Li et al. [59] simulated the folding process of two different balloon materials using numerical methods to evaluate and study retraction, insertion and friction forces. As another example, Dai et al. [26] exploited artificial neural networks (ANN) and nonlinear regression for balloon uniformity prediction. The hoop stress is twice of the axial stress so a balloon will usually break into parts longitudinally rather than circumferentially in case of failure (probably in PET non-compliant balloons). Although it might be acceptable in many medical applications, we will see later that it may emerge problematic in our application due to the closeness of the catheter tip to the TM. This imposes limitation on choosing an appropriate catheter in our design. In our research in this thesis, we will mainly use Foley balloon catheters (silicone/latex types) and PET PTCA dilation balloon catheters for a couple of reasons. More exactly, Foley balloon catheters will be our final choice.

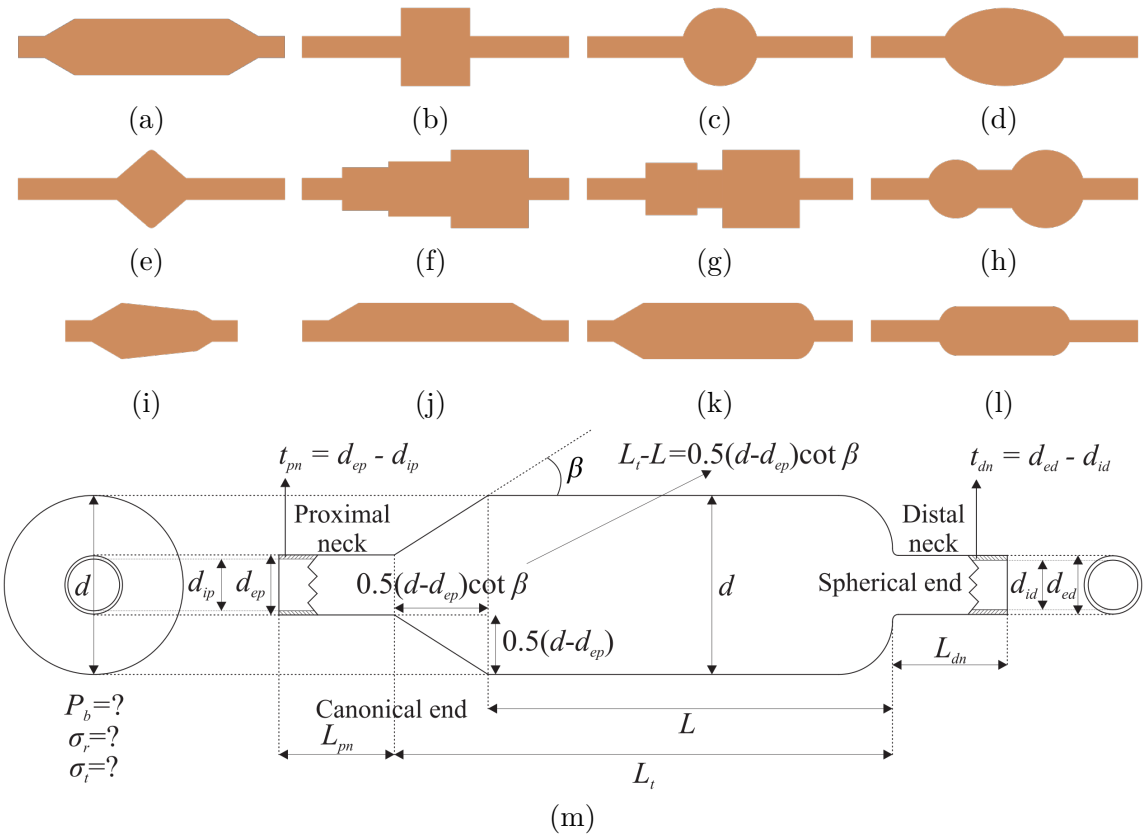

Figure 2.2: Different shapes of balloons: (a) Standard (b) Square (c) Spherical (d) Elliptical (e) Canonical (f) Stepped (g) Dog bone (h) Peanut (i) Tapered (j) Offset (k) Canonical spherical (l) Spherical-square. (m) Geometrical parameters of a typical balloon.

2.3 EVestG signal

The history of EVestG signal recording and research on neuro-degenerative disease mostly backs to at least 2006 and 2008 at Monash University in Australia [62, 42]. Its operation pathway is based on the electrical signaling from the inner ear balance organs to the brain and back during body/head movement. The ear hearing and balance functions are illustrated via two block diagrams in Fig. 2.3. EVestG records the electrical activity of the vestibular labyrinth, which entails the otolith organs and the semicircular canals, during stimuli and at rest. The stimulation is generated by subjecting the patient to controlled, slow, and safe movements in a hydraulic chair capable of moving up/down, rotation and tilting to sides, as well as the above

motions in the supine position. While stimulated, the vestibular system dispatches kinematic information as electrical signals to the brain. However, it does not only go to the brain since afferent and efferent pathways exist.

Two types of kinematic information are generated by this part of the inner ear organ: linear and rotational acceleration data. Utricle and saccule, which are significant parts of the vestibular system, operate as linear accelerometers for movement detection in the horizontal and vertical planes, respectively. They are sensitive to the head linear displacements in the transverse and sagittal planes. Their structures benefit a crystal-like otolithic organ working in series with hair cells to detect motion and generate an Action Potential (AP) in correspondence with the movement, similar to the hearing system. Unlike the otolith organs, the semicircular canals, as another set in the vestibular system, are sensitive to 3D-space rotation. These gyroscopes detect rotation around the normals of the sagittal, coronal and transverse planes. Angular momentum moves the endolymph within the canals. It bends the cupula inside the canals ampullae in different directions with various strengths and generates AP via the hair cells.

Hair cells within the utricle, saccule and semicircular canals transduce motion into electrical signals. Movement of stereocilia towards (far from) the kinocilium depolarizes (hyperpolarizes) the hair cells. It causes neurotransmitter release (absence) in hair cell-vestibular afferent synapses, resulting in excitation (inhibition). Due to leakage of the open ion transduction channels in rest and the consequent spontaneous firing in vestibular nerve fibres, depolarization and hyperpolarization generate higher and lower firing rates, respectively. The generated firing signals represent linear or angular acceleration. A mapping is established among the rotation rate or linear momentum, AP firing rate and the electrical neural signal received by the brain. Figure 2.3 summarizes the physiology of the hearing and balance systems in two block diagrams.

The EVestG signal is fed-back to the inner ear organ on the ear canal wall near the Ear Drum (ED). The EVestG field potential contains some nerve and brain functional information, which is exploitable for diagnosing the aforementioned neural disorders. The delicacy and sensitivity of an electromechanical system in the inner ear require researchers' high care and scrupulousness in proposing solutions for local signal recording. The EVestG signal pathway mainly comprises ED, the balance system, 8th Cranial Nerve and emotional, behavioral and brain motor centers.

2.4 Currently-used EVestG electrode

Figures 2.4a and 2.4b display the currently used electrode and its components for EVestG recording. Each electrode is a silver wire put inside a silicone tube. One tip is ring-shaped and covered with cotton-wool so as not to damage the TM. The other tip is connected with a metal gold connector with a heat-shrink tube. The connector goes to the EVestG amplifier. An ear plug is used to fix the silicone tube in the ear canal. Not only is the silver wire a conductor between the ring tip of the electrode and the amplifier connector, but it also plays the role of a guide wire, which helps the physician/technician embed the electrode inside the ear canal. The silver wire diameter is about 0.25 mm, and its length measures about 21 cm. The ring tip diameter is about 2 to 3 mm accommodating the cotton wool around it. Two of these electrodes are used for an EVestG recording. One electrode is almost placed at the end of the ear canal near the TM. It is called active electrode. The other is located at the inlet of the canal and is called passive electrode. The distance between the electrodes is about 2.5 cm. The ear canal length is typically about 2 to 3 cm. Figure 2.4c illustrates the embedment of the electrodes inside the canal and around the auricles using the ear plug and some sticking plasters, respectively.

Problems of signal recording via the current EVestG electrode may remain as

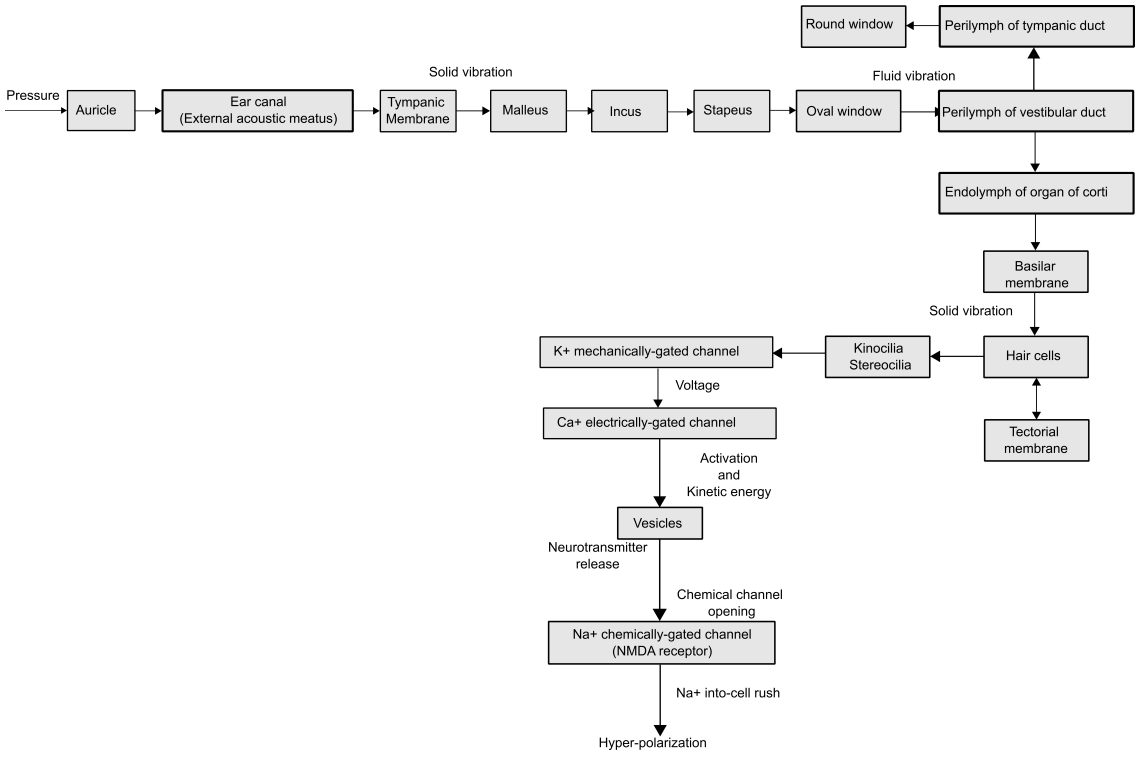

(a)

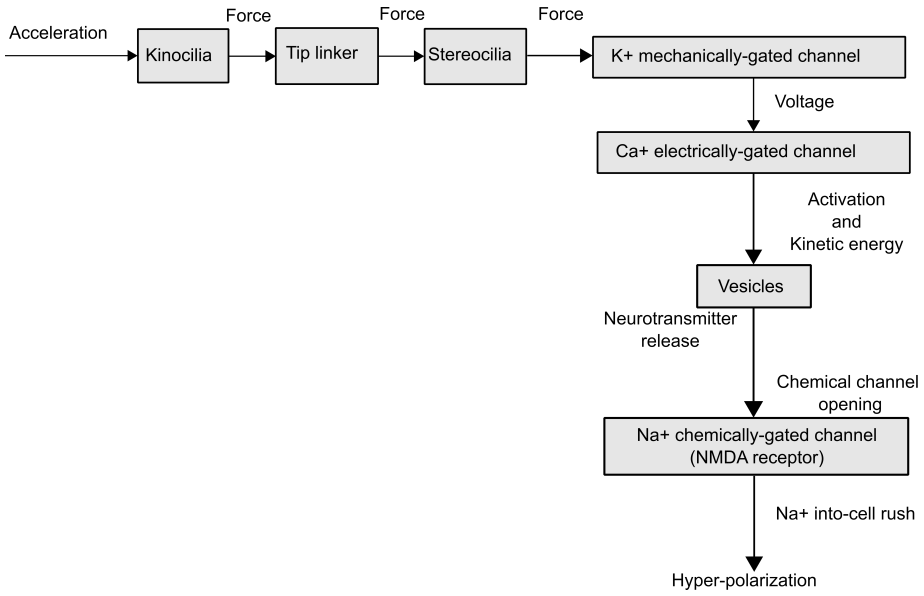

(b)

Figure 2.3: Hearing and balance system physiology: (a) Sound energy is transmitted to the perilymph, tectorial membrane, cilia, and mechanical-gated channels of hair cells, generating an AP. (b) Angular momentum moves the endolymph, bending the cupula inside the Ampullae in different directions with various strengths, producing an AP by the hair cells in the cupula.

the following undesired effects: Electrode movement due to the chair tilt and jerks, Difficulty in the electrode fixation at the appropriate contact region. Coverage of the electrode tip with lots of conductive gel, Short circuits in differential mode by the gel along the ear canal between the active and passive electrodes, Facial muscle movement artifacts, Noise boosting due to the long wire antenna effect, Disruption subjected to the ear wax, and Noise impact by breaks in the wire or loops. Furthermore, preparing the electrode for the EVestG experiment is time-consuming for the technician. Not only is the inner ear hardly accessible for signal acquisition, but also the signal ranges from nV to a few μV; it is buried in noise so that the SNR is about -30 dB. The type of stimulation hinders one from applying numerous repeated clinical recordings and averaging to demolish noise. Other biological signal processing methods, such as wavelet de-noising, are intrinsically limited in improving SNR. Hence, software solutions remain insufficient for the signal de-noising.

Figure 2.5a schematically illustrates some of the bottlenecks which prevent physicians from reaching a non-noise-polluted bio-signal for diagnosis purposes. The first is how to get the signal recording areas of A and B concerning the arches of the canal while increasing contact surface area, reducing the contact impedance and handling motion artifacts. In particular, A is a far-reaching area near the TM. The second bottleneck is wiring C, which malfunctions as an antenna, embracing environmental stray noise. The third is the instrumentation, signal conditioning and digitization hardware.

There should be appropriate contacts with inner ear canal walls (skin) in point A and B. The wires, represented above as region C in the figure, should be shortened as much as possible and shielded. As a straightforward and initial design solution seen in Fig. 2.5b, MEMS electrode pads or μ-needles might be embedded on a suitable adjustable holder (yellow structural foam). At the same time, they fill the ear canal thoroughly to support the contact and sustain impedance within a fundamental

and new solution framework. All the measurement circuits and signal conditioning electronics (part D) can be integrated via discrete or integrated components on the adjustable holder and inside a headset (part E) in such a way that the effect of wire antenna noise gets reduced in an optimized manner. A third reference simple electrode is placed and fixed over the forehead. All the above schematic descriptions and discussions somehow clarify more where our motivation and objective, explicitly expressed in Chapter 1, originated from.

The EVestG signal amplitude ranges from 10 to 100 nano volts. Its frequency band is almost 5 kHz. Consequently, a sampling rate of 50 kHz with a resolution of 16 bits is possibly an excellent acquisition rule of thumb for recording this signal. If all the electrodes and the amplifiers are accommodated inside a headset, it can be used to communicate with the patient and possibly apply acoustic stimulation in future research. A sample EVestG field potential and its frequency spectrum (FFT) are displayed in Fig. 2.6. More illustrative information and figures describing and displaying EVestG signal (field potential), EVestG electrodes embedment inside the ear canal, and EVestG stimulation system and tilting chair can be found in [42, 88, 89].

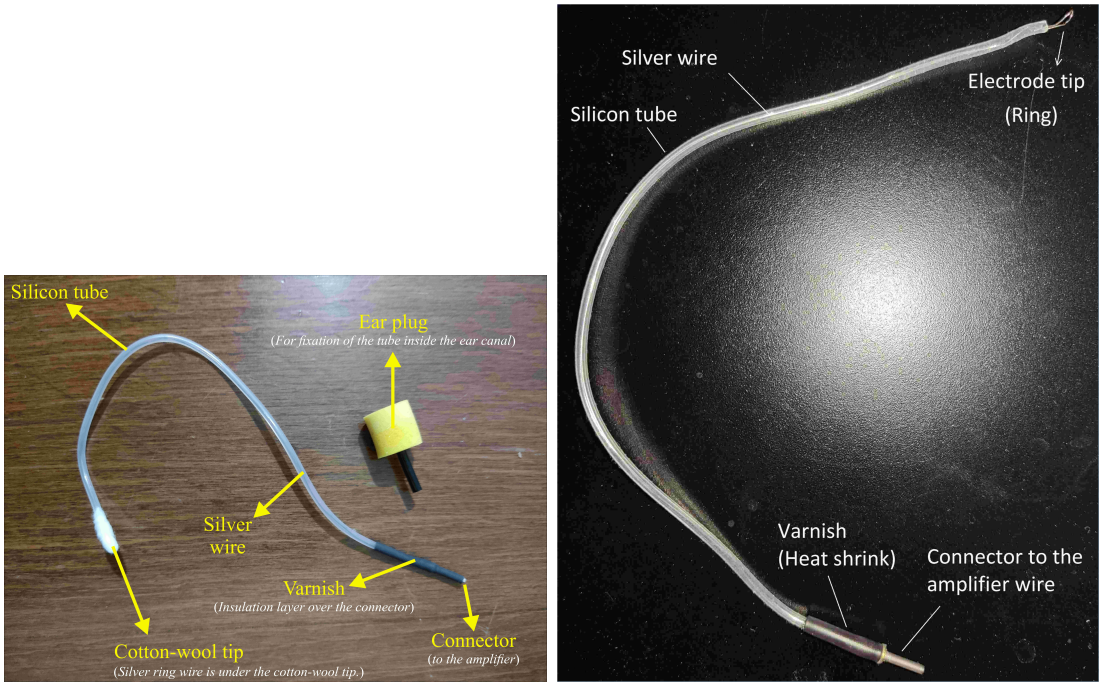

(a) (b)

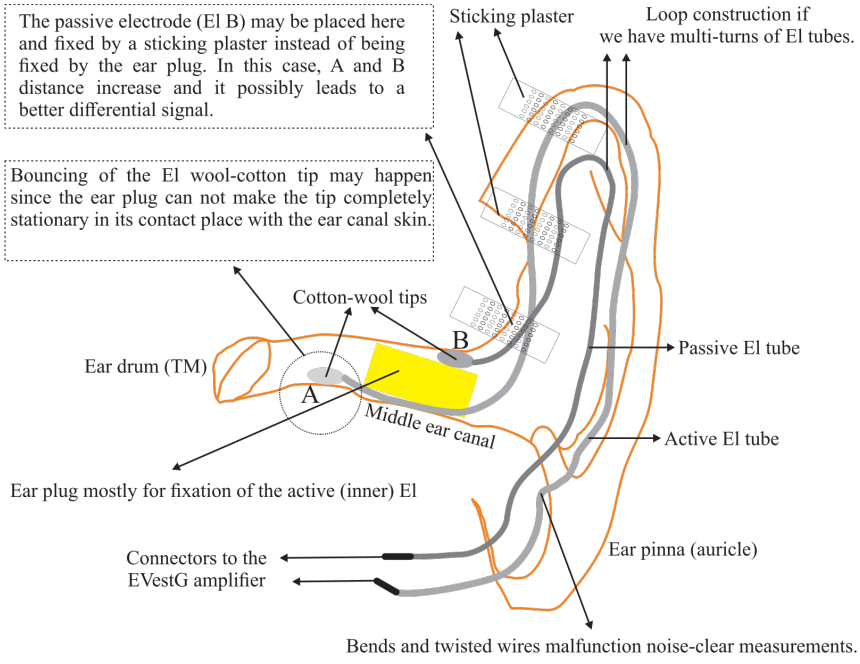

(c)

Figure 2.4: (a) and (b) Current state-of-the-art EVestG electrode and its different components. (c) Embedment of the active and passive electrodes within the middle ear canal.

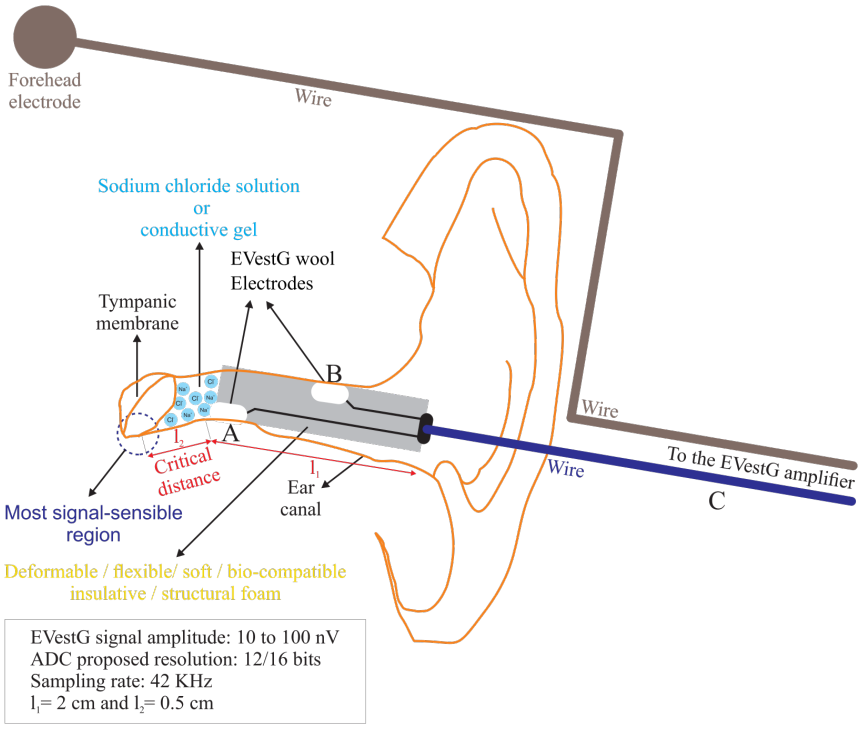

(a)

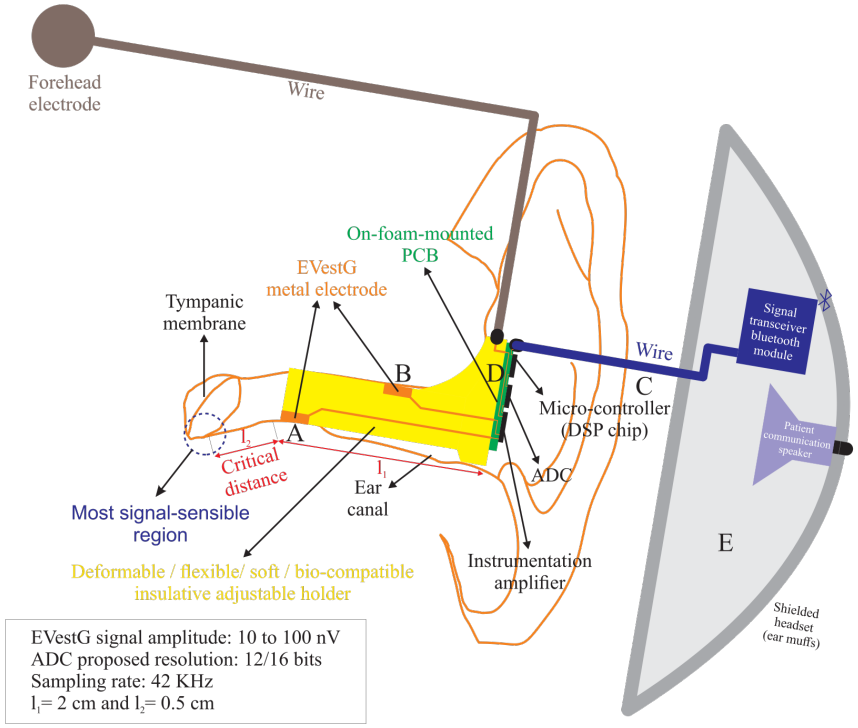

(b)

Figure 2.5: (a) Bottlenecks in EVestG recording using the current electrodes, (b) A conceptual schematic immature solution for EVestG recording to over come the bottlenecks.

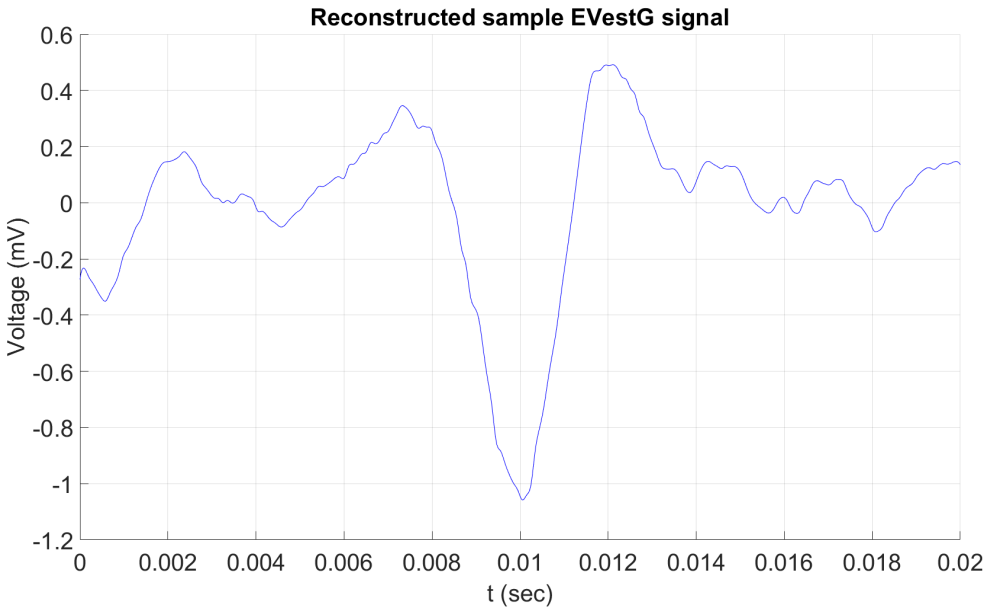

(a)

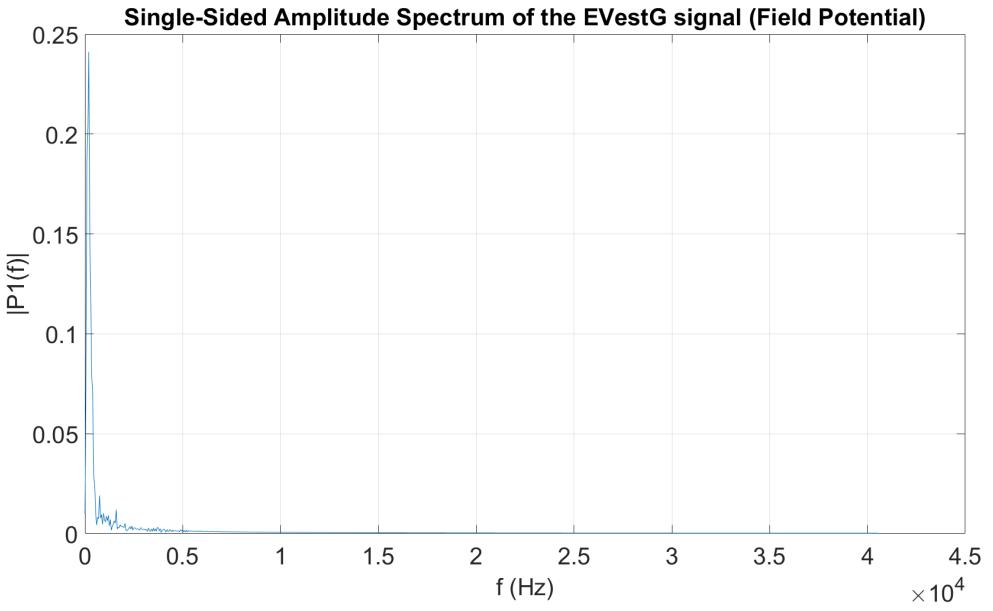

(b)

Figure 2.6: (a) and (b): A sample EVestG field potential and frequency spectrum.

3

Methodology

In this chapter and at the initial stage, a conceptual schematic ideal solution is proposed (not implemented) for tackling the problem of designing a miniaturized electrode with capabilities/characteristics, mainly including in-canal fixation (or in-canal usability) and pressure-controlled reducible impedance, which may show some future potentials for EVestG recording to cope with some of the expressed challenges. Then, a list of simplified methodologies is proposed based on a model reduction approach and investigated from the implementation feasibility aspect. Ultimately, a more approachable methodology seems more implementable regarding our accessible tools, machines, fabrication facilities and resources. This selected methodology will be the framework of our implementations later in Chapter 4. Before these, the problem we are addressing in this thesis is clearly expressed in Section 3.1. Figure 3.1 illustrates a flow chart of the methodological contents presented in this chapter.

3.1 Problem statement

The problem and main research question that we are going to address here in this thesis is how an electrode device can be designed to be applied and fixed in a canal while it is equipped with a micro-needle or a flexible micro pad electrode at its

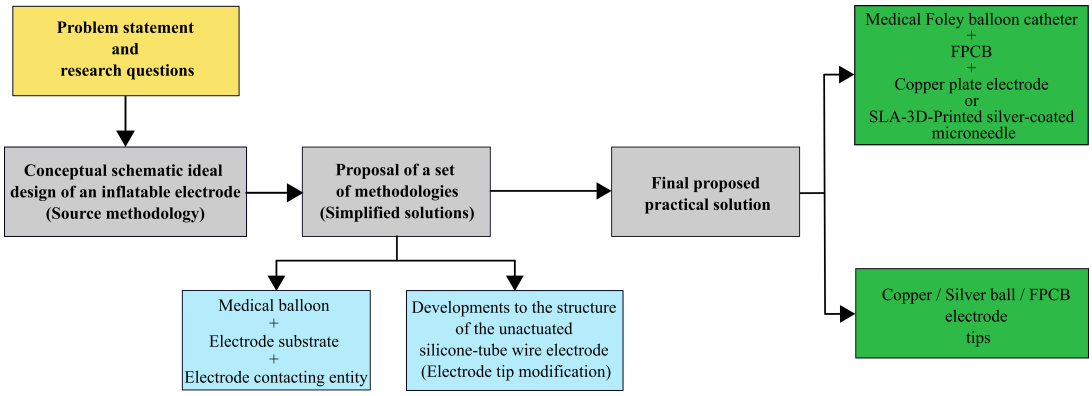

Figure 3.1: Trend of investigation of different methodologies, from a basic ideal immature methodology to more implementable ones, leading to a practical solution, regarding our accessible facilities and resources.

end to contact the skin, minimizing or reducing its interfacing impedance. We are going to deal with this problem in such a way that the proposed solution may show some potential to be used for EVestG recording after further modifications. For more clarification and to have a better understanding of the motivation, one may express the following questions, regarding the currently used EVestG electrode description in Section 2.4:

1. How can a suitable contact be made with a circular canal wall?
2. How can we control the contact modality with the target area while preventing any damage to (interference with) other canal parts?
3. How can the electrode be mechanically actuated to contact the wall appropriately?
4. What is the modality of the interaction of the electrode with the canal in terms of the interfacing impedance against force, pressure, penetration, etc.?

To adopt a suitable methodology for the electrode design described earlier, we may get concerned with some of these questions. These questions, which are not addressed directly and thoroughly in this thesis, are exploited just as some inspiring hints and not of our main concern. There are some assumptions addressing our main research question: we have access to micro-fabrication lab, and non-metal 3D printing

technology for implementation of our solutions. There might be some other questions of interest to be addressed in future research trends; see Chapter 6.

3.2 Ideal conceptual schematic solution of an inflatable electrode unimplemented methodology

An ideal but ambitious solution to address our research's main bottleneck, is illustrated in Fig. 3.2 and Fig.3.3. It is a basic pattern for more simple implementable structures later in this thesis (mainly Section 3.5 and Chapter 4). This complicated conceptual schematic describes the miniaturized MEMS-based electrode as the disposable part (specified in the dotted circle), which is connected with the control, actuation, and measurement facilities outside (displayed in the dotted rectangle).

The disposable electrode has three critical parts: a fixed-diameter core, a variable-dimension inner upper/lower shells, and fixed-dimension outer upper/lower shells. The Fixed-diameter core accommodates a camera lens, LEDs and some connection wires. Variable-dimensional inner upper/lower shells will take advantage of soft robotic actuators, which can be inflated on a gross scale to conform with the canal arch, similar to a cylindrical tube. The Fixed-dimension outer upper/lower shells accommodate two outer metal micro-pads or micro-needle array electrodes with inflatable micro-substrates. Decreasing impedance, the μ-substrates of the μ-needle array electrodes or metal μ-pads are inflated in a fine scale manner to penetrate the canal wall or to make μ-surface contact, respectively. The inflations should be handled via some intelligent controllers, being robust against tube non-modelled dynamics, parameter uncertainty, disturbance and noise, which results in more safety and efficiency. The pressure against the wall might be read via back-pressure of the pumps circuits or embedded strain gauges.

Figure 3.3 illustrates the three stages, from accommodation of the disposable

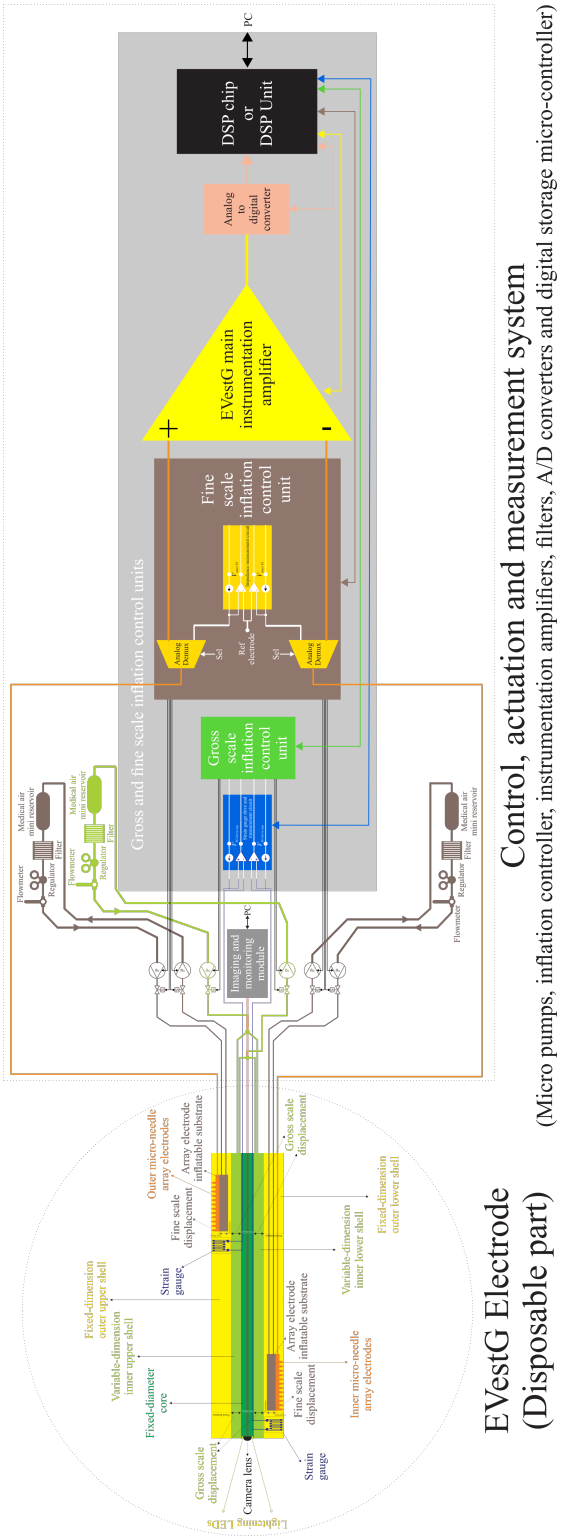

Figure 3.2: Conceptual schematic design of a MEMS-based miniaturized recording system including two major parts: 1) Disposable electrode, 2) Control, actuation and measurement circuitry.

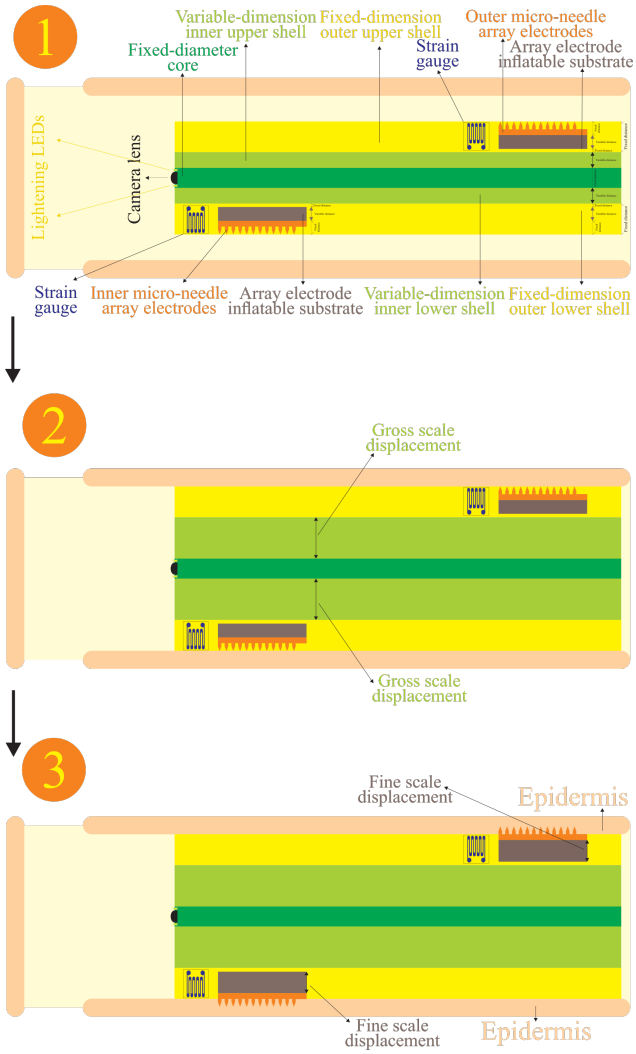

Figure 3.3: Three stages of embedment of the disposable electrode into the canal.

electrode by the canal to insertion of the μ-electrode array into the canal wall or to establishment of contacts of the electrode μ-pads with the canal wall. Stage 1 is a manually monitored embedment of the non-inflated tube-wise device inside the canal. Stage 2 is a controlled circular conformation of the device with the canal wall in a gross scale manner. Stage 3 includes a controlled penetration of μ-needle array into the canal wall or enhancement of the contact area of the electrode μ-pads with the wall, depending on the electrode shape ($\mu needle$ or μpad).

3.3 Simplifying the ideal scheme of the inflatable electrode unimplemented methodologies

Though the scheme in Fig. 3.2 and Fig. 3.3 is complicated, one of the major implementation challenges is the fabrication of the disposable electrode (μ-electrode pads or μ-needle arrays on an inflatable substrate). Our simplifying practical suggestion (model reduction) to overcome the challenge is breaking the design into two parts: electrode mechanical actuation (inflation) system and MEMS or micro electrode. For the actuation, we propose applying customized inflatable medical balloons to conform with the canal. For the electrode, we may propose μ-pad/μ-needles with polyamide flexible substrate mountable on the balloon.

A typical electrode fabrication process is illustrated in Fig. 3.4: 1) Deposition of copper over a polyamide layer, 2) Patterning of photo-resist over the copper layer, 3) Etching the exposed copper layer down to the polyamide layer, 4) Deposition of another polyamide layer over the non-etched copper and the previous polyamide layers, 5) Patterning of photo-resist over the last-deposited polyamide layer and etching to create holes with polyamide walls and copper floors, and 6) Electroplating/evaporation of gold/nickel onto the copper floors inside the holes. We are mostly inspired by [73, 72, 6] to propose such a fabrication process. The product will be mounted over the balloon via a suitable adhesive. However, reaching such a fabrication recipe through experiments is challenging.

Following a practical implementation, our solution might be designing and fabricating the active and passive electrodes (differential electrodes) with geometries displayed in Fig. 3.5 and 3.6 regarding our existing facilities and resources. As depicted in Fig. 3.5 for the active electrode, there is a flexible polyamide substrate in which a copper track, a rectangular pad with an area of about 7.33 mm^2 (copper sub-layer) and another grooved rectangular pad (wire soldering pad) are buried.

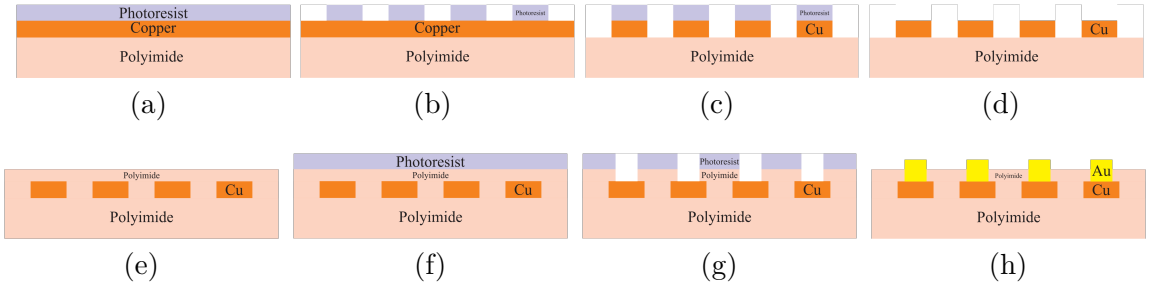

Figure 3.4: Fabrication process of the electrode pads on a flexible polyamide substrate. The polyamide substrate is supposed to be embedded on a PDMS/Silicone/Latex/Polyethylene/Nitrile/rubbery adjustable (yellow) holder or balloon in Fig. 2.5b.

Over the copper sub-layer, a gold/nickel electrode is constructed with a height of $800\,\mu m$, which projects $300\,\mu m$ out of the outermost insulation layer. The copper track connects the wire soldering pad at one end with the copper sub-layer at the other. Figure 3.6 demonstrates a similar structure for the passive electrode, which differs only in planar geometry and not in height.

Fabrication of such an electrode set might be done using either the MEMS conventional process explained in Fig. 3.4 or additive manufacturing e.g., 3D ink-jet printing. In the latter, we may print silver nano-particles as electrode contacts and polyamide as substrate, limiting the metal type to one. The amplifier wire is soldered (connected) to the non-solder-masked (grooved) wire soldering pad.

In the case of building the electrodes with the aid of 3D-printing technologies, one may exploit PBF or DMLM to build the metal (conductive) parts of the electrode geometries presented in Fig. 3.5 and 3.6. In contrast, other 3D-printing technologies, such as Stereo-lithography (SLA) can fabricate the non-metal (non-conductive) parts or insulation geometries of the active and passive electrodes displayed in Fig. 3.5 and 3.6. Then, the 3D-printed conductive and non-conductive parts should be assembled to generate the total structure of the proposed active and passive electrodes. Figure 3.7 schematically illustrates such an assembly concept.

We may use a customized medical balloon as the actuation system of the micro

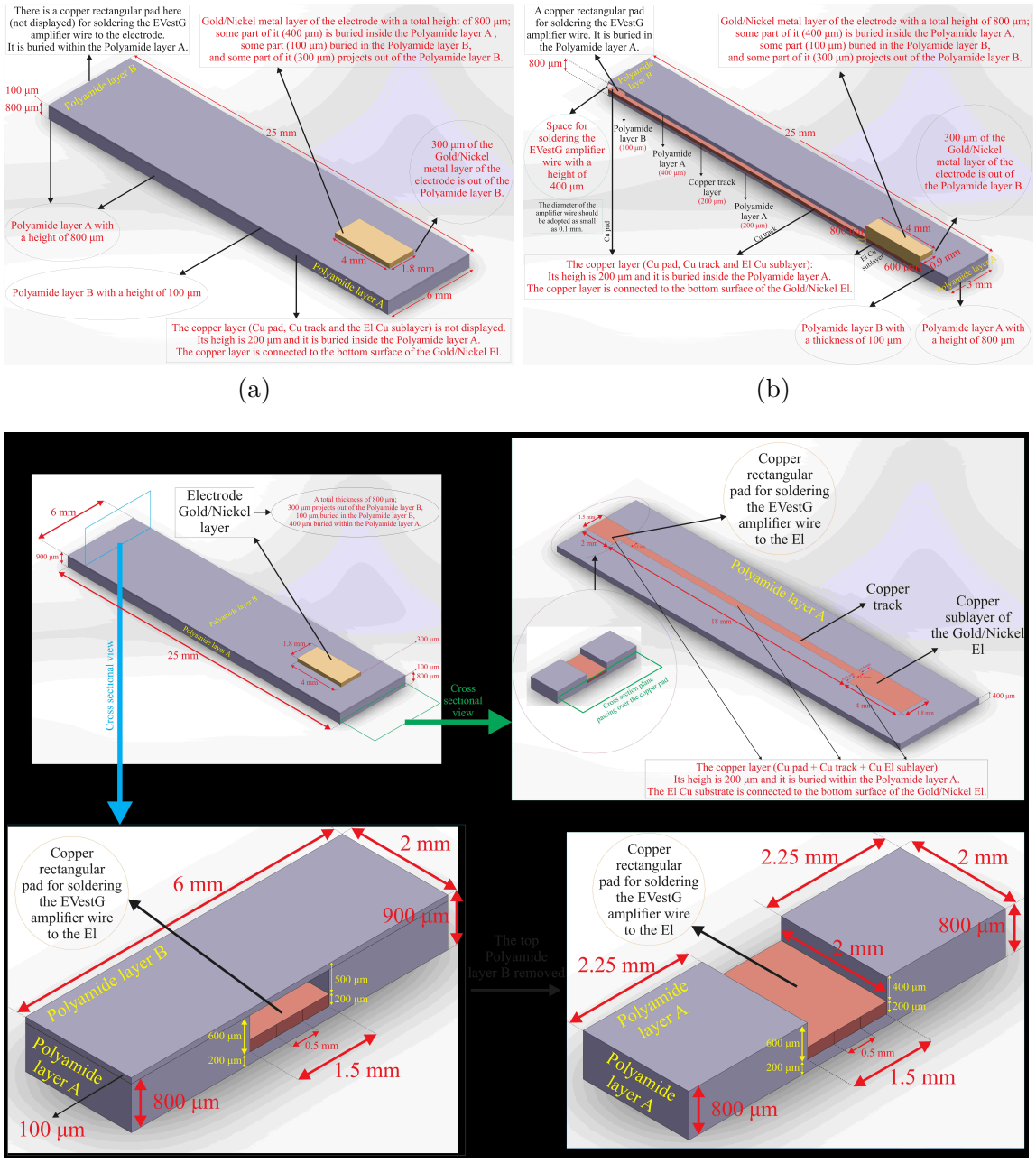

Figure 3.5: Active electrode: the geometrical dimensions and cross-sectional views illustrate three layers of the electrode including Polyamide, Copper, and Gold/Nickel.

electrodes to maintain their contact with the canal wall during signal recording. The active and passive electrode sets are adhered onto the balloon as depicted in Fig. 3.8 to touch point A and B when the balloon inflates. Figure 3.9 depicts another concept of attachment of the active electrode over a medical balloon, which can be

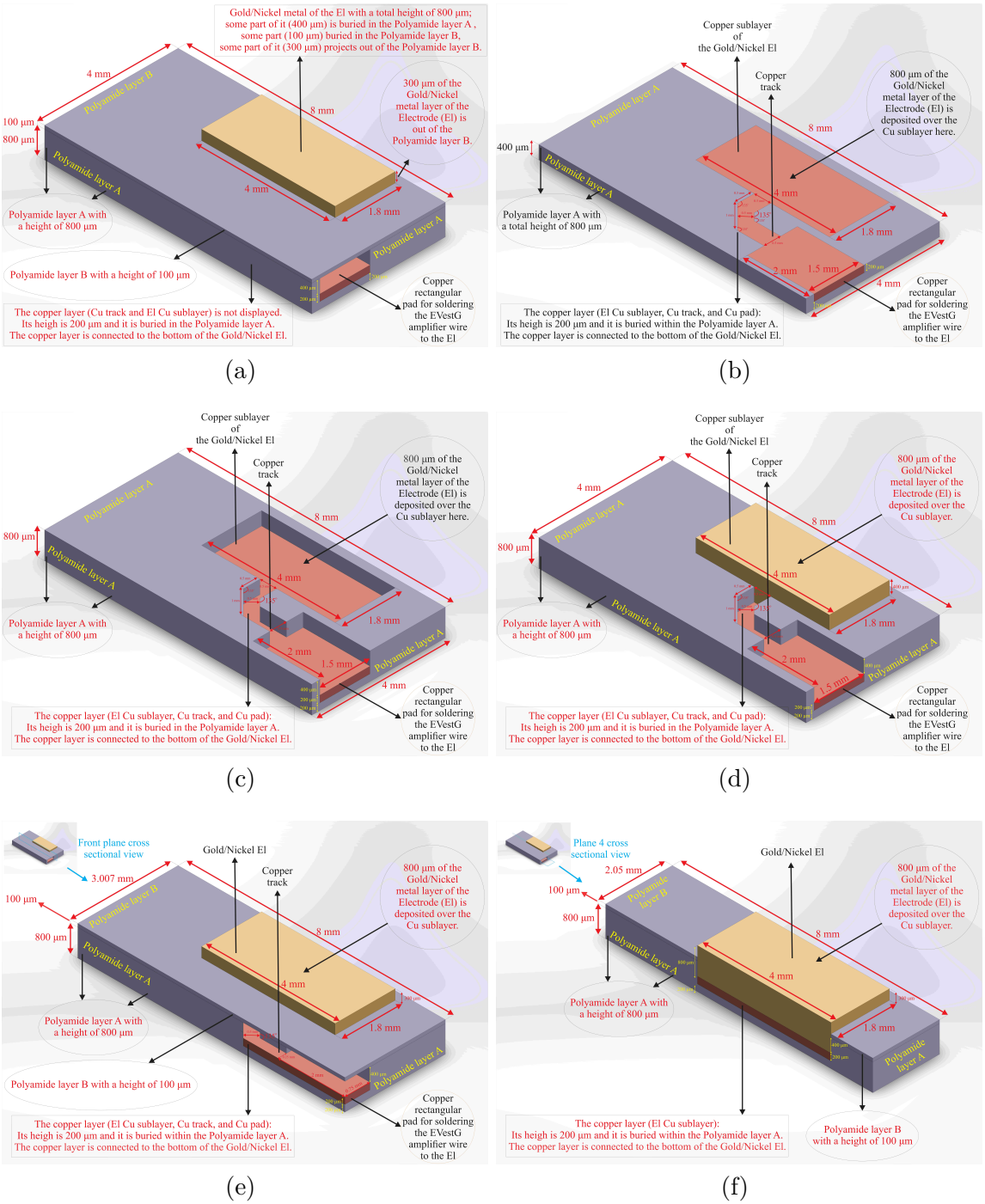

Figure 3.6: Passive electrode: the geometrical dimensions and cross-sectional views are presented.

covered with insulation painting over the copper tracks from the electrode pad to the soldering pad. However, this concept might be achievable via ink-jet silver droplet

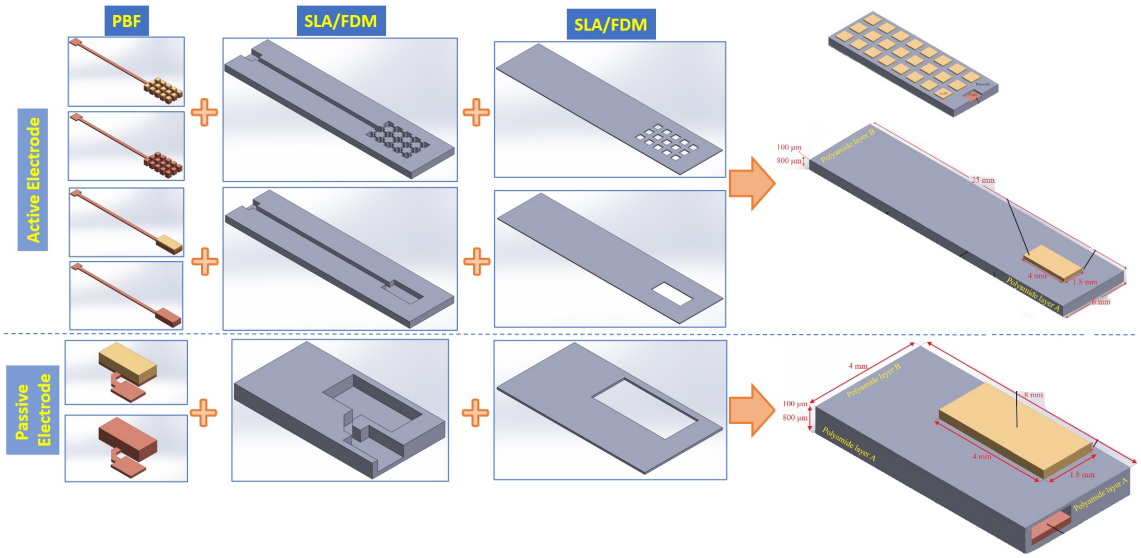

Figure 3.7: Application of 3D-printing technology to build the active and passive electrodes; the conductive (metal) and non-conductive (non-metal) parts of the active and passive electrodes can be 3D-printed by PBF or DMLM and SLA technologies, and be assembled afterwards.

3D-printing.

Regarding a potential usage of the electrode for EVestG application in future, one may explain the electrode surface area of $7.33\,mm^2$ as follows: imagine the conventional TM electrode (cotton-wool tip) to be a cylindrical shell and assume that 20° to 30° of the surface of the cylinder contacts the skin. Consider the length of the cotton-wool tip displayed in Fig. 2.4a to be about 4 mm. Presuming the electrode as a cylinder shell, which 30° of that contacts the canal, the electrode contact area will be equal to

$$\text{Area} = sl_c = r\theta l_c\,, \tag{3.3.1}$$

where s, l_c, r, and θ are the arc length, cylinder length (cotton-wool tip length), canal radius, and sector of the circle (cylinder base), respectively. Canal radius is

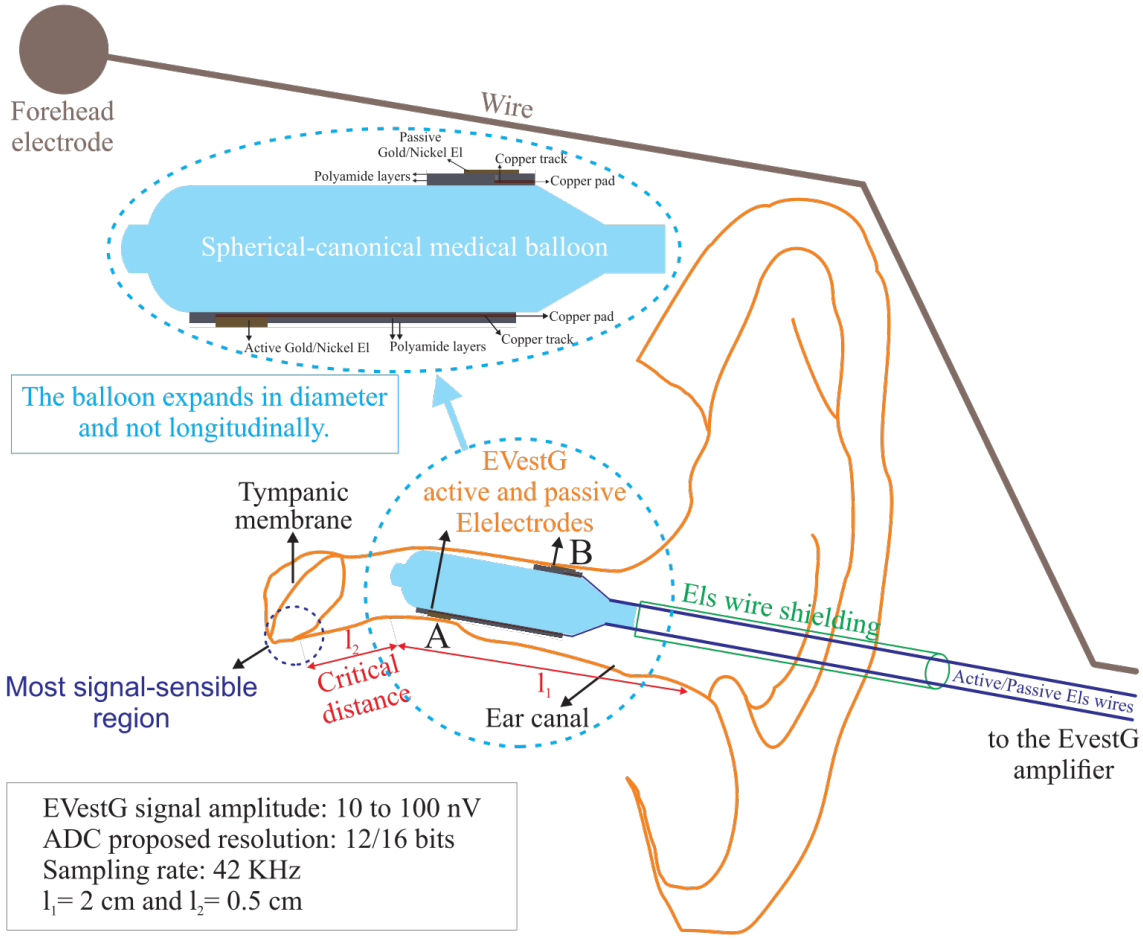

Figure 3.8: Conceptual schematics of a simplified solution for an electrode design with in-canal fixability and impedance reduction capability. The picture shows its future potential for EVestG recording; the active and passive electrodes are mounted (adhered to) around the medical balloon to contact with A and B points, respectively, when the balloon inflates.

$r = d_c/2 = 3.5$ mm. Consequently,

$$\text{Area}_{min} = 3.5 \times \frac{\pi}{6} \times 4 = \frac{7\pi}{3} \approx 7.33\, mm^2 \tag{3.3.2}$$

where $\theta = 30^o$. See Fig. 3.10.

Fortunately, some companies fabricate medical balloons according to desired features. Our survey possibly suggests the most conventional shapes, as illustrated in Fig. 2.2 or a combination of them. The balloon end shape near the sensitive areas could be selected out of canonical sharp/radius corners, and square/spherical



Figure 3.9: Application of (silver-droplet ink-jet) 3D-printing technology to build the active electrode; the attachment of polyamide substrate over the balloon membrane is challenging.

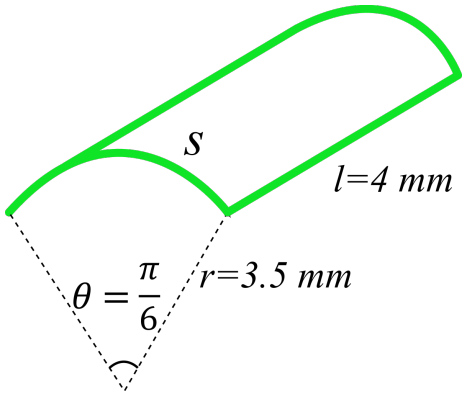

Figure 3.10: The electrode surface in contact with the canal can possibly be assumed to be a cylindrical shell with a length of 4 mm and a radius of 3.5 mm. The radius is half of the ear canal diameter.

ends. The latter seems less damaging. Figure 2.2m depicts a canonical-spherical medical balloon possibly proposed for actuation of the micro electrode, while Table 3.1 introduces its parameters. The freedom in shape design may facilitate electrode

Table 3.1: Values of the geometrical parameters for a typical balloon design (displayed in Fig. 2.2m): they are suggested for electrode actuation purposes, regarding the canal geometry (7 mm in diameter and 2.5 cm in length) and electrode sets dimensions in Fig. 3.5 and 3.6. One design question can be stated as how the radial and axial stresses, as well as burst pressure, function in the constrained parameters and material characteristics.

Parameter	Description	Parameter	Description
$d = 7\,mm$	Inflated diameter	$L = 2.5\,cm$	El mounting length
$L_t = 2.75\,cm$	Total length disregarding necks	$L_{pn} = 1\,cm$	Proximal neck length
$L_{dn} = 2\,mm$	Distal neck length	$\beta = 45^o$	Canonical angle
$d_{ip} = 1.2\,mm$	Internal diameter of the proximal neck	$d_{ep} = 2\,mm$	External diameter of the proximal neck
$t_{pn} = 400\,\mu m$	Wall thickness of the proximal neck	$t_{dn} = 400\,\mu m$	Wall thickness of the distal neck
$d_{id} = 1.2\,mm$	Internal diameter of the distal neck	$d_{ed} = 2\,mm$	External diameter of the distal neck
P_b	Balloon bursting pressure	$t_{eb} = 400\,\mu m$	Thickness of the expandable body

actuation for twisted canals. It is worthwhile to mention using a dog-bone balloon (or a dual balloon) such as Fig. 2.2g may appear beneficial as it provides independent inflatable substrates for active and passive electrode mounting.

Figure 3.11 proposes another approach to conform the electrode surface with the canal arch, to increase the contact probability, and to reduce the electrode fracture chance. It benefits a network of connected pads embedded in a polyamide *mattress*. The number of pad cells and their dimension should establish an overall area of about 7.33 mm^2.

Trying to obtain a more effective circular contact with the canal, Fig. 3.12 and 3.13 propose a ring of electrode pads circumferentially wrapped around the balloon, i.e., a sector of 360° or 300° is considered instead of the 30° cylindrical shell in Fig. 3.10. The ring of the electrodes can be fabricated by adopting the process displayed in Fig. 3.4.

In this approach, a 6 or 8 French (fr) size Foley balloon catheter or a PTCA dilation catheter might be exploitable to host the circumferential electrode pads and accommodate the electrode wire, CMOS camera sensor head, illumination LEDs, etc. The balloon material might be silicone, latex, and PET. The conformability of the balloon with the canal is significant, so an ordinary Percutaneous Trans-luminal

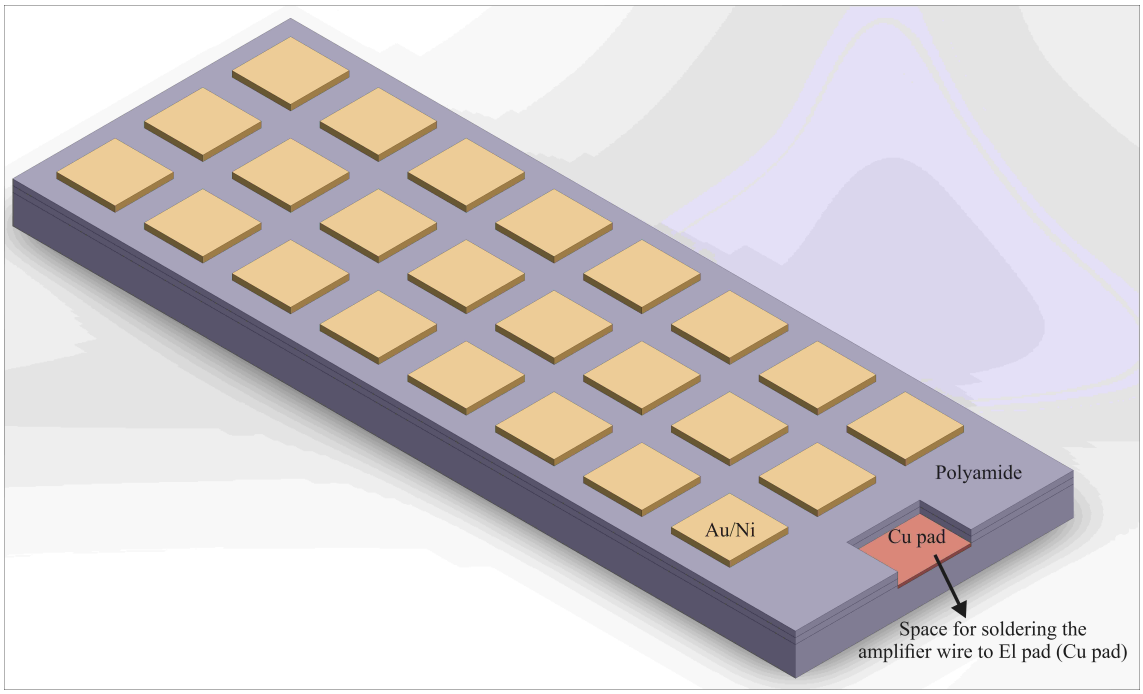

(a)

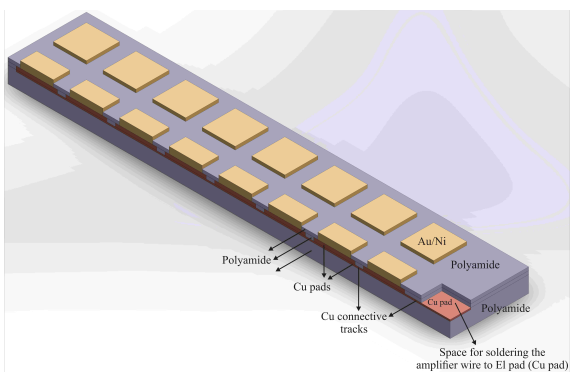

(b)

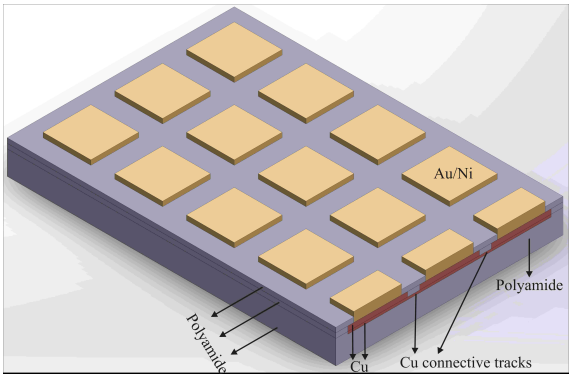

(c)

Figure 3.11: (a) A network of in-plane vertically and horizontally connected metal pads to increase flexibility, contact area and decrease fracture chance. The distribution enhances contact when the canal surface has roughness or corrugation. (b) and (c) Copper tracks connect the pads length and width-wise, respectively.

Coronary Angioplasty (PTCA) balloon may not be usable for our purpose. We may need a Foley balloon or another customized type of balloon. These are investigated in Chapter 4. See Section 4.5 for details.

Besides the MEMS fabrication process and 3D-printing, multi-layer flexible Polyamide a Printed Circuit Board (PPCB) or Flexible Printed Circuit Board

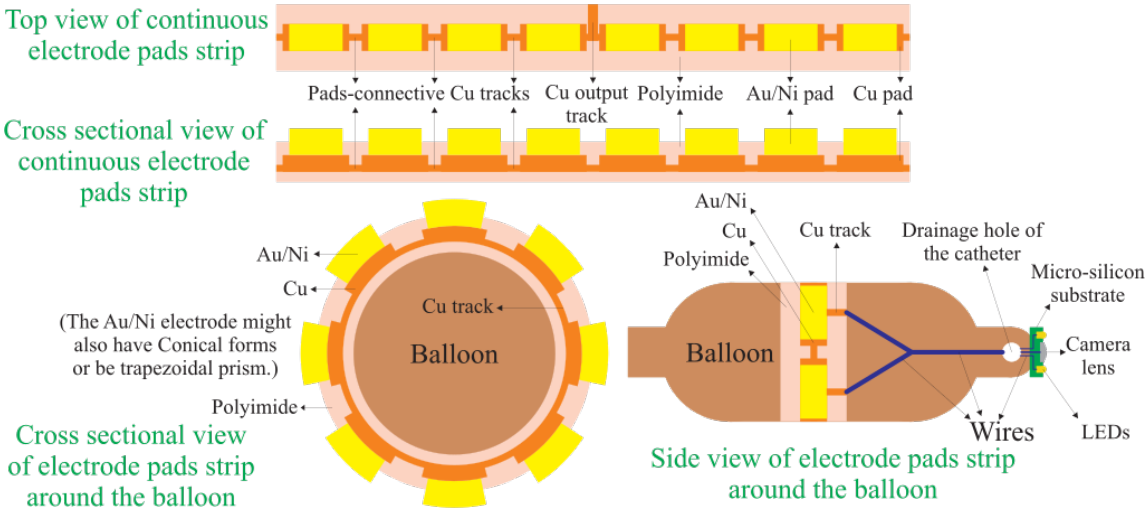

Figure 3.12: Conceptual schematics of electrode pads ring. The electrode pads strip is wrapped around the balloon. It is made up of polyamide substrate, copper tracks, copper pads, and gold/nickel pads. The pads are connected with copper tracks and are distributed in 360° to contact the canal circumferentially.

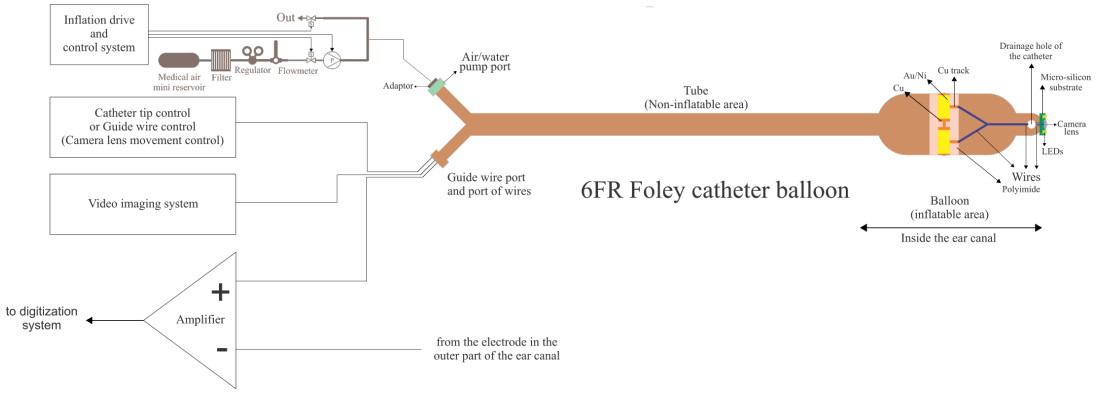

Figure 3.13: Conceptual application design of a balloon catheter for the electrode signal acquisition, using electrode pads ring.

(FPCB) (illustrated in Fig. 3.14) may be exploitable to construct insulated copper tracks, non-solder masked (non-insulated) rectangular (circular) pad with an area of about 7.33 mm^2 at one end of the copper track, and non-solder-masked small circular pad at the other end. Then, a rectangular pad/disc (with a typical thickness of 800 μm) might be 3D-printed or sputtered over the FPCB non-solder-masked rectangular pad to grow the electrode out of the FPCB. Sputtering mask may be challenging in this practice. The amplifier wire can be soldered (connected) onto the FPCB non-solder-masked small circular (rectangular) pad. If the electrode pad is

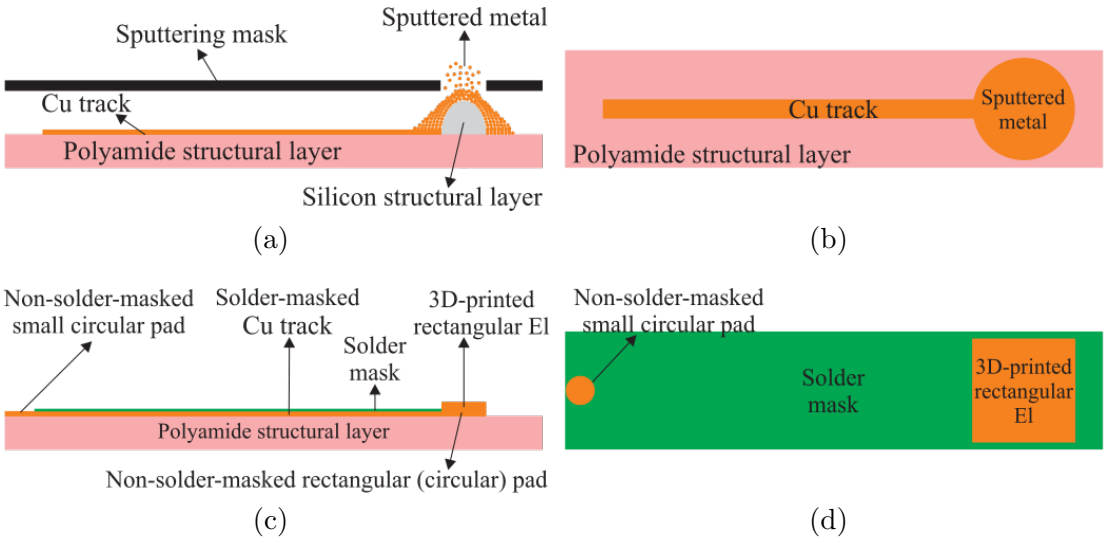

Figure 3.14: PPCB: metal is sputtered/3D-printed on the copper pad and track. In sputtering, the metal bumpy surface is fabricated over a silicon/plastic structural layer. The metal bump contacts the canal when the balloon inflates. The rectangular/circular pad area is 7.33 mm^2. (a) and (b) Sputtering, (c) and (d) 3D-printing.

sputtered as seen in Fig. 3.14a and 3.14b, we may have to cover the copper track manually with a bio-compatible insulation glue. It is worthwhile mentioning that the whole design of Fig. 3.14c and 3.14d can possibly be 3D-printed thoroughly from substrate to the outer touching electrode, in particular when grooves are needed for soldering the amplifier wire to the copper track small pad. It is important to prevent bumps on the soldering pad and track which spoil the electrode desired height.

The electrode mounted over the FPCB (in Fig. 3.14) or even over the active and passive electrodes proposed in Fig. 3.5 and 3.6 might be adopted as micro-needles to penetrate the canal wall to decrease contact impedance. One conventional way of building micro-needles can be based on doping silicon wafer, photolithography, silicon oxide growth, anisotropic KOH wet etching of silicon wafer to build pyramidal sharp structures, coating them with gold/titanium and copper to enhance electrical conductivity and biocompatibility, and reduce toxicity while penetrating the canal wall. Figure 3.15 proposes the process for such a purpose. The silicon wafer can be doped as an etch stop layer from one side. However, the maximum achievable height

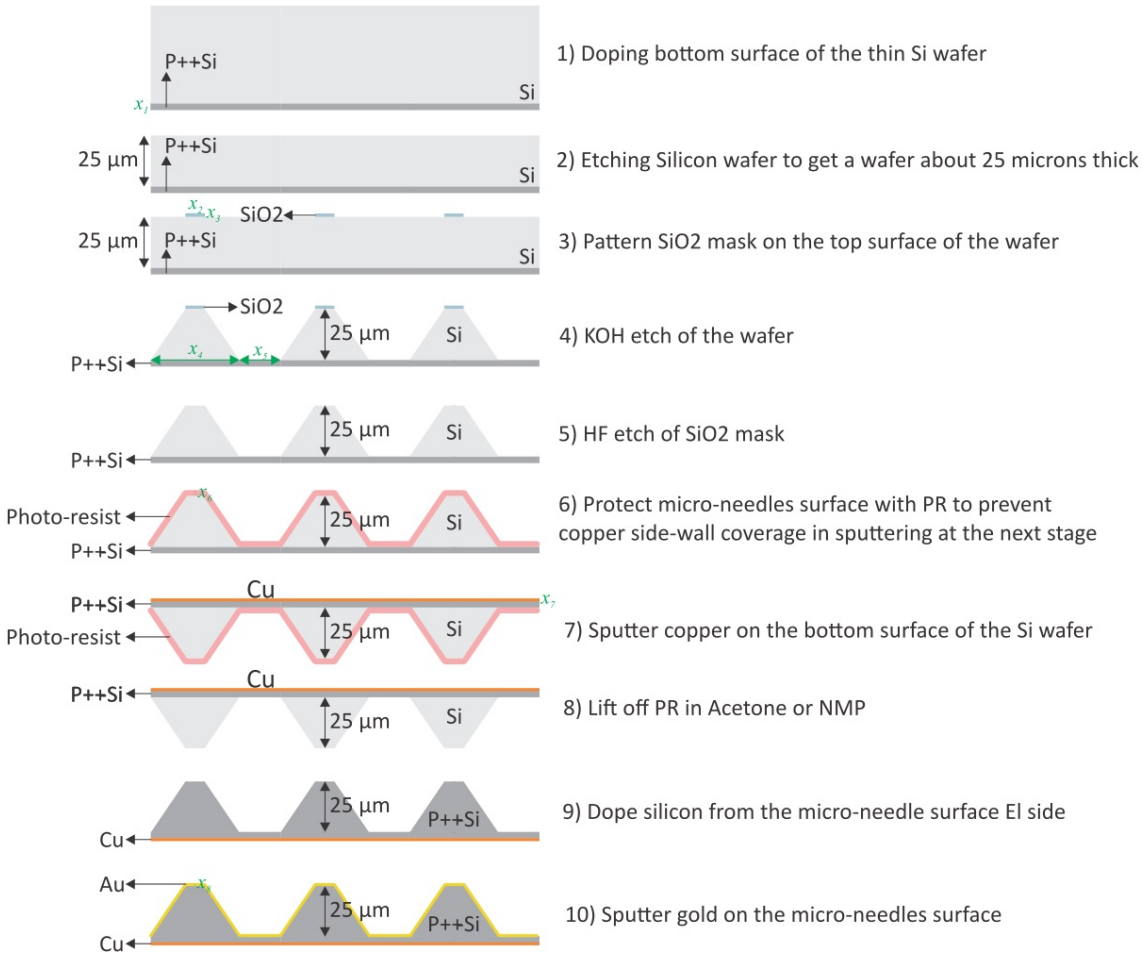

Figure 3.15: Process design of a MEMS micro-needle based on conventional techniques of photolithography, silicon wet etch and sputtering. The height value is just a typical one and not designed nor calculated.

in the etching process of this fabrication approach might be challenging. Moreover, the fabrication costs and required facilities are considerable, which results in the fabrication of high-resolution features.

3.4 Development of the tip of the unactuated cottonwool electrode

In addition to the design and fabrication of an inflatable electrode, developments to the structure of the unactuated silicone-tube wire cotton-wool electrode (passive

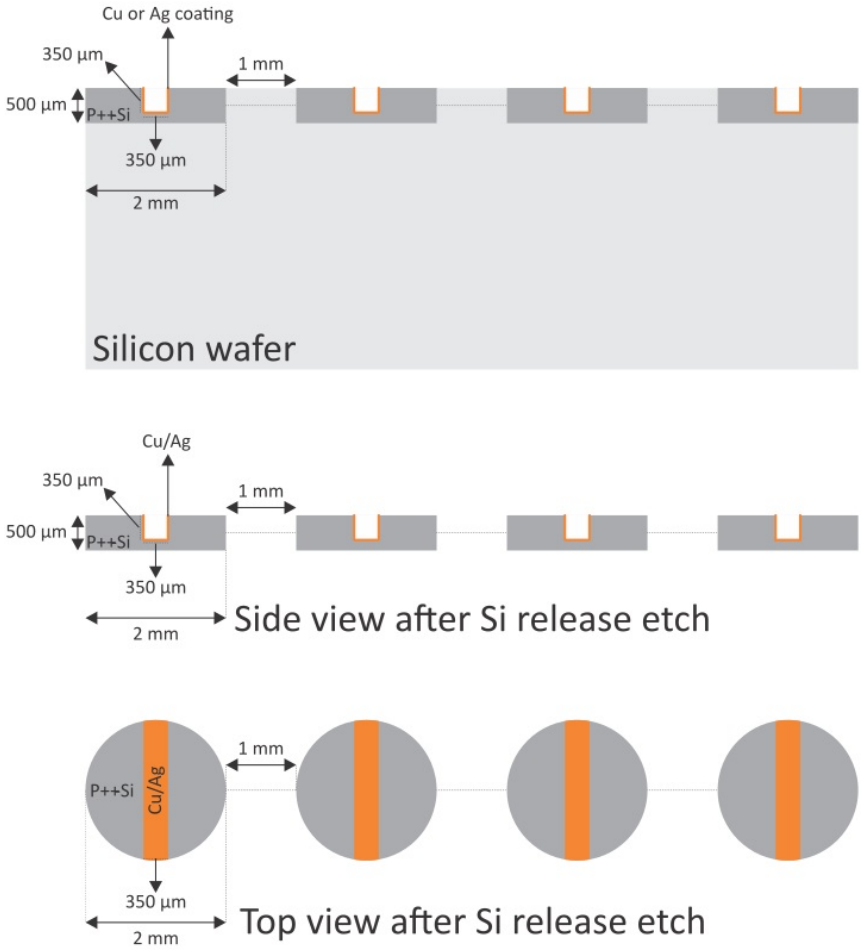

Figure 3.16: Micro-fabrication process of doped silicon discs without SiO_2 etch stop layer which is not time-efficient nor cost-efficient due to mm etch depth.

system) might be adopted as other approachable methodologies instead of the design and fabrication of single electrodes mounted over a balloon, which is basically different as an active system. This approach tries to focus on tackling possible defects with this structure. One of the probable shortcomings is the empty space or area (ring shape), which suffers from an inadequate conductive surface (capacitive area) or even small inductance with an undesired effect. Although these effects are not investigated in this thesis, some solutions are introduced theoretically which might be practically approachable in the future, and some others are implemented to handle the probable malfunctioning effects (See Section 4.3).

One of the suggested developments is replacing the empty ring-shape tip of the

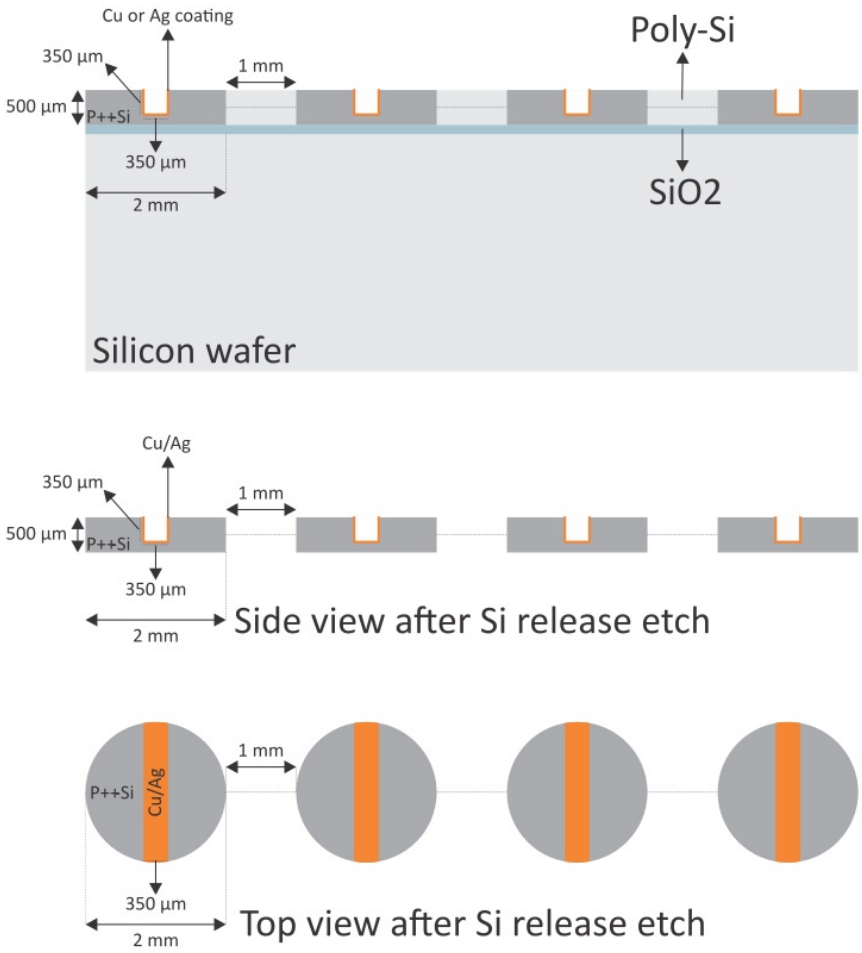

Figure 3.17: Micro-fabrication process of doped silicon discs with SiO_2 etch stop layer which is not time-effective nor cost-effective because of mm etch depth.

electrode (displayed in Fig. 2.4b) with a conductive small disc to fill the empty space, increase the effective capacitive area, and suppress the tiny coil effect. This disc can be non-metal and metal-coated later via sputtering. Figure 3.16 illustrates a typical fabrication process of such discs based on photolithography and doping disc volumes within the silicon wafer and then releasing them with KOH wet etch. Figure 3.17 describes a similar typical process on an SOI silicon wafer in which SOI can act as the etch stop layer.

The silicon discs in Fig. 3.16 and 3.17 need to be metal-coated to enhance conductivity. So, another solution might be building metal discs directly. Figure 3.18 displays the process of building such discs based on wet etching or DRIE of copper

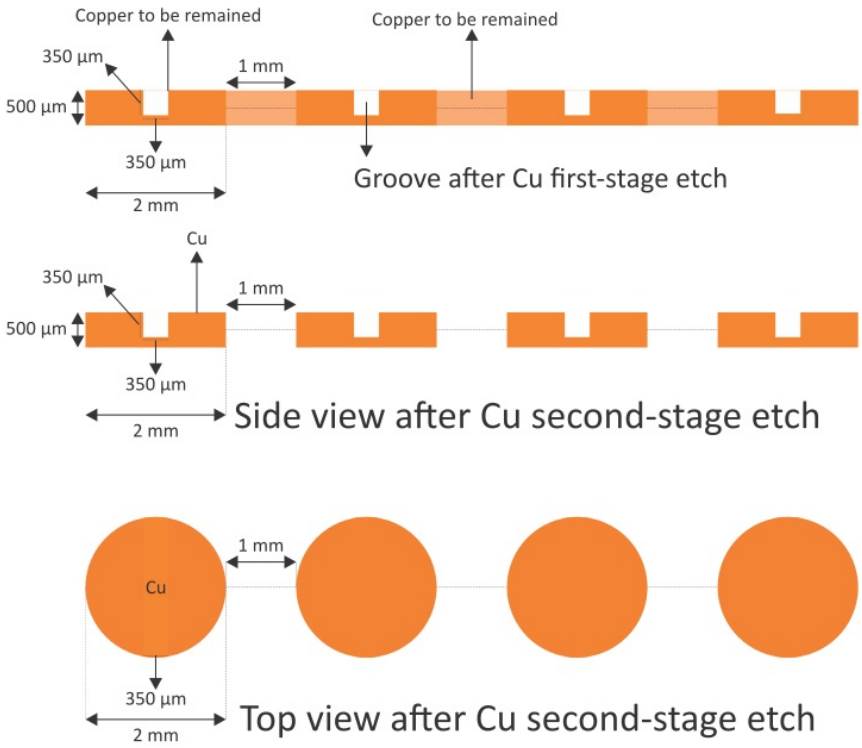

Figure 3.18: Micro-fabrication process of copper discs which is not time-efficient nor cost efficient due to mm etch depth of copper.

or gold plates. The processes in Fig. 3.16, 3.17, and 3.18 are time-consuming and cost-inefficient.

Fabrication of PDMS discs may be suggested to replace the metal discs and fill the space of the ring-shape tip of the unactuated wire cotton-wool electrode to reduce the costs of etching process in high aspect ratio. Figure 3.19 typically illustrates such a solution. It benefits using thinner copper/gold discs as the top and bottom covers of the PDMS central disc.

Regarding costs, time inefficiency, and complexity of the fabrication process discussed in this section (Section 3.4), we suggested or exploited and implemented other solutions to modify the tip of the unactuated electrode. They are shortly

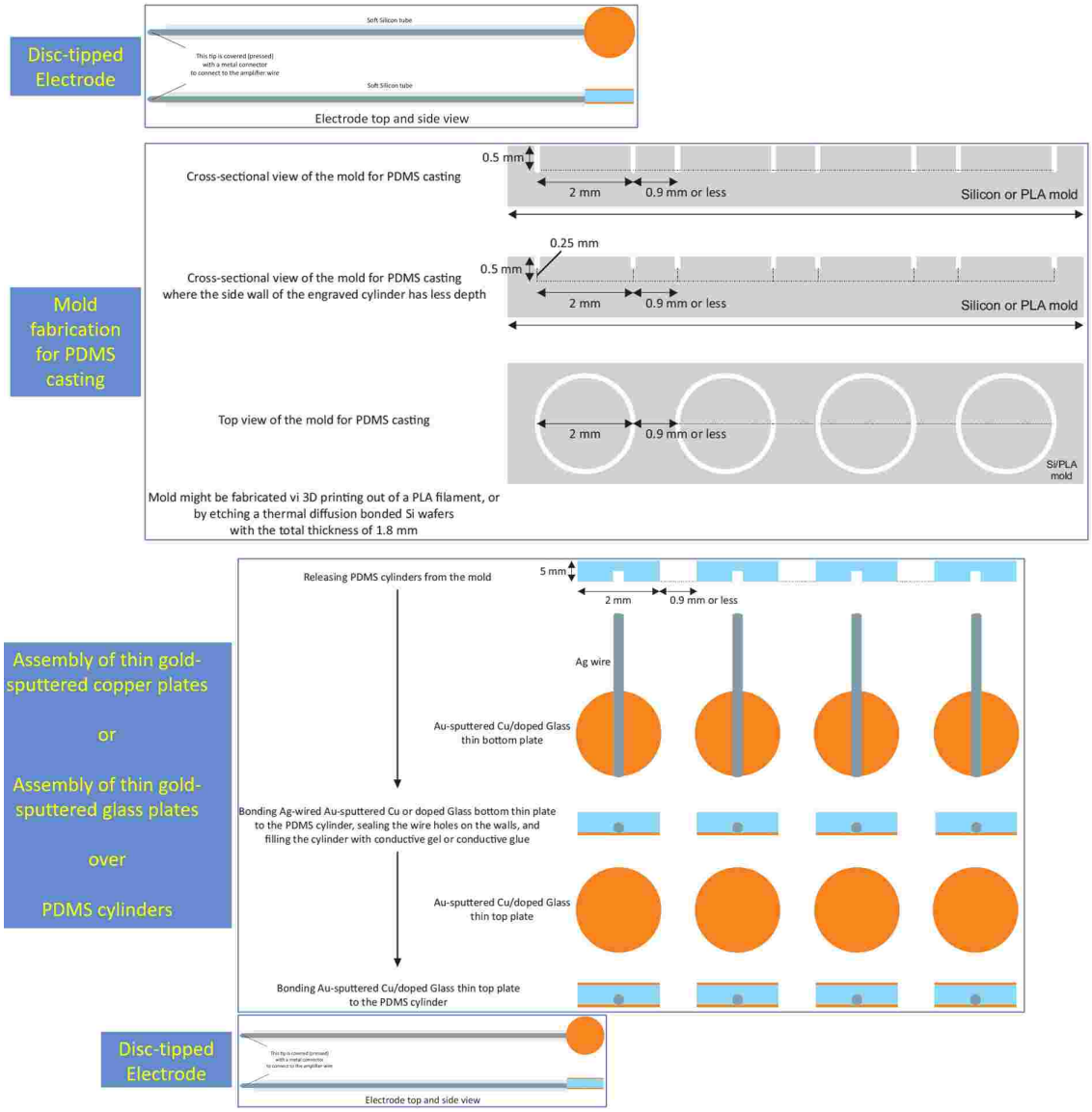

Figure 3.19: Fabrication process of PDMS metal-covered discs.

mentioned in Section 3.5 and completely explained (implemented) in Section 4.3. Simply, it is based on using copper balls or silver-sputtered balls and FPCBs.

3.5 Final practical adopted methodology to be implemented

Regarding cost-efficiency, time-efficiency, resources and our lab facilities, we have to transform the suggested methodologies and discussed approaches in Section 3.3 and 3.4 to more practical and feasible solutions. Our ultimate simplified practical solution to the design and fabrication of an inflatable electrode in Section 3.3, is comprised of the following five major parts, which are going to be implemented in Chapter 4:

- Exploitation of mostly a medical latex/silicone 6 or 8 fr Foley balloon catheter as the electrode actuation system instead of using the balloon proposed in Fig. 3.8 and 3.9,
- Design and fabrication of an FPCB electrode via flexible PCB design instead of MEMS fabrication process presented in Fig. 3.4,
- Fabrication of metal discs using metal disc cutters instead of fabrication processes proposed in Fig. 3.18,
- 3D-printing plastic micro-needles and coating them with conductive paint or via sputtering instead of the fabrication process put forth in Fig. 3.15,
- Fabrication of FPCB tips or copper/silver ball tips instead of the solutions proposed in Fig. 3.16, 3.17, 3.18 and 3.19 as developments to the un-actuated silicone-tube wire cotton-wool electrode structure.

The reasons in the itemized headlines as alternatives go as follows; however, the logic is clarified in detail in Chapter 4. First off, building medical balloons is a high-tech industry, and we did not have access to the machines for building and testing them. Outsourcing our design and ordering is time-consuming and costs remarkably for our prototyping purposes. We even sent one of the balloon designs to a company and

asked them to build it but it did not work out. We did not follow up either regarding the project timeline. So, we were compelled to search for medical balloons available on the market, and we are reassured about their bio-compatibility. We shall avoid re-inventing the wheel. Secondly, the conventional fabrication process of MEMS for building copper and nickel/gold polyamide electrodes costs too much. It is possibly time-inefficient, while flexible PCB technology vouches for building similar structures if the protruded electrodes are added later. Thirdly and again, MEMS silicon micro-needle fabrication also costs too much, but it can be replaced with cheap plastic 3D-printed micro-needles, which can be metal-coated relatively easily later. This seems more feasible and reasonable regarding the aspect ratio and size of the desired micro-needles for the first experiments. Lastly, the FPCB or copper/silver-ball tips are much easier to build than MEMS tips regarding the desired geometry and costs.

4

Fabrication and experimental set-ups

In this chapter, we report the fabrication process and final experimental set-ups prepared from the early stages of our research to the ultimate stage, which led to our final fabricated solution, regarding the methodologies trend presented in Fig. 3.1. It is reported chronologically. In detail, it mainly includes FDM 3D-printing, SLA 3D-printing, conductive paint application, conductive glue application, sputtering, flexible PCB design/fabrication, copper plate cutting and various kinds of catheter applications.

4.1 FDM/SLA 3D-printing of different basic plastic electrode models

First, we started using FDM or SLA 3D-printers (Fig. 4.1a, 4.1c, and 4.1e) of our accessible labs to investigate if we could 3D-print models similar to the ones presented in Fig. 3.5 and 3.6. We thought that, in case of reaching a fine-resolution 3D-printed part, we may be able to find and use PEDOT:PSS filaments/resin (as

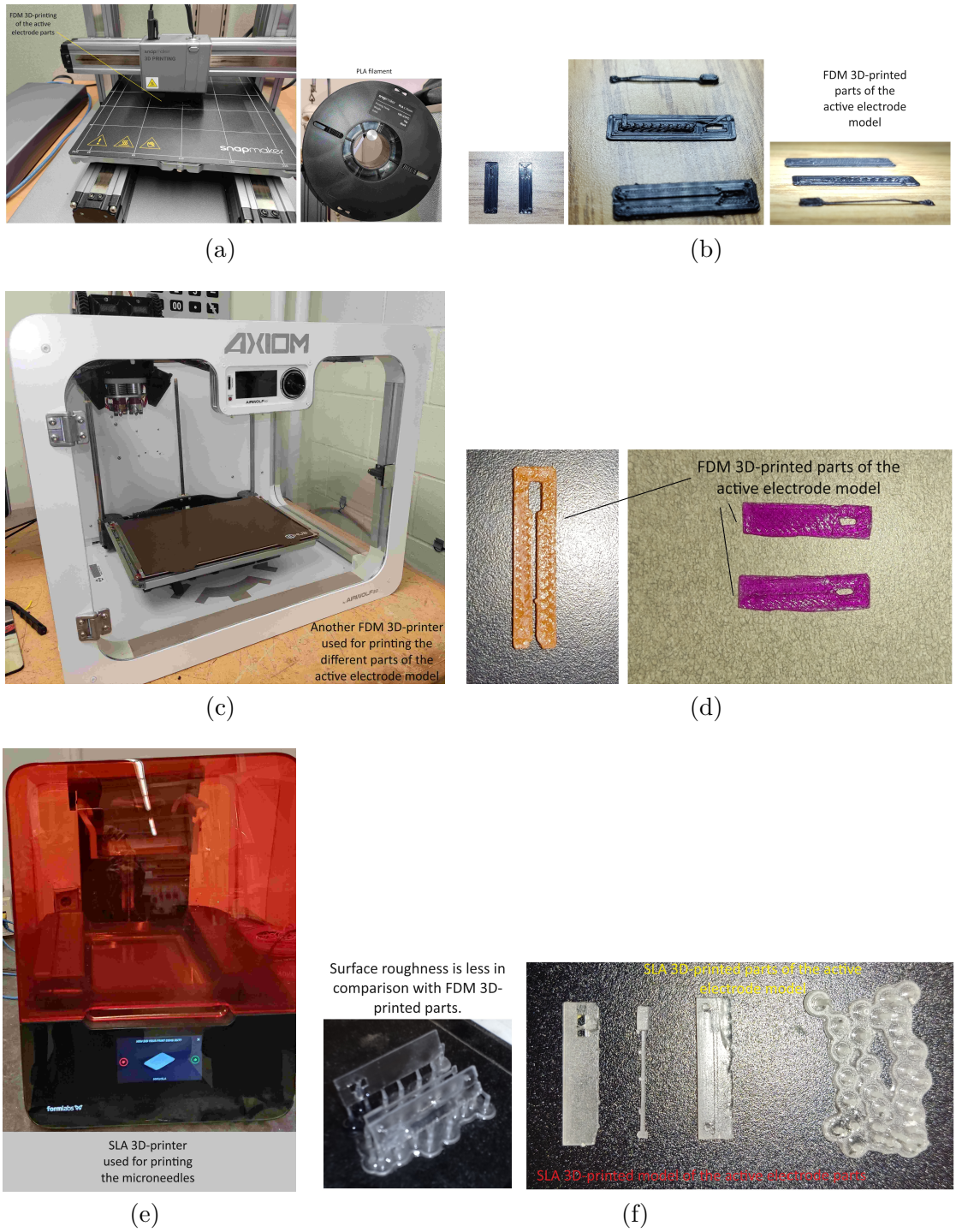

Figure 4.1: Plastic 3D-printed models: (a) Our lab FDM 3D-printer and (b) its printed models, (c) FDM 3D-printer in the Fabrication shop and (d) its printed models, (e) SLA 3D-printer in the Fablab and (f) its printed models. All these printed models are our attempts to build models similar to the active electrode in Fig. 3.5.



(a) (b)

Figure 4.2: Different filaments: (a) PLA, (b) TPU. They show rigidness and flexibility characteristics, respectively

conductive filaments/resin) to fabricate the electrode the easiest way. The FDM results are displayed in Fig. 4.1b and 4.1d, which show awful quality and surface roughness suffering from insufficient resolution. In contrast, the SLA 3D-printer yields demonstrate much-improved surface roughness and better quality (See Fig. 4.1f). However, PEDOT:PSS resin is required, which we could not access. That is the reason that led us to think about 3D-printing plastic models and coating them with conductive material/metal in our later trends. The PLA and TPU filaments used in printing our FDM models are displayed in Fig. 4.2, which are rigid and flexible types of filaments, respectively.

In addition to the 3D-printed models of the electrodes similar to Fig. 3.5 and 3.6, we also tried 3D-printing of pyramidal and conic micro-needle structures using FDM 3D-printer with TPU and PLA filaments. Figure 4.4 displays the TPU FDM 3D-printed micro-needles. Although we tried different small heights less than 3 mm and changed the parameters in the STL-to-Gcode conversion software, we could not obtain any acceptable 3D-printed model with the desired geometries. It is probably because of runny material of the filament which exacerbates the quality in small scale 3D-printing. This highlights the need for a 3D-printing technique based on instant curing (such as SLA) of the build material while working with flexible

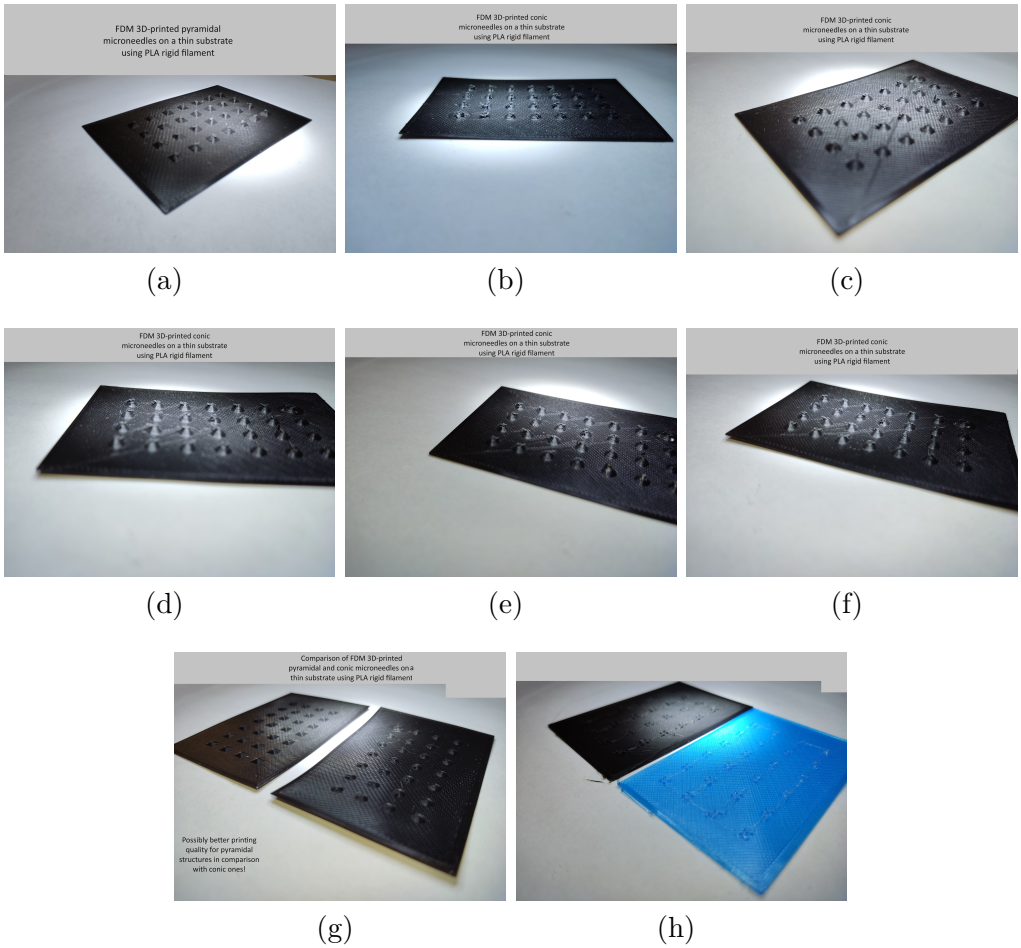

Figure 4.3: (a) to (g): PLA FDM 3D-printed pyramidal and conic micro-needles. (h) Comparison between TPU and PLA micro-needles; PLA 3D-printed features better than TPU ones.

material because cool-down time and nozzle movement cause deformation. Figure 4.3 depicts the PLA FDM pyramidal and conic 3D-printed micro-needle models, showing a better-desired shape but still unsatisfactory. Figure 4.3h illustrates them comparatively.

Better results of PLA FDM 3D-printing of micro-needles persuaded us to work on the parameters while generating the G-code from the STL file with the 3D-printer conversion software. Hence, we could 3D-print pyramidal micro-needle structures presented in Figure 4.5. We then cleaned the surface roughness, bumps and extra grass features under the microscope with tweezers. This parameters manipulation

may dramatically affect the printed part quality and surface roughness; see Fig. 4.5d. The quality is impaired due to increase of printing speed.

The FDM PLA 3D-printed pyramidal micro-needle we obtained did not have any resolution better than 4 mm square base and 2.5 mm (3 mm) height. The surface roughness was not satisfactory enough to deposit a nice quality metal layer or conductive painting on. Consequently, we switched to SLA 3D-printing. Figure 4.6 displays our SLA 3D-printed pyramidal micro-needles which show a dramatically controlled surface roughness compared to FDM 3D-printed microneedles.

4.2 Fabrication of wired copper-plate (disc) electrodes and their assembly on the Foley balloon catheter

In the next stage, we got focused on a simple way of fabricating a copper-plate (Cu disc) electrode instead of exploiting chemical wet etch or RIE of tiny copper plate or discs out of bigger metal plates, to obtain the high aspect ratio we were looking for. Thus, we exploited a cutting machine displayed in Fig. 4.7a. A sample result is presented in Fig. 4.7b. Another solution for building such copper or silver plates is using metal disc cutters for jewellery fabrication. They can even make round-shaped discs with a diameter of 2 mm. The wire was soldered onto the electrode backside (Fig. 4.7c). Then we tried to assemble the set on a 14 fr-size Foley balloon catheter following the idea of exploitation of an inflatable electrode substrate or actuator. Figure 4.7d demonstrates various parts of a Foley balloon catheter including drainage port, air (inflation) port, inflatable membrane (balloon part), drainage holes (eyes) and catheter tip. Figure 4.7e to 4.7k illustrate the fabrication of the whole design, approaching simple wire and copperplate electrode usage. We can see the undesired

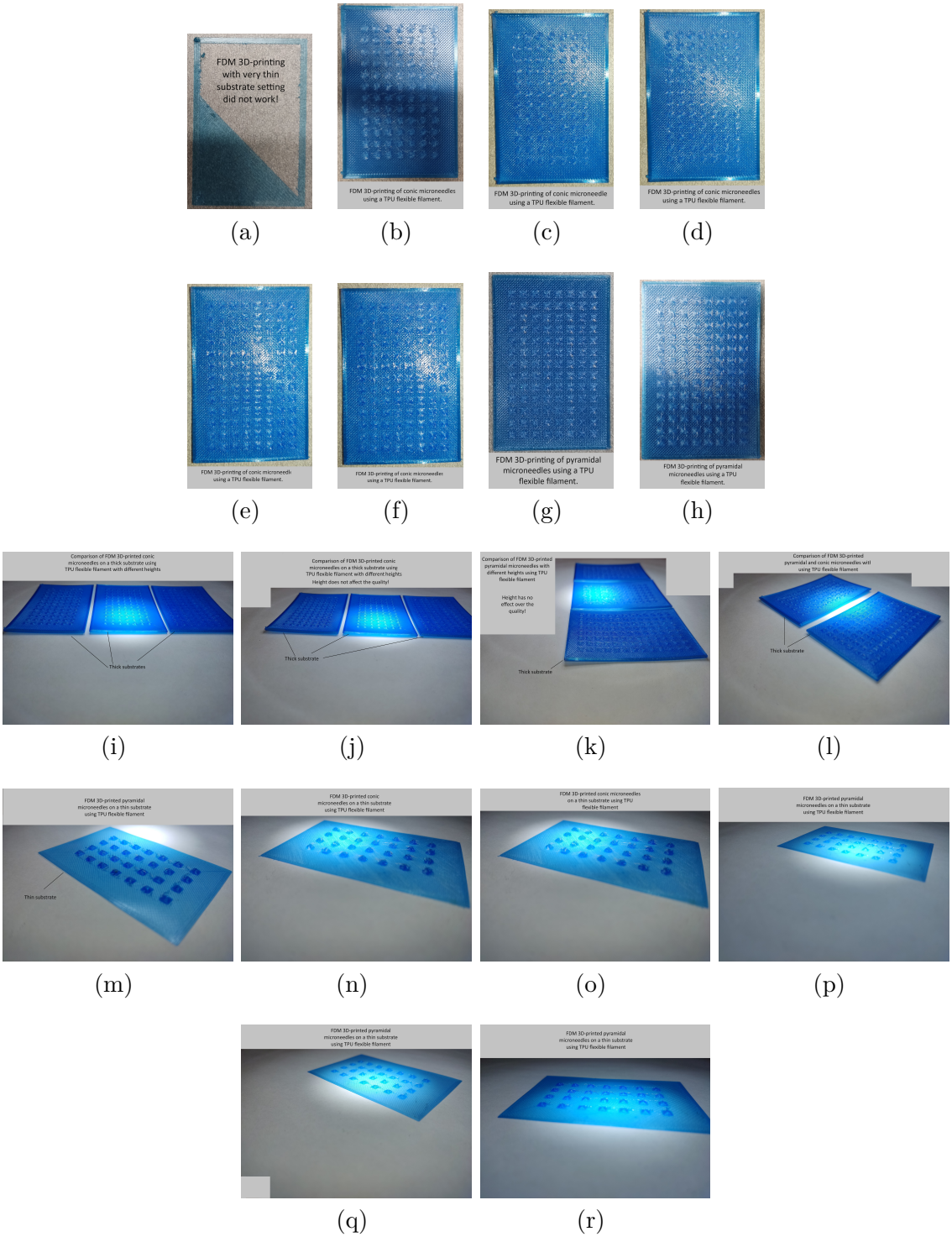

(a) (b) (c) (d)

(e) (f) (g) (h)

(i) (j) (k) (l)

(m) (n) (o) (p)

(q) (r)

Figure 4.4: Trying to FDM-3D-print micro-needles on flexible TPU; the results are not satisfactory even after changing parameters while converting STL file to G-code. Some of the pictures are the same and presented from different light angles to enhance illustration. Some are pyramidal, conic, and dots. Different sizes have been also tried.

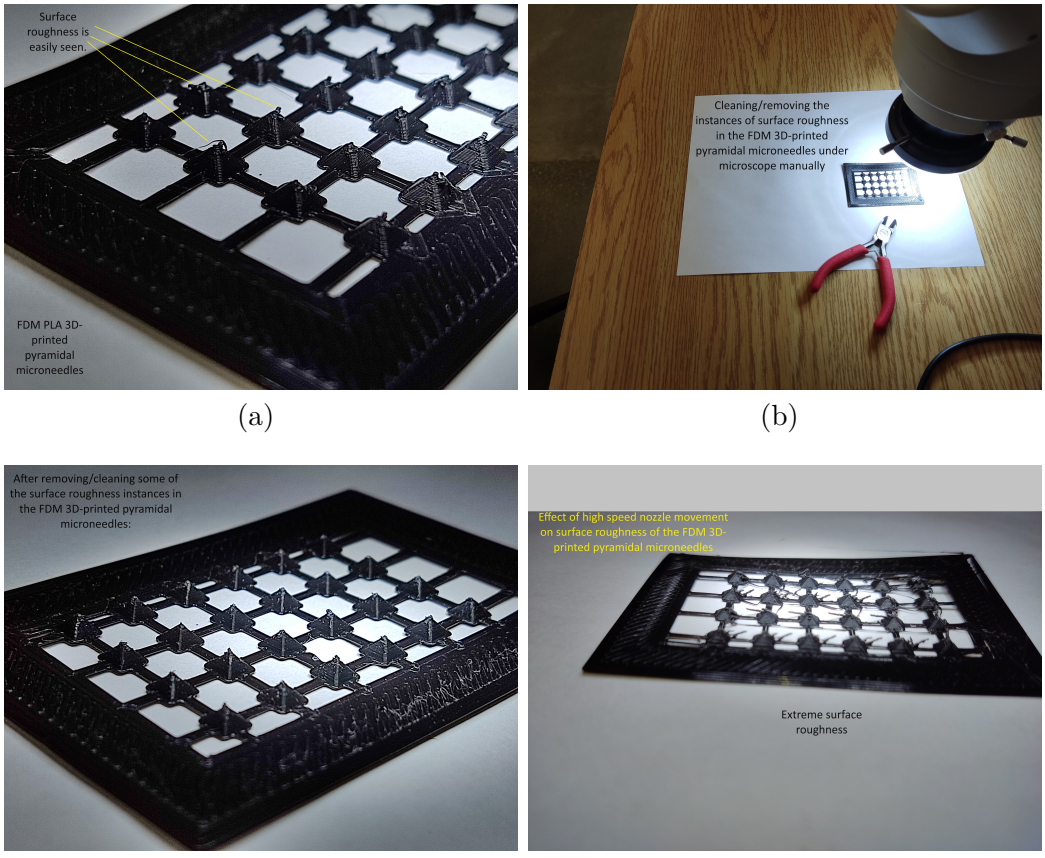

(a) (b)

(c) (d)

Figure 4.5: FDM 3D-printed pyramidal micro-needles with a base of 4 mm by 4 mm after setting the parameters in the process of conversion of STL file to G-code. (a) Before trimming under microscope (b) Trimming under microscope. (c) After trimming. (d) The result of bad setting of parameters in the file conversion process.

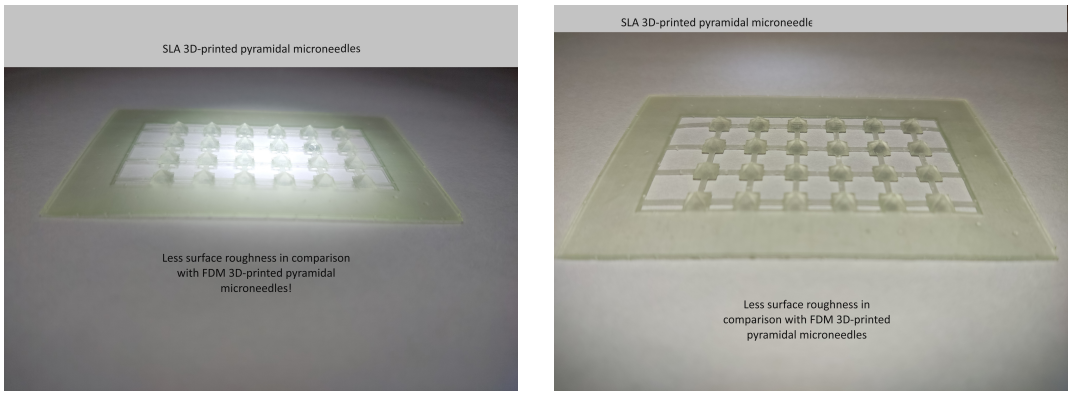

(a) (b)

Figure 4.6: SLA 3D-printed pyramidal micro-needles with a base of 4 mm by 4 mm.

bending of the catheter due to the wire attachment while using two wires to return the electrode plate to its initial place after the balloon deflation; see Fig 4.7l, 4.7m, and 4.8c for the double-wire single copper-plate electrode. Figure 4.8a and 4.8b display the catheter when a single-wire copper-plate electrode is assembled over the balloon. One of the problems is that the electrode does not return to its initial place after deflation. Sharp corners and the rigid body of the electrode remain, as do other problems.

To assess the contact quality of the double-wire and single-wire copper-plate electrodes, actuated with the Foley balloon catheter, with the canal, we 3D-printed some approximate ear canal FDM PLA/TPU models. Some of them had cylindrical shapes, some resembled big ear canal models, and some were built similar to the size of a typical actual ear canal model. They are depicted in Fig. 4.9. A few of them were equipped with some copper foils and wiring connections to emulate the active and passive sites of the signal inside the canal (symbolized with points A and B in Fig. 2.5). The test set-up is straightforward and depicted in Fig. 4.10. It is mainly comprised of an oscilloscope (output), function generator (input), and a FDM-3Dprinted approximate ear canal model equipped with active and passive copper foils. The Foley balloon catheter assembled with the copper-plate electrode is inside the approximate ear canal model. No signal was observed on the oscilloscope while the balloon was deflated, but a stable output on it after inflation; the signal was robust against swinging and manual disturbing movement of the canal model (e.g. motion artifact). Figures 4.10a to 4.10d illustrate single-wire copper-plate electrode tests, whereas Figures 4.10e to 4.10i show double-wire copper-plate electrode testing. The double-wire type shows better off-state while the balloon is deflated compared to the single-wire type. At this stage, we concluded that the wired copper-plate electrode does not meet our expectations, leading us to consider flexible PCB as a serious alternative to facilitate electrode up-and-down movement or its return to its

initial place.

4.3 Modification of the unactuated electrode tip

Meanwhile, we considered making developments to the tip of the un-actuated silicone tube wire cotton-wool electrode (similar to the currently used EVestG electrode), filling the empty ring-shaped area. We designed square-shape FPCB electrodes in KiCad with an area of 4 mm by 4 mm (bigger than $Area_{min}$). They are displayed in Fig. 4.11a, 4.11b and 4.11c. Then, the FPCB electrode is perforated, cut, trimmed and put inside the silicone tube of the un-actuated wire electrode; see Fig. 4.11d, 4.11e, 4.11f and 4.11g. Afterwards, some qualitative tests were done comparing to the conventional electrodes, as seen in Fig. 4.11h and 4.11i. The FPCB remarkably shows less attenuation and noise. To cope with sharp edges, one may use the modified round-shaped designs in KiCad as presented in Fig. 4.11j and 4.11k, ranging in various sizes from 2 mm to 4 mm in the circle diameter ($\{2, 2.25, 2.5, 2.75, 3, 3.25, 3.5, 3.75, 4\}$), possibly suitable for different canal sizes.

Following the idea of modification of the tip of the electrode, we thought about how to make the FPCB in Fig. 4.11f more three dimensional to increase touch probability and decrease damage of sharp edges. We exploited some holed copper 2 mm and 3 mm balls. Then, we tried to change the coating of the balls and to make it similar to the electrode wire so the balls were silver-coated via sputtering in the clean room as seen in Fig. 4.12. The sputtering process is explained in details in Section 2.2.1 and 4.7 in theory and practice, respectively. Afterwards, electrodes with copper and silver 3 mm balls and twin 2 mm balls were fabricated. See Fig. 4.13. Figure 4.14 shows double FPCB tip for better double-sided canal touch which we built simultaneously.

To test the frequency response of the modified electrode with different tips,

including copper/silver ball and FPCB tips, we set up a simple series of experiments that gave white noise and sinusoidal waveforms as inputs to the fabricated tips. They are illustrated in Fig. 4.15. The results for the FPCB electrode are presented in Fig. 4.16. The experiment frequency plots for the copper/silver ball electrodes are exhibited in Fig. 4.17. The cotton-wool tip went under test, yielding plots in Fig. 4.18. We did not do quantitative tests because the qualitative comparison of all these figures leads us to conclude that the FPCB and copper/silver ball electrodes provide less attenuated and noisy interface in signal acquisition. In other words, it was the only hypothesis which we intended to verify possibly enough at this stage.

4.4 Assembly of the FPCB electrode on the Foley balloon catheter

Exploiting the fabricated FPCB electrodes and solving the problems of the single wire copper-plate electrode over the balloon, we mounted the FPCB electrode with different kinds of glue over the Foley balloon catheter. However, this design suffers from the problem of the glue curling up under the FPCB after deflation. The fabrication process and the issues are illustrated in Fig. 4.19. It is worth mentioning that the FPCB can still be used without glue, showing better performance compared to the single-wire copper-plate electrode due to flexibility which causes the electrode to return to its initial place after deflation.

Solving the tip problem, we discovered that the catheter tip can be cut up to the balloon. We also tested double-sided glue tape under the FPCB and it showed less curl-up. However, we did not have access to a tape with enough thinness, see Fig. 4.20. As seen, the curl-up still grows the electrode tip or diameter and prevents easy insertion into a small diameter canal.

4.5 Assembly of the FPCB electrode on the PTCA balloon catheter

Following our fabrication journey, we tried another type of catheter a typical PTCA balloon catheter. Unfortunately, it is not conformable at all with a curved diameter changing (or funnel-shaped) canal, though it shows fantastic strength while inflated and has high bursting pressure. Its tip is sharp and not reducible without damaging the balloon in contrast with the non-damageability of the balloon in Foley types after tip-cut. Figure 4.21 depicts the assembly of the FPCB over the PTCA balloon using elastic bands and handling its sharp tip with a cut Foley latex tip. The figure proves the non-functionality of using such a catheter for our purpose.

4.6 Assembly of FPCB, copper-plate and ball electrodes over pediatric/neonatal Foley balloon catheter and camera at its tip

The Foley balloon catheters used in previous stages of fabrication were 14 fr-size which is too big for insertion into small-diameter canals (e.g. 7mmdiameter) and not applicable for human studies, though possibly suitable for animal research. Hence, we tried to find neonatal or pediatric Foley balloon catheters whose size measure mostly 6 and 8 fr. A typical silicone Foley balloon catheter is shown in Fig. 4.22a and 4.22b. We also checked how much we could cut the catheter tip to make the balloon closer to the end of the canal. Unlike the latex type, we have some limitations but it seems that the tip can be shortened enough for our purpose; see Fig. 4.22c. The FPCB perforation is a rectangle and we need to cut the margins of the FPCB under microscope (Fig. 4.22d and 4.23). Cutting of the catheter tip should be done carefully

not to damage the inflated balloon. Trimming of the FPCB and the catheter tip can be done under microscope. The balloon inflation can also be controlled to a lower volume.

Being concerned with having more control over electrode insertion, we investigated the usage of a micro camera at the tip inside the catheter tube. We searched for an imaging sensor with suitable dimensions (diameter less than 1 or 2 mm) and found out that OVM6948 and OVM6946 CMOS sensors are ideal for our purpose. The sensor head and its strands of wires can be accommodated inside the catheter tube. Since it costs money, we 3D-printed the camera head model, cut the 8 fr-size latex Foley balloon catheter tip, and verified whether it could host the CMOS sensor or not. The answer is positive. Our trial is illustrated in Fig. 4.24.

Presenting a more developed and practically feasible design, we fabricated a more evolved electrode set. It is mainly comprised of a 6 fr-size silicone Foley balloon catheter, an FPCB mounted over the balloon (as the passive electrode), and a copper ball electrode (as the active electrode) at the tip of the catheter. The fabricated structure and its status inside an approximate ear canal model is presented in Fig. 4.25. The copper ball electrode is a holed 2 or 3 mm ball which soldering the wire into it without sharp edges can be challenging without using an oven and via using an ordinary soldering station. For professional assembly, one may need micro-fixation tools.

For adding more height (thickness) to the FPCB, we soldered the copper plate (disc) electrode on the FPCB. It is seen in Fig. 4.26, adding a thickness of 520 μm. The more the height is, the less the conformability will be. However, the FPCB reverse capability is still sustained.

4.7 SLA 3D-printing of micro-needle electrode and its conductive/metal coating

We also continued developing the main idea of the thesis, which is to build a conductive (metal-coated) plastic micro-needle. As our first and simplest solution, we approached spray-painting of the plastic SLA-3D-printed micro-needle (displayed in Fig. 4.6 or 4.27e) with a silver conductive paint (Fig. 4.27a). Due to safety issues and uniform spraying, we built a box (Fig. 4.27b, 4.27c and 4.27d) since we could not access a suitable painting chamber. The result is seen in Fig. 4.27f and 4.27g. We did not use another type of conductive paint displayed in Fig. 4.27h, which we had access to in our lab because its spray application was impossible, and we had to use a swap or paintbrush. The paint-brush brings about the non-uniform coating.

Conductive paint applied to the coating mentioned above is not biocompatible. Moreover, the painted micro-needle is too big and unsuitable for our target application. Hence, we approached two other solutions. First off, we redesigned micro-needles to be SLA-3D-printed with pyramidal and conic structures on a square base with an area of $16\,mm^2$ and $4\,mm^2$ with a sweeping height ranging from $0.1\,mm$ up to $1.5\,mm$. They are depicted in Fig. 4.28. Secondly, all the SLA3D-printed features (including features in Fig. 4.27e and 4.28) were silver-sputtered in the clean room for 4.5 minutes, providing a power of 30 watts. The temperature of the chiller was set to 5^oC to prevent the plastic from melting in the chamber. The deposited silver layer thickness is about 450 nm. Figure 4.31 and 4.32 include some pictures of the process and the results (silvercoated micro-needles). The sputtering process stages for the machine of our lab go as follows (regarding Fig. 4.31):

1. Turn on the valves of all the five gas supply cylinders which are located out of the sputtering room.
2. Turn on the chiller which is located out of the sputtering room and set its

temperature to 5^0C , and then go to the sputtering room.

3. Turn on the CDA and N_2 gas valves on the wall inside the sputtering room.
4. Turn the rotary switch to manual state on the top left metal panel.
5. Make sure all the manual control switches on the top left metal panel are off.
6. Fix the sample (micro-needles) on to the substrate, load the substrate into the chamber, align the substrate, switch the substrate rotation on for one cycle of rotation, turn off the substrate rotation, and close the chamber door.
7. Turn on the rough switch on the top left metal panel and wait until the chamber pressure is below 100 mTorr (the chamber is roughed out); it may take a few minutes. Then, turn it off.
8. Turn on the high-vacuum switch on the top left metal panel and wait for one hour.
9. Turn on the ion gauge on the gray left panel, wait until the pressure is below 10 μTorr, and turn off the ion gauge.
10. Turn on the Ar gas valve on the wall.
11. Turn on the Ar gas switch on the black left panel.
12. Turn on the mass flow controller switch on the black left panel.
13. Press the throttle button on the metal right panel.
14. Select the desired magnetron on the right metal panel (press orange circle key A to ON which is related to silver).
15. Select the DC/RF switch to DC state on the right metal panel.
16. Turn on the substrate rotation on the right metal panel.
17. Turn on the power supply and set the output power knob to 30 Watts.
18. Turn on the output (start) button of the power supply and wait for 1 or 2 minutes to sputter over the shutter.
19. Turn on (upward position) the desired target switch (shutter switch) beside the orange circle key A and wait for 4.5 minutes (sputtering process time) to

sputter over the sample until deposition is done.

20. Turn off the power supply (press the stop button).
21. Turn off the mass flow controller switches on the black left panel.
22. Turn off the Ar gas switch on the black left panel.
23. Turn off the magnetron switch on the metal right panel.
24. Turn off the shutter switch (downward position) on the metal right panel.
25. Turn off the substrate rotation (downward position).
26. Turn off the Ar gas valve on the wall.
27. Turn off the high vacuum switch on the top left metal panel and wait for 5 seconds.
28. Turn on the vent switch on the left metal panel and wait until the pressure rises up to $7.6 \times 10^{+2}$ Torr.
29. Open the chamber door and remove the sample out.
30. Close the chamber door.
31. Turn on the rough switch on the top left metal panel and wait until the pressure is below 100 or 70 mTorr.
32. Turn off the rough switch on the top left metal panel.
33. Turn off the rotary switch on the top left metal panel.
34. Turn off the CDA and N_2 gas valves on the wall.
35. Turn off the chiller out of the sputtering room.
36. Turn off the valves of the gas supply cylinders out of the sputtering room.

4.8 Fabrication of Foley balloon catheter-based electrodes with various μEl configurations

During the sputtering process, we used up our time to work on our idea of development and fabrication of inflatable electrode system using 8 fr-size latex

Foley balloon catheters, FPCB electrodes, copper/silver ball tip electrodes, and illumination adds-on. Figure 4.33, 4.34, and 4.35 demonstrate different configurations of these designed and fabricated electrode systems. Some of them are equipped with both active and passive electrodes while some only had active electrodes. The ball tips (as active electrodes) had different size or were single/double/thriple configured to increase/enhance contact modality. In some configurations, the FPCB were double (balloon top and bottom side) to expand contact area as well. The idea of passing the fibre optic strands through the hole of the ball electrode was also implemented to provide illumination; however, the light generated was not sufficient. All the configurations and geometries were placed inside the FDM 3D-printed approximate ear canal models to assess the placement of the fabricated electrode system visually and verify its contact modality roughly and macroscopically.

Likewise, Figure 4.36, 4.37, 4.38, and 4.39 illustrate developed inflatable electrode system using 6 fr-size silicone Foley balloon catheter, FPCB, copper-plate electrode, copper/silver ball electrode tip, cotton-wool tip, and illumination LED.

Figure 4.40b and 4.40c display an inflatable electrode system with three different active electrodes to increase electrical contact and reduce impedance in an omnidirectional manner, using an 8 fr-size latex Foley balloon catheter, copper ball tip electrode, micro-needle, and FPCB. Figure 4.40a shows the attachment process of the micro-needle over the FPCB of the balloon, using epoxy silver-conductive glue.

Being concerned with fabrication of an inflatable electrode system with both active and passive FPCB electrodes, we assembled the system depicted in Fig. 4.41. It takes advantage of using a dual balloon 16 fr-size Foley balloon catheter or dog-bone structure to inflate each FPCB electrode independently. Its size is too big and it may be suggested for animal study.

4.9 Measurement of the impedance of micro-needle electrodes vs balloon pressure variation

In the final stages of our research, we assembled different types of electrodes over a latex Foley balloon catheter including FPCB electrodes, rigid copper-plate (Cu-disc) electrodes, FPCB-based micro-needles, and cotton-wool electrodes. As mentioned in the previous section, the assembly process of the micro-needles over the FPCB to build FPCB-based electrodes is done using epoxy silver conductive paste (binary agents), illustrated in Fig. 4.43. Then, we approached testing the impedance of the fabricated electrode on a skin phantom while increasing the pressure of the inflated electrode substrate. For a straightforward and accessible test, we measured the resistance of the two diagonal points of a hydrated skin phantom inside a cylinder via a multi-meter. Two FPCBs mounted over a 14 fr-size latex Foley balloon catheter probed the two points. We increased the balloon volume by the syringe through the catheter air (inflation) port. We could decrease the measured DC resistance from infinity (several MΩs) to 2 MΩ, including approximate decreasing values of 21, 8, 4, 3, 2.7, and 1.8 in MΩ. Figure 4.42 displays the experiments and the read-out values for increased volumes of the injected air into the balloon.

Although the previous experiment, resistance variation measurement against the injected air volume, vaguely proves supporting role of pressure in impedance decrease, it is not valid in terms of AC measurement and does not provide usable stable data for analysis. Consequently, we designed another set of experiments in which both DC and AC measurements could be assessed to evaluate the electrode interfacing impedance more accurately and reasonably. The interfacing impedance of the two electrodes, contacting the two diagonal points of the hydrated skin phantom accommodated inside the cylindrical canal, was measured via the establishment of the circuit presented in Fig. 4.44b using the tools in Fig. 4.44a. The circuit implementation is

demonstrated in Fig. 4.44c and Fig. 4.44d for AC and DC measurements, respectively. The impedance is calculated via the following circuit analysis:

$$-V_{in} + R_e(t)i(t) + 1000i(t) = 0 \tag{4.9.1}$$

or

$$-V_1 + R_e(t)i(t) + V_2 = 0\,. \tag{4.9.2}$$

Considering $V_2 = R_2 i$ and $R_2 = 1000$, one may calculate the resistance (impedance) of the electrodes interface via the following equation:

$$R_e = \frac{V_1 - V_2}{V_2} \times 1000\,. \tag{4.9.3}$$

Assuming R_e not to be time-variant in stable experimental conditions and regarding sinusoidal input of V_{in}, the Phasor relations exist and the impedance absolute value will be calculated as follows:

$$|Z_e| = \frac{|V_1 - V_2|}{|V_2|} \times 1000\,. \tag{4.9.4}$$

The AC test was done for the following frequencies: $f_1 = 600Hz$, $f_2 = 2.2kHz$, $f_3 = 2.8kHz$, and $f_4 = 4.2kHz$. The measured interfacing impedances were plotted in Fig. 4.46 to 4.56. Before doing these set of experiments, we verified the skin phantom frequency response; see Fig. 4.45. The actual human body skin is comprised of three anatomical layers of the epidermis, dermis and the hypodermis. The dermis contains muscle fibres, some sweat glands, hair strands/follicles, blood capillaries, and sensors (neurons). Hair follicles, neurons, and blood capillaries also exist in hypodermis. Hence, the phantom probably may not mimic a close behaviour of the actual skin. One of the well-known approximate models of the actual skin is a low pass filter; a circuit of a resistance in series with an impedance which consists of

another resistor in parallel with a capacitor. In AC (sinusoidal) and DC tests of impedance, V_1 was set to (read as) 4.08 V and 9.8 V, respectively. The frequencies are selected regarding two points: 1) The EVestG signal bandwidth is about 5 kHz. 2) The selected frequencies are significant components in the EVestG signal frequency spectrum and their possible attenuation is of our concern. 600 Hz is a harmonic of the power line frequency of 60 Hz and so is 4.2 kHz. The given frequency range also covers a discrete frequency range from low (DC) to high frequencies within the 5-kHz frequency bandwidth.

AC test for the electrodes inside a cubic canal (instead of a cylindrical canal) was also done to compare the FPCB and micro-needle electrodes to assess their performance on a flat surface instead of a curved surface. The results are displayed in Fig. 4.58 to 4.62.

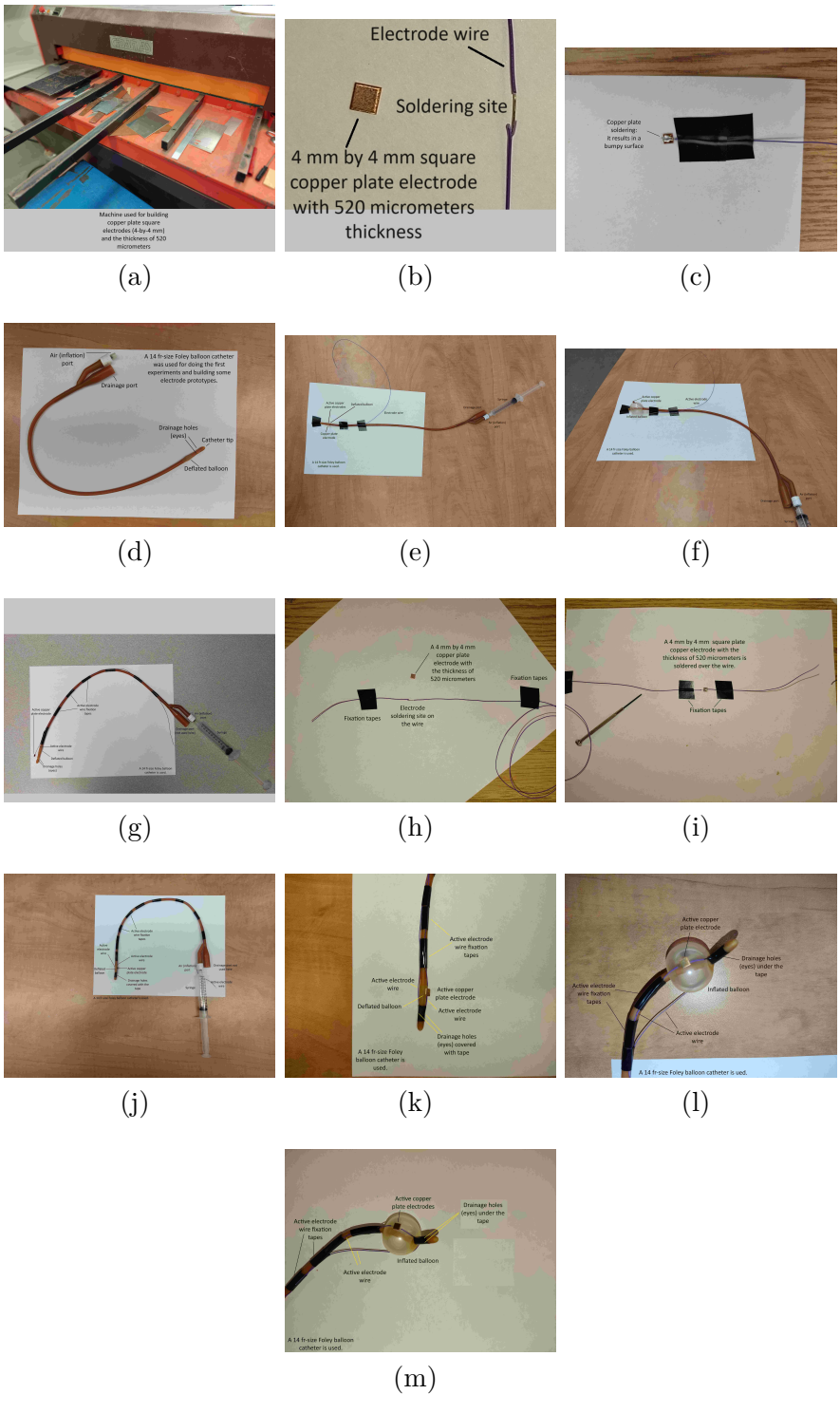

(a) (b) (c)

(d) (e) (f)

(g) (h) (i)

(j) (k) (l)

(m)

Figure 4.7: Fabrication process of an electrode using copper (Cu) plate (disc) and Foley balloon catheter: (a) Equipment for cutting tiny Cu plates. (b) Cu-plate electrode with an area of 4 mm by 4 mm and thickness of 0.52 mm. (c) Cu-plate electrode soldering to the wire. (d) 14 fr-size Foley balloon catheter. (e) to (g) Assembly of the electrode on the balloon. (h) to (i) Soldering Cu-plate electrode onto the middle of the wire. (j) and (k) Cu-plate electrode assembled over the balloon. (l) and (m) Inflation of the balloon.

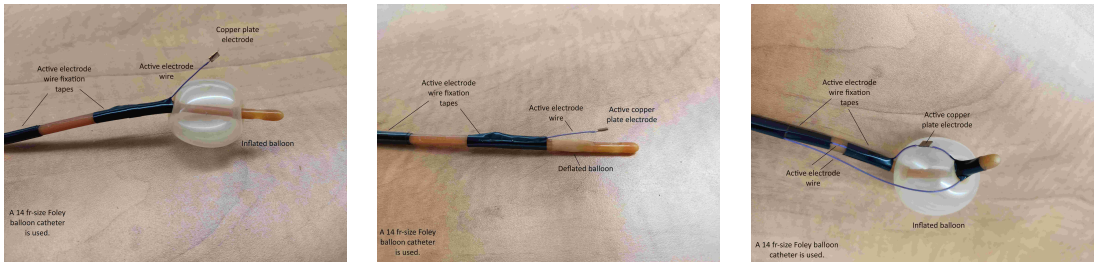

(a) (b) (c)

Figure 4.8: 14 fr-size balloon catheters equipped with copper-plate wire electrodes.

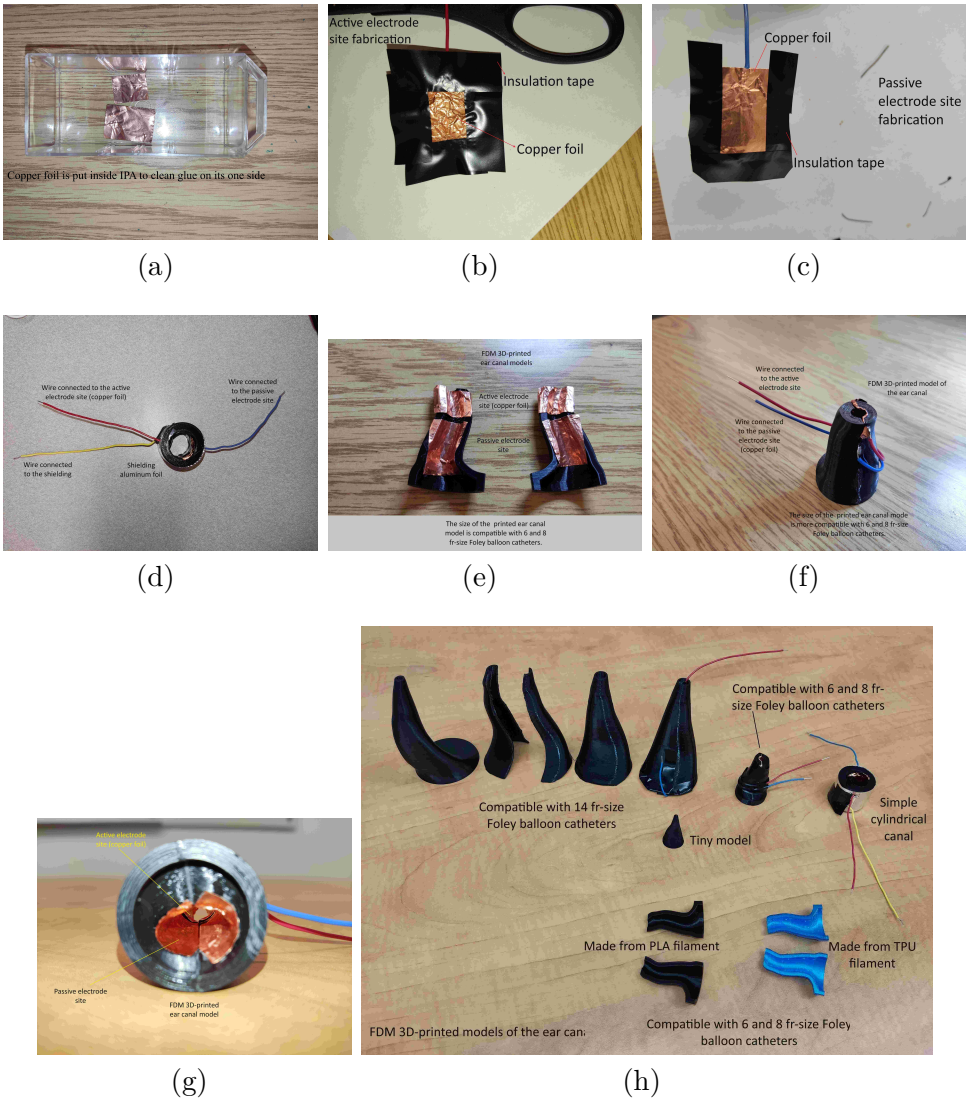

(a) (b) (c)

(d) (e) (f)

(g) (h)

Figure 4.9: (a) to (g) Fabrication of approximate ear canal models with different sizes to test the Foley balloon catheter-based electrodes: (h) Approximate ear canal FDM 3Dprinted models.

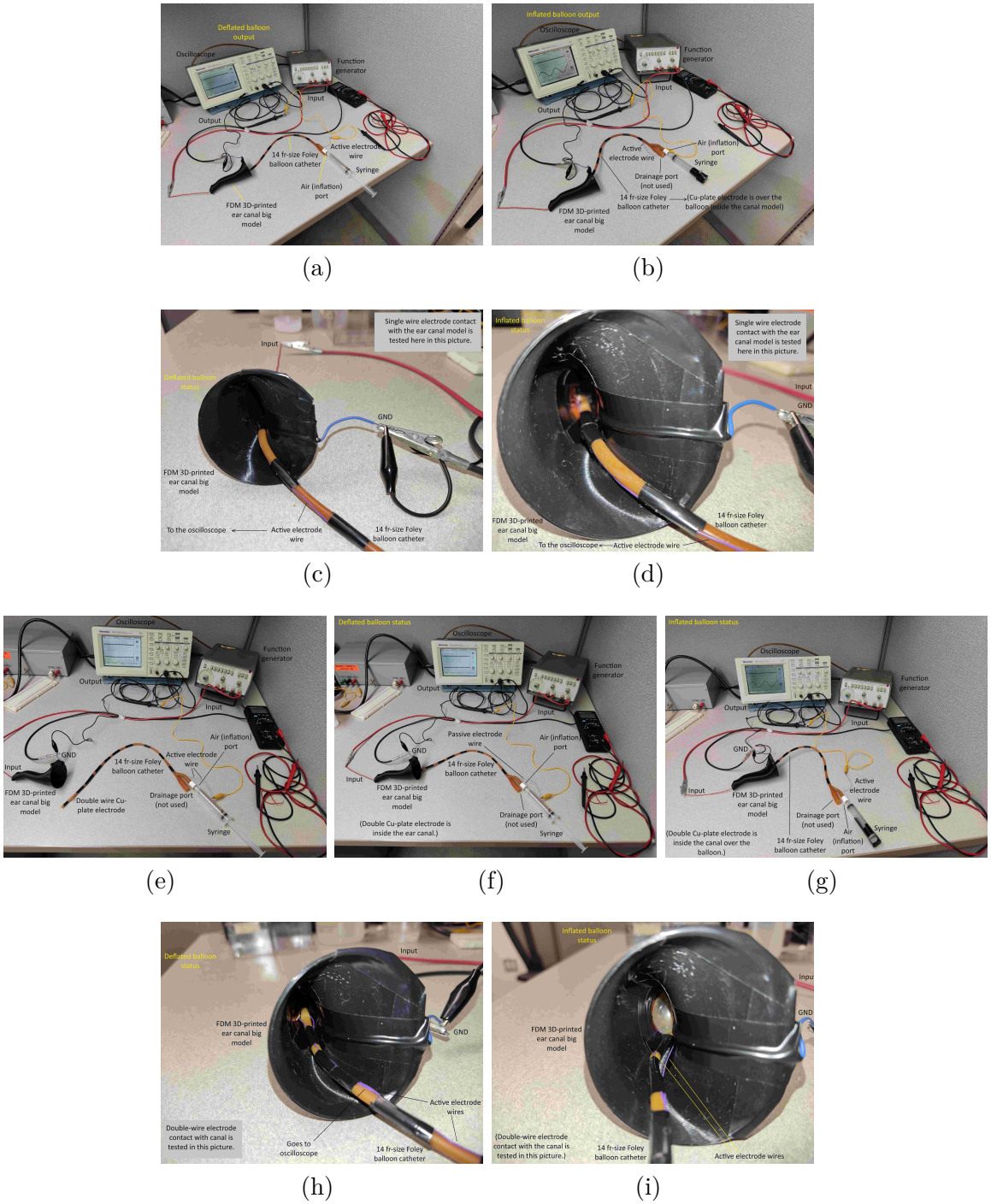

Figure 4.10: Test of the copper-plate (disc) electrode assembled over the Foley balloon catheter inside the approximate ear canal model.

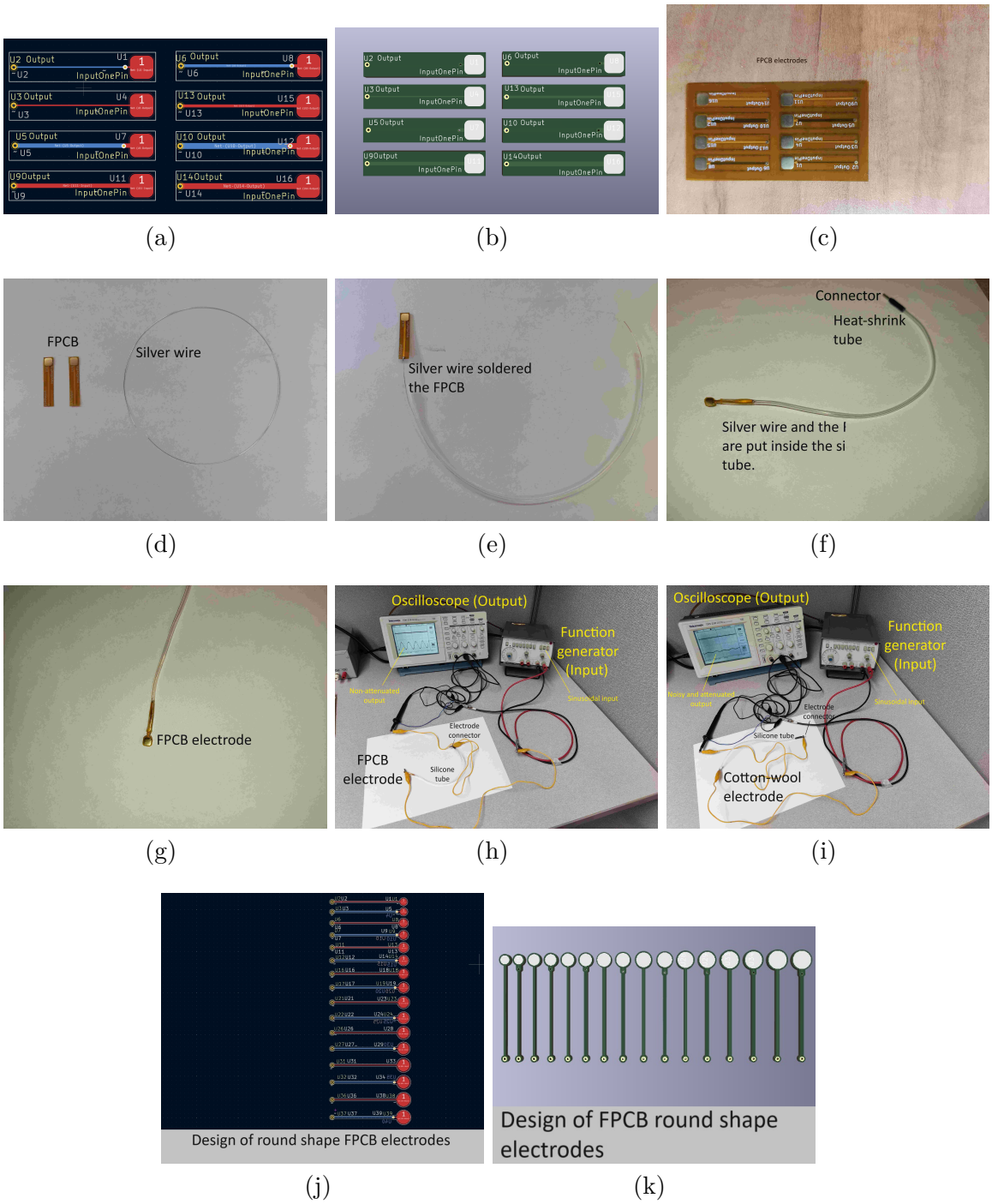

Figure 4.11: (a) and (b) FPCBs designed in KiCad. (c) Fabricated FPCBs each with a contact square pad of 4-by-4 mm. (d) to (g): FPCB electrode; development to the current electrode. (h) and (i): Comparison between the FPCB-tipped electrode and the cotton-wool-tipped electrode. (j) and (k): Design of double-sided round-shape electrodes in KiCad with different areas.

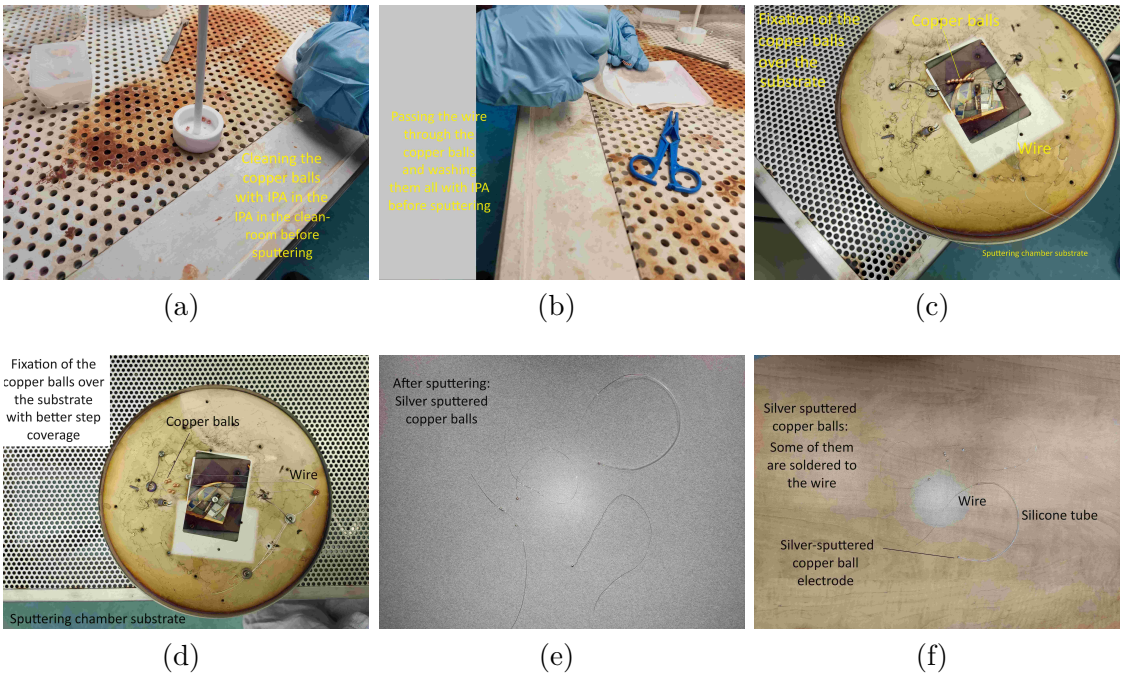

Figure 4.12: Sputtering silver over the copper balls to be used as a new tip for the unactuated silicone-tube wire electrode.

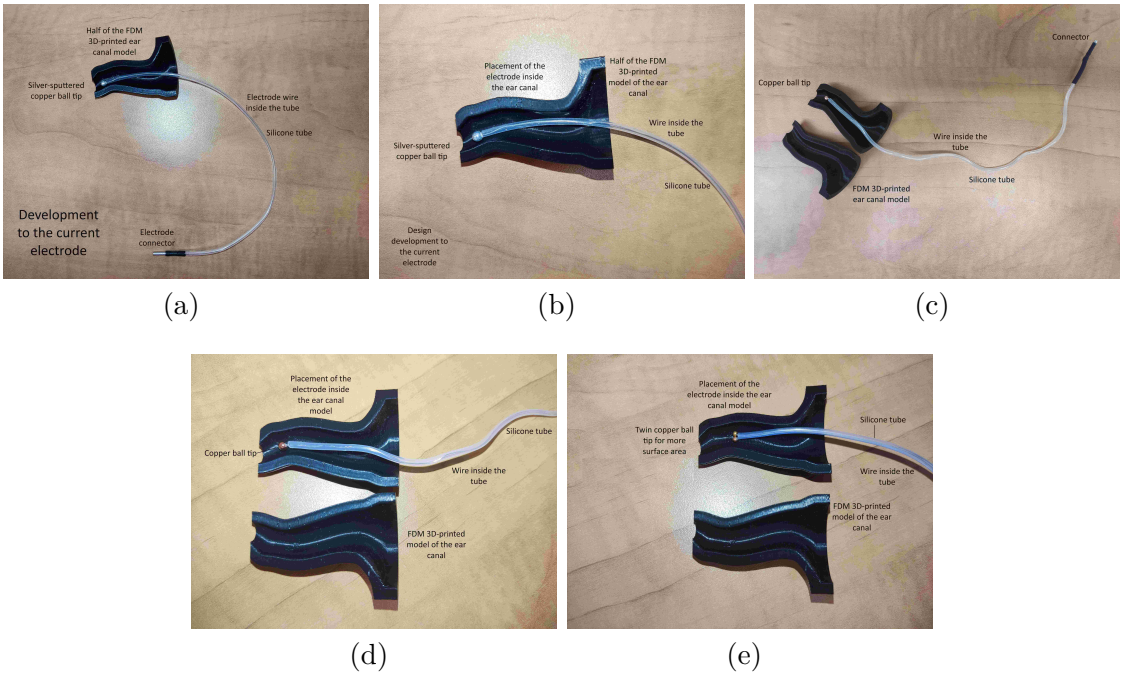

Figure 4.13: Development to the tip of the unactuated silicone-tube wire electrode (copper/silver ball tip) and its placement inside the FDM 3D-printed approximate ear canal model.

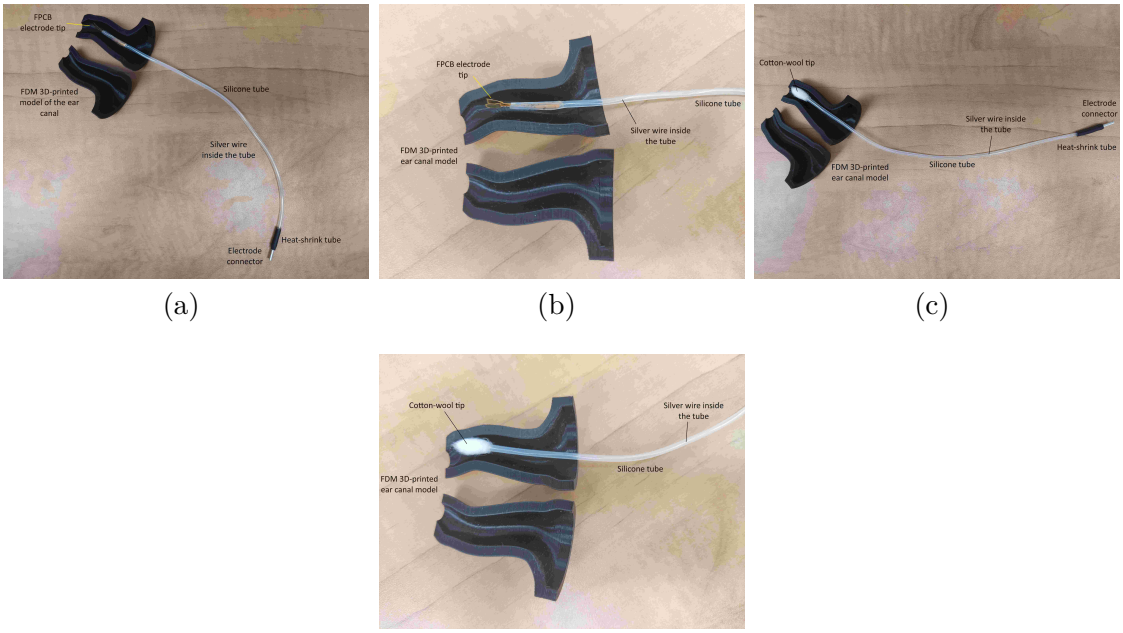

(a) (b) (c)

(d)

Figure 4.14: (a) and (b) Development to the tip of the unactuated silicone-tube wire electrode (double-sided FPCB tip) and it placement inside the FDM 3D-printed approximate ear canal model. (c) and (d) Placement of the unactuated silicone-tube wire cotton-wool electrode inside the FDM 3D-printed approximate ear canal model. It is voluminous due to not being gel-smeared.

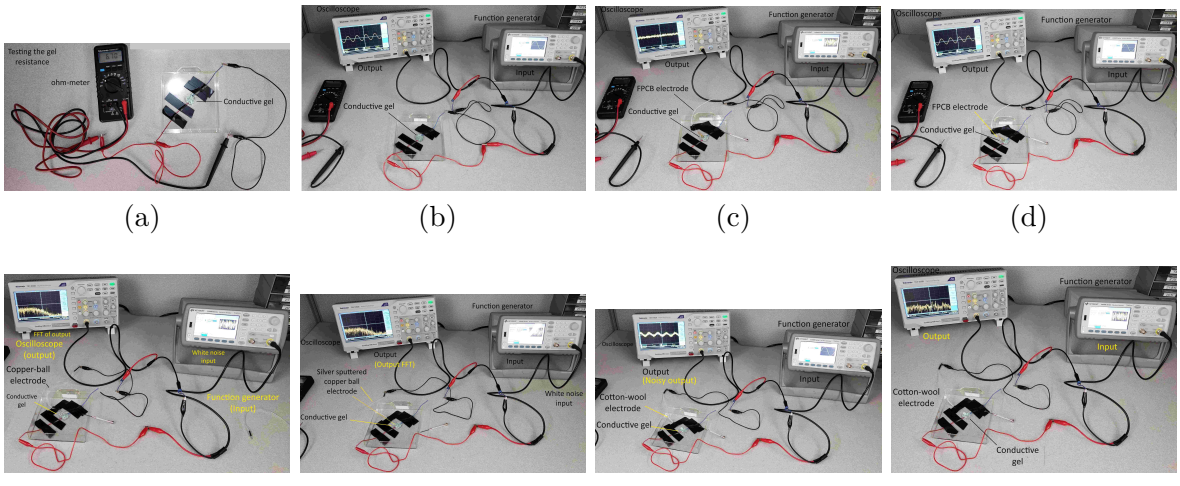

(a) (b) (c) (d)

(e) (f) (g) (h)

Figure 4.15: (a): Resistance of the electrolyte gel. (b): Input-output signal of the gel. (c) to (d): Input-output signal for the FPCB electrode. (e) to (f): Input-output signal for the copper and silver ball electrodes. (g) to (h): Input-output signal for the cotton-wool electrode.

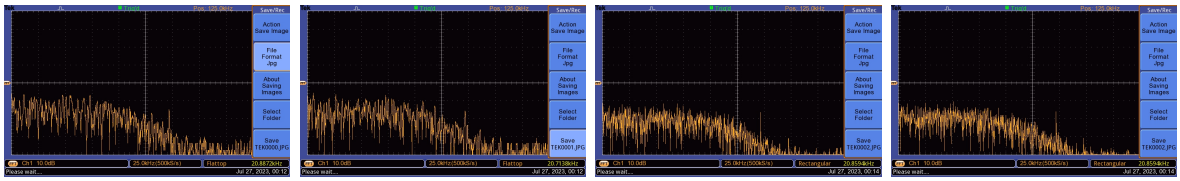

(a) (b) (c) (d)

Figure 4.16: Frequency response of the FPCB electrode.

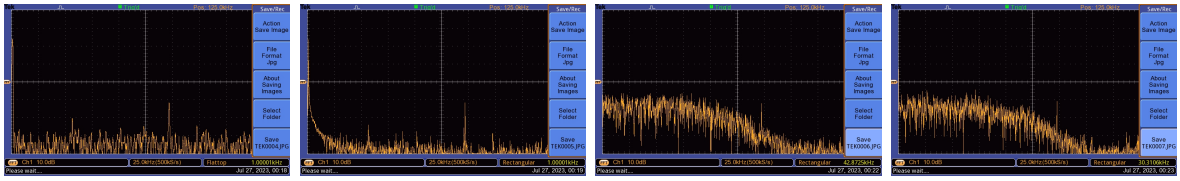

(a) (b) (c) (d)

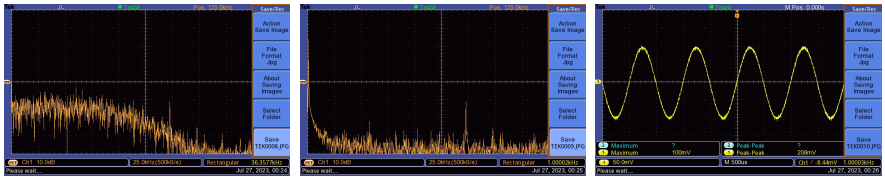

(e) (f) (g)

Figure 4.17: Frequency response of the ball electrodes: (a) to (c) copper ball electrode, (d) to (g) silver ball electrode. The output sinusoidal waveform is not noisy nor attenuated.

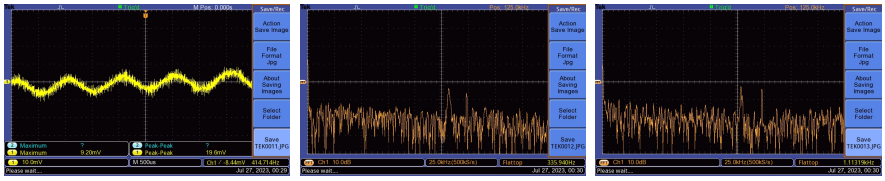

(a) (b) (c)

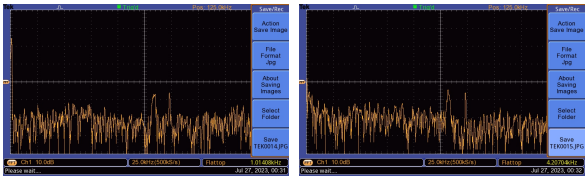

(d) (e)

Figure 4.18: Frequency response of the cotton-wool electrode. The output sinusoidal waveform is noisy and attenuated.

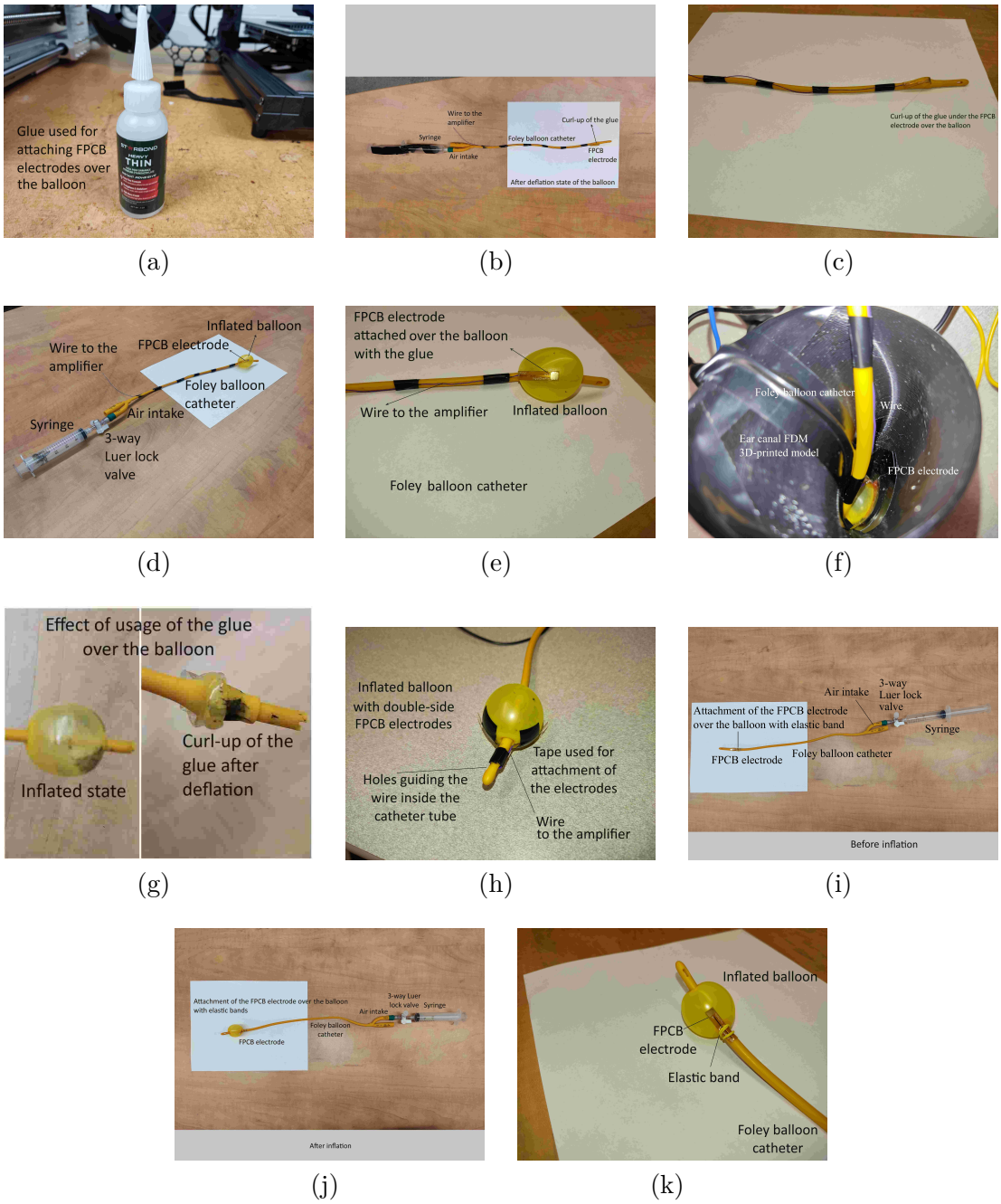

Figure 4.19: (a) Glue used for sticking the FPCB electrode over the balloon. (b) Assembly of the FPCB electrode over the balloon using the glue. (c) to (e): Problem of the glue curl-up. (f): Testing the FPCB electrode inside the approximate ear canal model. (g) Balloon deformation due to usage of different kinds of glue. (h) Sticking the FPCB over the balloon using tape. (i), (j), and (k) Sticking the FPCB electrode over the balloon using elastic band (or ligature).

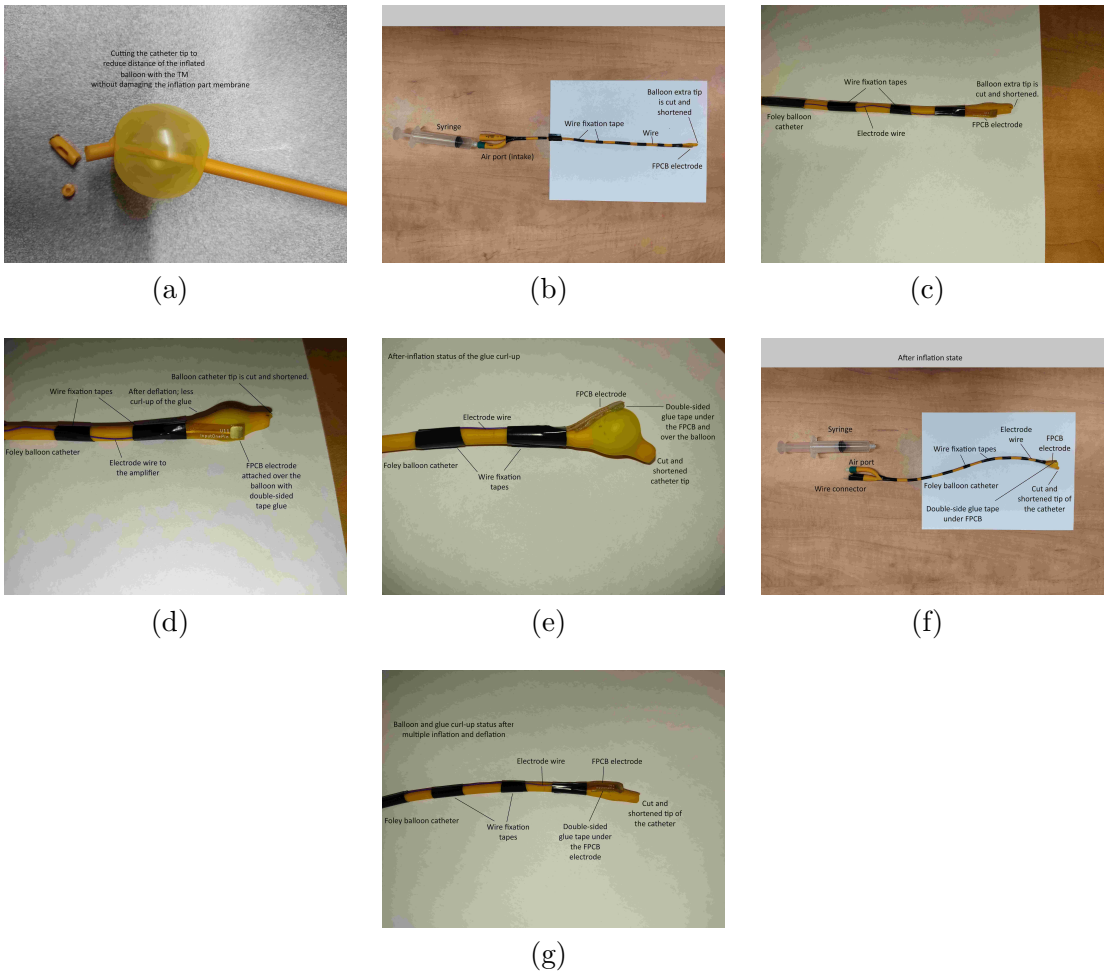

(a) (b) (c)

(d) (e) (f)

(g)

Figure 4.20: (a) Cutting the balloon catheter tip. (b) to (f) Using double-sided glue tape for assembly of the FPCB electrode over the balloon and its status while inflated and deflated. (g) Balloon status after multiple inflation and deflation, using double-sided glue tape.

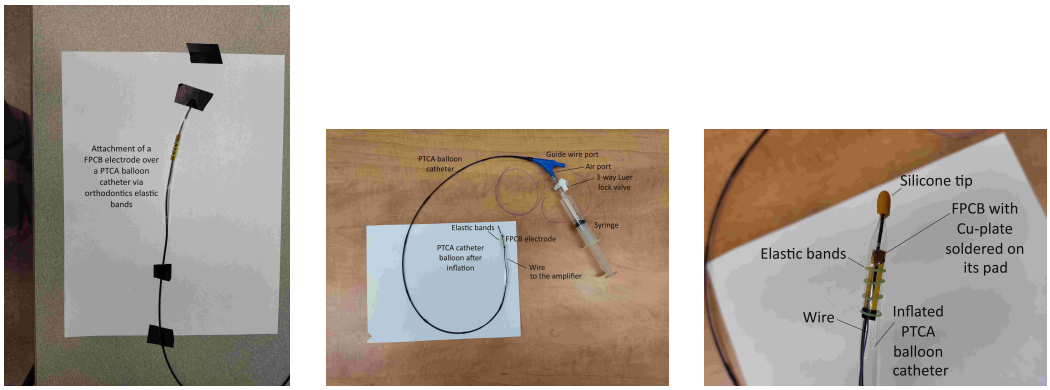

(a) (b) (c)

Figure 4.21: Assembly of the FPCB electrode over a PTCA balloon catheter.

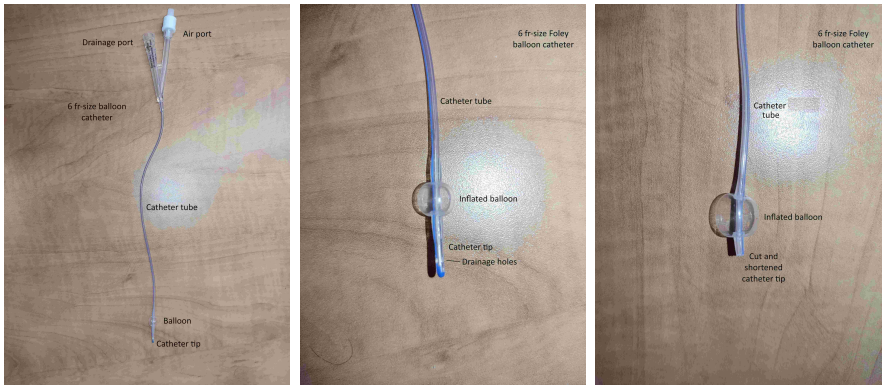

(a) (b) (c)

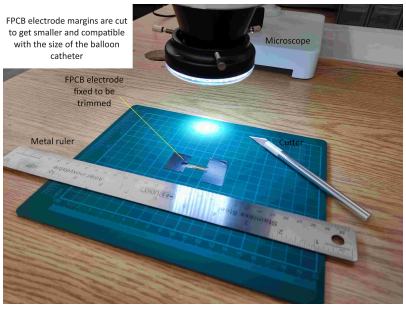

(d)

Figure 4.22: (a) to (d) Assembly of the FPCB electrode over a 6 fr-size balloon catheter. The catheter tip should be cut very carefully not to damage the inflated balloon. FPCB trimming and cutting of the catheter tip are suggested to be done under microscope.

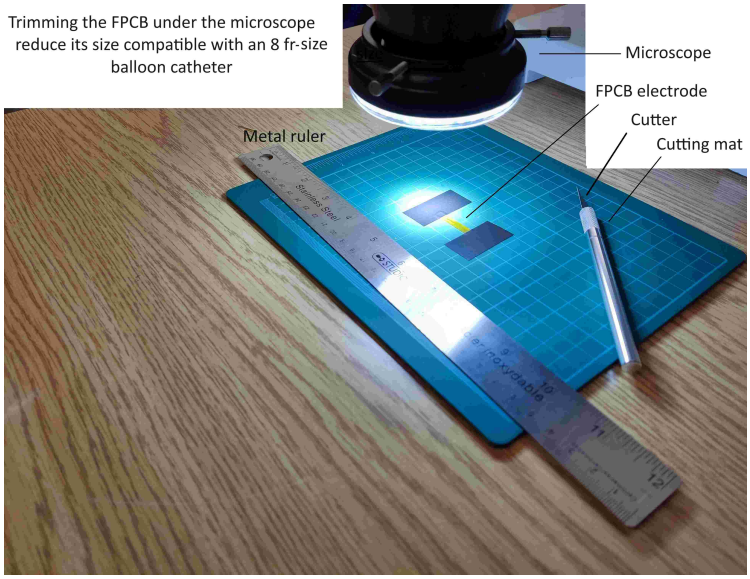

Figure 4.23: Cutting the FPCB under the microscope to trim the size for passive and especially active electrodes.

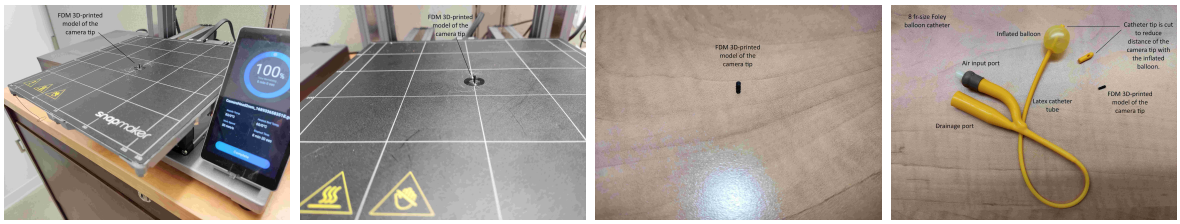

(a) (b) (c) (d)

(e) (f) (g)

Figure 4.24: (a) to (c) 3D-printing a camera head to check if it will be accommodated inside the catheter tube. (d) to (g) Putting the 3D-printed camera head model inside the catheter tube. The actual camera, which is suggested for being put inside the catheter tube, can be OVM6948 image sensor. The cross sectional size of its cubic structure is 0.65 mm by 0.65 mm which can be accomodated by the catheter tube.

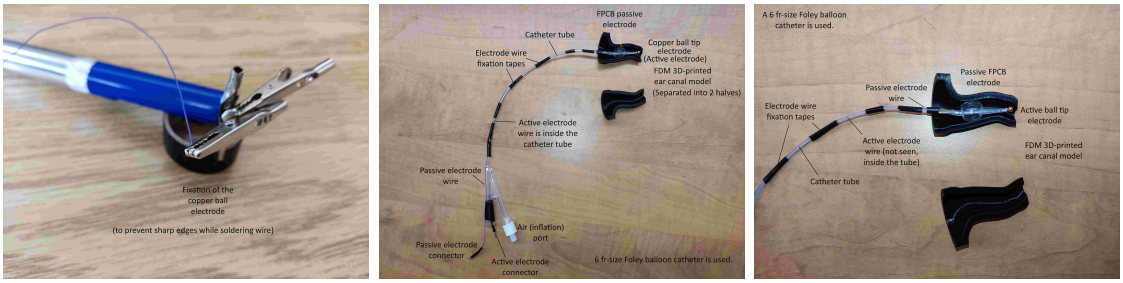

(a) (b) (c)

Figure 4.25: Fabrication of the electrode using a 6 fr-size silicone Foley balloon catheter with a round ball active electrode at the tip and an FPCB electrode as the passive electrode touching the canal.

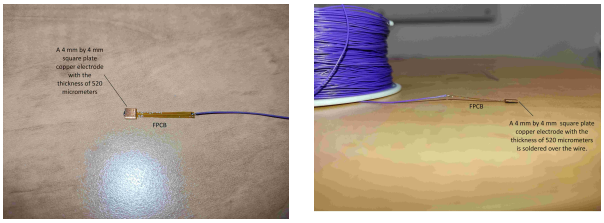

(a) (b)

Figure 4.26: Assembly of the copper-plate (Cu-disc) electrode over the FPCB electrode to increase the electrode height.

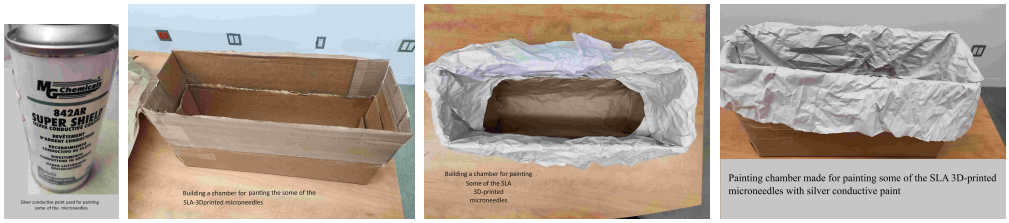

(a) (b) (c) (d)

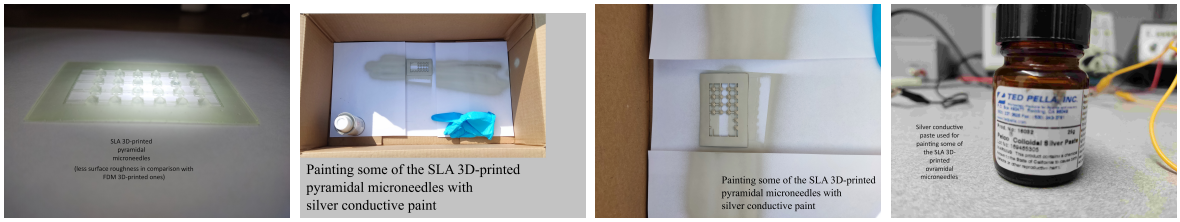

(e) (f) (g) (h)

Figure 4.27: Painting plastic SLA-3D-printed micro-needles: (a) Silver conductive paint used, (b) to (d) Building a painting chamber, (e) SLA 3D-printed micro-needles, (f) and (g) Painted micro-needles inside the chamber. (h) Silver paste not used for our painting.



(a) (b) (c)

(d) (e)

Figure 4.28: (a) SLA-3D-printed micro-needles with smaller size; (b) and (e) with a base of 4 mm by 4 mm, (c) and (d) with a base of 2 mm by 2 mm.

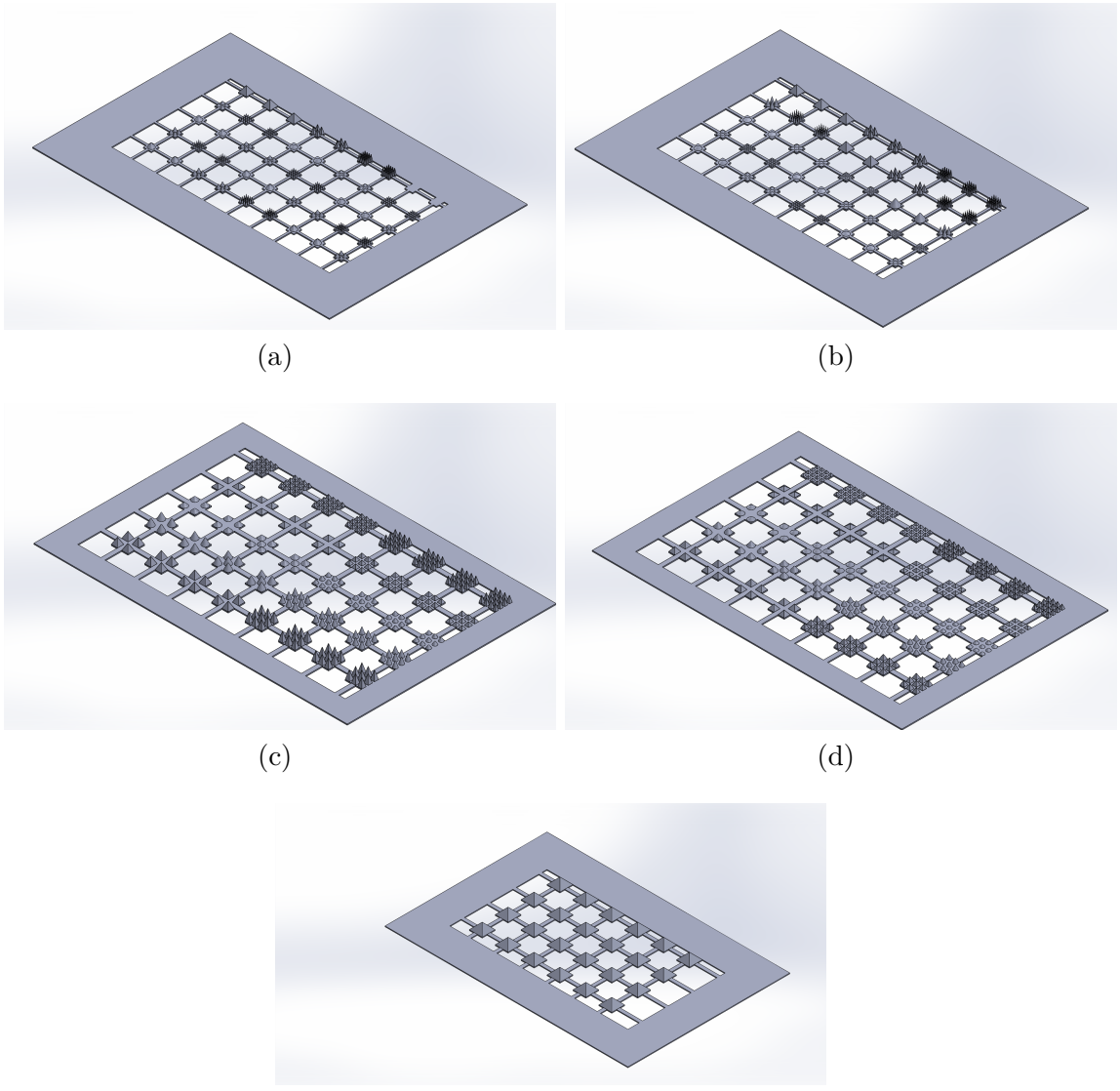

Figure 4.29: Digram of SLA-3D-printed micro-needles with smaller size; (a) and (b) with a square base of 2 mm by 2 mm. The height changes from 0.1 to 1 mm with an step of 0.1 mm. There are some other taller microneedles just for later testing of 3D-print quality. (c) and (d) with a square base of 4 mm by 4 mm. The height of microneedles are 0.5, 0.75, 1, 1.5, and 2 mm. (e) Pyramidal structure with the height of 2 mm on a square base of 2 mm by 2 mm.

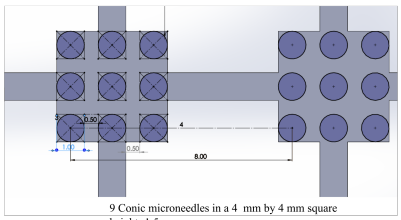

9 Conic microneedles in a 4 mm by 4 mm square
height=1.5 mm
radius=0.5 mm

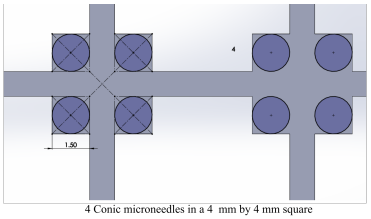

4 Conic microneedles in a 4 mm by 4 mm square
height=1.5 mm
radius=0.75 mm

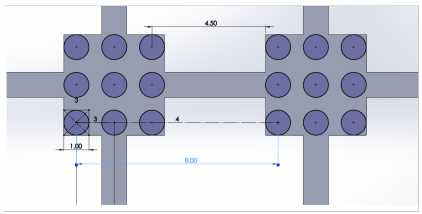

9 Conic microneedles in a 4 mm by 4 mm square
height=0.75 mm
radius=0.5 mm

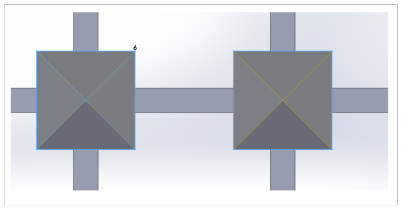

1 Pyramidal microneedles in a 4 mm by 4 mm square
height=2 mm
sqaure side=4 mm

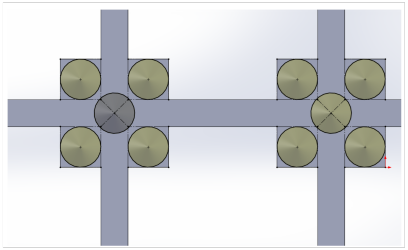

1 Conic microneedles in a 4 mm by 4 mm square in the center is obtained by removing (cutting) 4 other corner microneedles.
height=1.5 mm
radius=0.75 mm

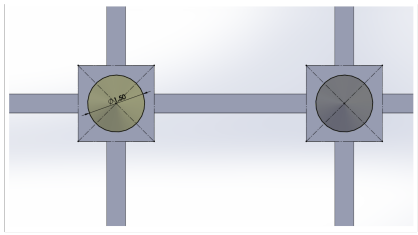

1 Conic microneedle in a 2 mm by 2 mm square
height=0.9 mm
radius=0.75 mm

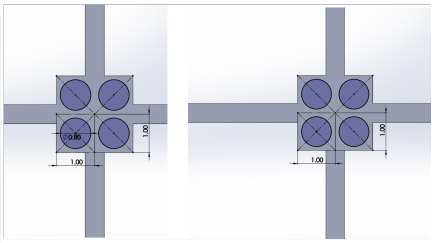

4 Conic microneedles in a 2 mm by 2 mm square
height=1.5 mm
radius=0.4 mm

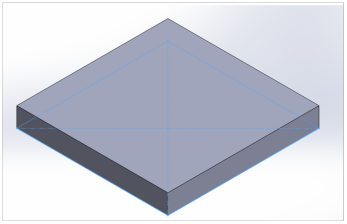

Copper plate (disc) in a 4 mm by 4 mm square
height=0.52 mm
square side=4 mm

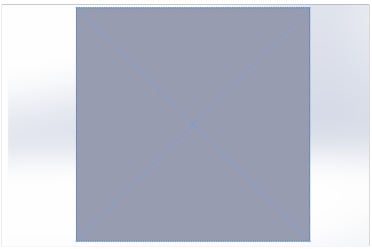

FPCB in a 4 mm by 4 mm square
height is almost zero.
sqaure side=4 mm

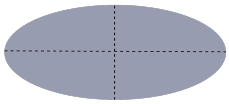

Approximate shape of the cotton-wool tip in the experiment when pressed and smooth
big diameter = 5 to 7 mm
small diameter = 2 t o 3 mm

Figure 4.30: Diagrams of the microneedles and other electrodes used in the experiments discussed in the next chapter.

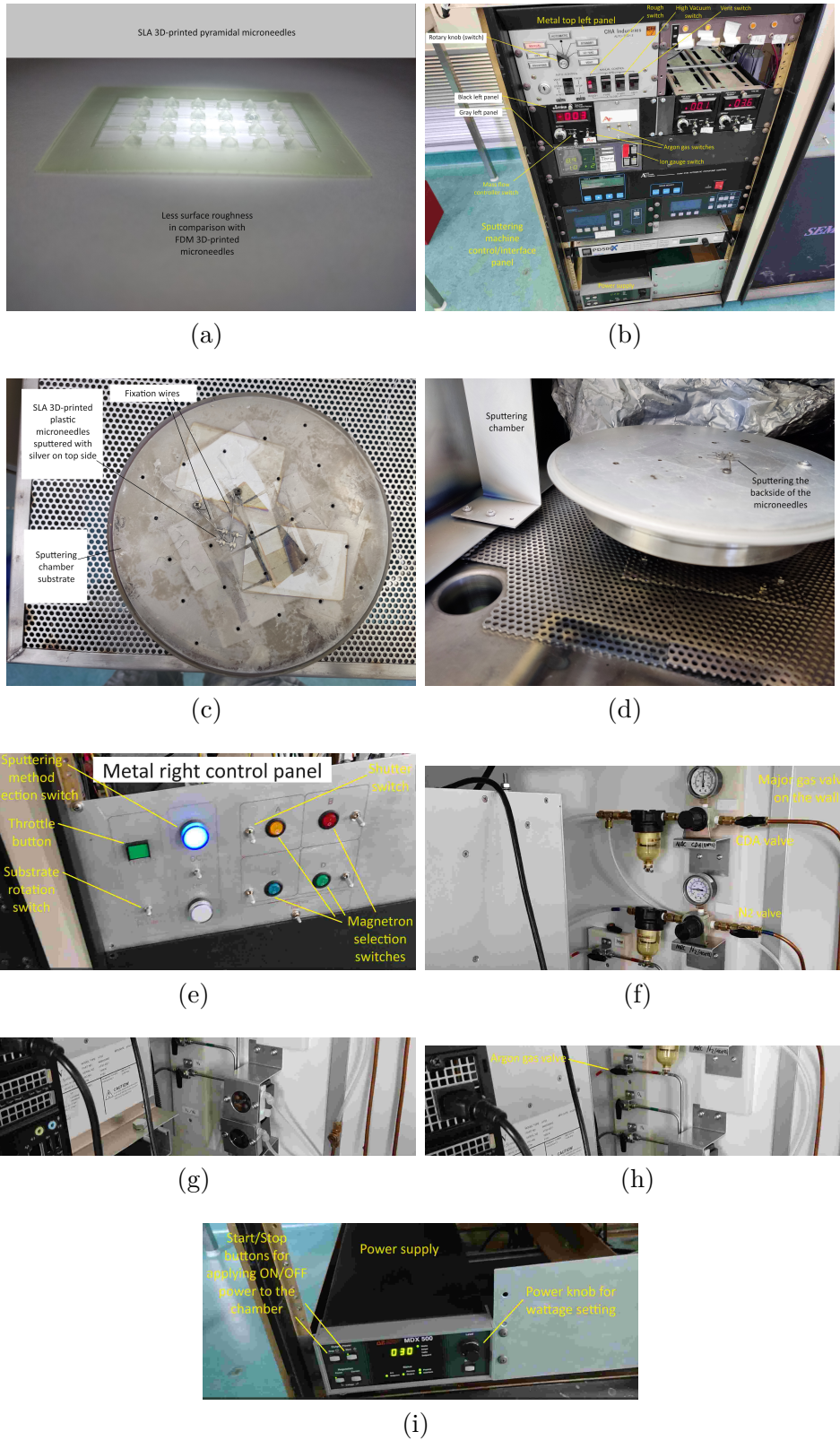

Figure 4.31: Silver-sputtering of the plastic SLA-3D-printed pyramidal micro-needles.

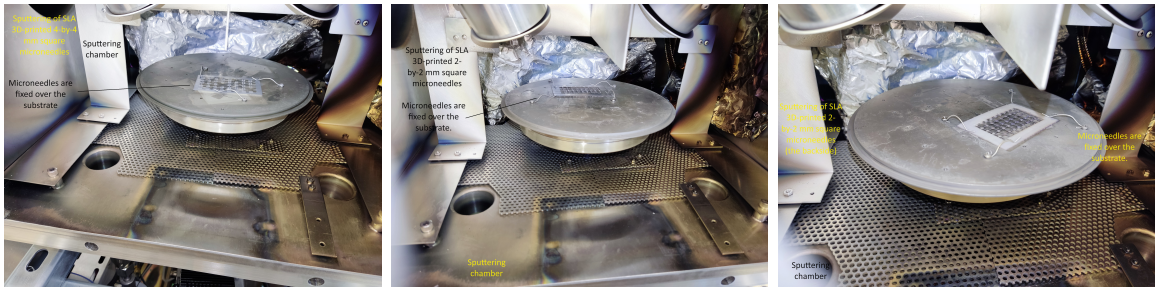

(a) (b) (c)

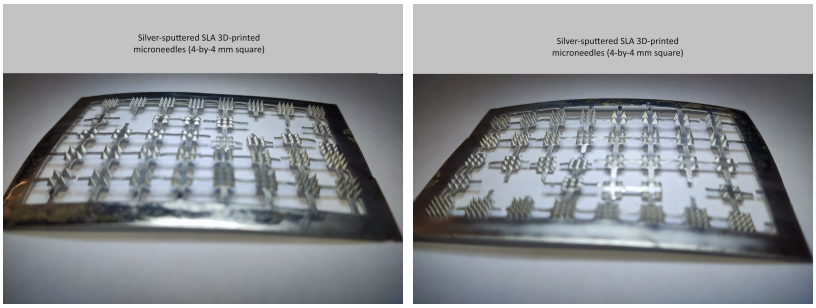

(d) (e)

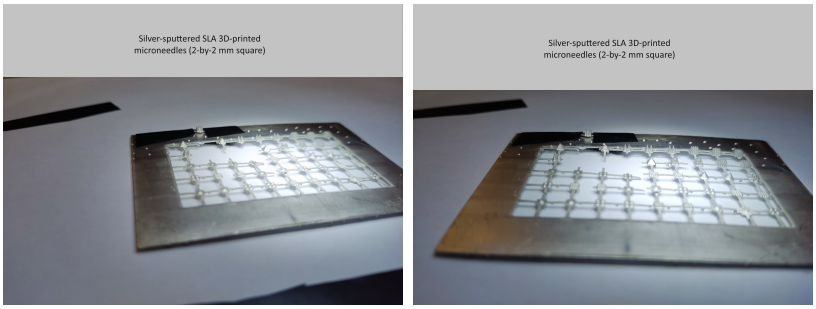

(f) (g)



(h) (i)

Figure 4.32: Silver-sputtering of the plastic SLA-3D-printed conic and pyramidal microneedles. (a) to (c) Micro-needles inside the sputtering chamber, (d) to (i) 4 mm and 2 mm square micro-needles after sputtering.

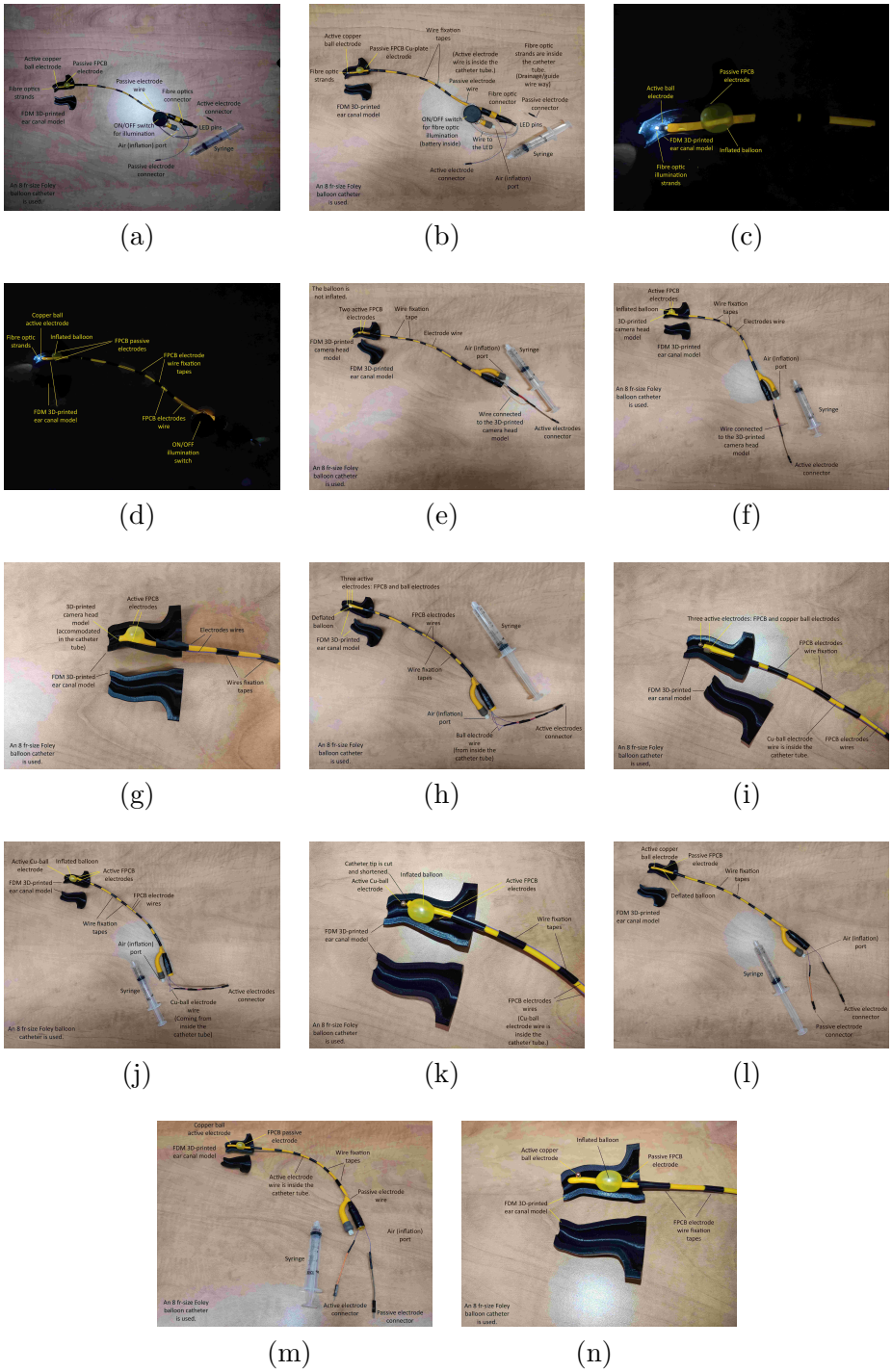

Figure 4.33: 8 fr-size latex Foley balloon catheters equipped with different types of electrodes: (a) to (d): Using fibre optic strands, ball tip and FPCB electrodes. (e) to (g): Electrode with double FPCB and a camera-like head inside the tube. (h) to (k): Electrode with double side FPCB and ball tip. (l) to (n): Using ball tip and FPCB electrodes as active and passive electrodes.

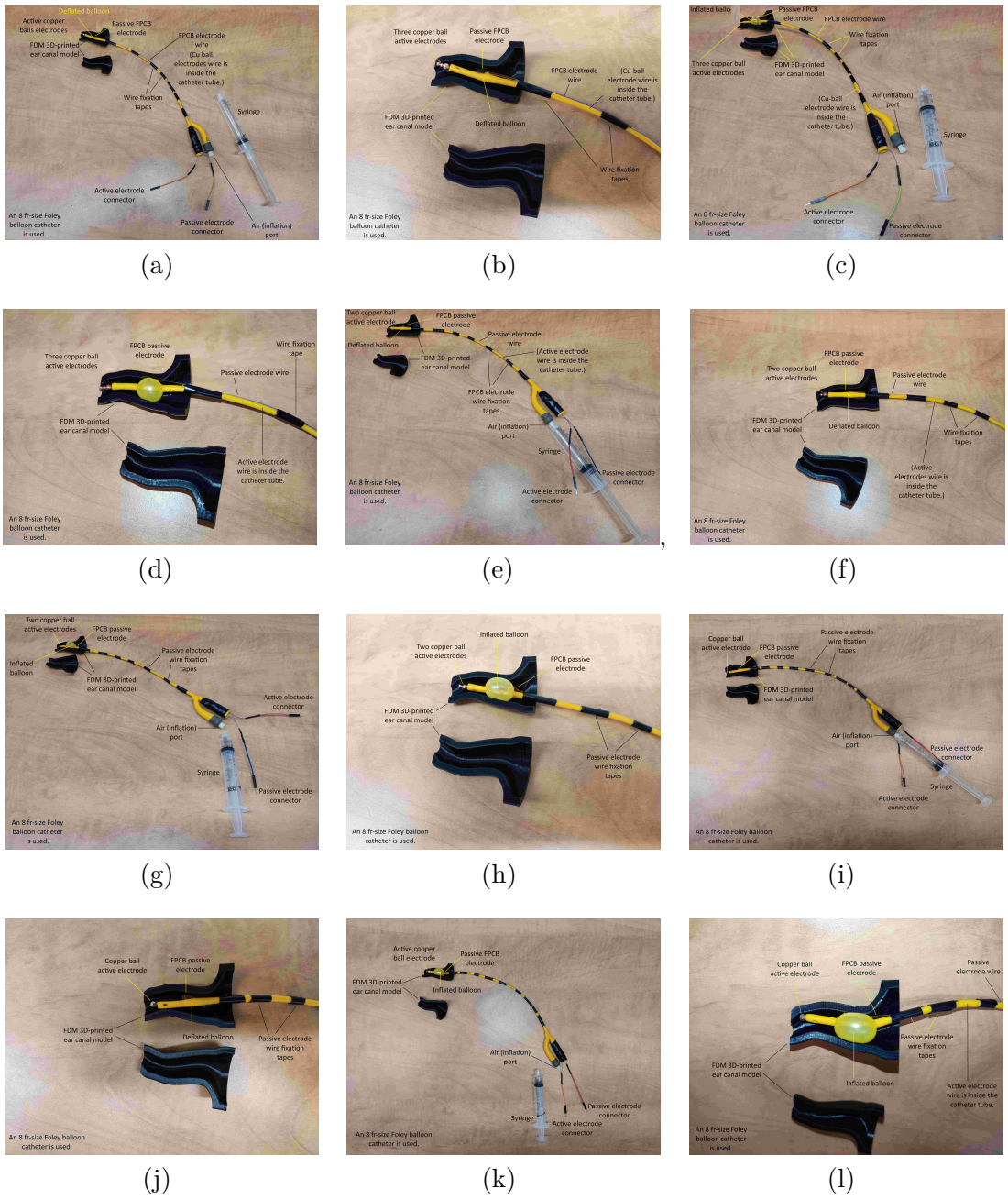

(a) (b) (c)

(d) (e) (f)

(g) (h) (i)

(j) (k) (l)

Figure 4.34: 8 fr-size latex Foley balloon catheters equipped with different types of electrodes and various configurations: (a) to (d): Using three ball tips and FPCB electrode as active and passive electrodes. (e) to (h): Using two ball tips and FPCB electrode as active and passive electrodes. (i) to (l): Using single ball tip and FPCB electrode as active and passive electrodes.

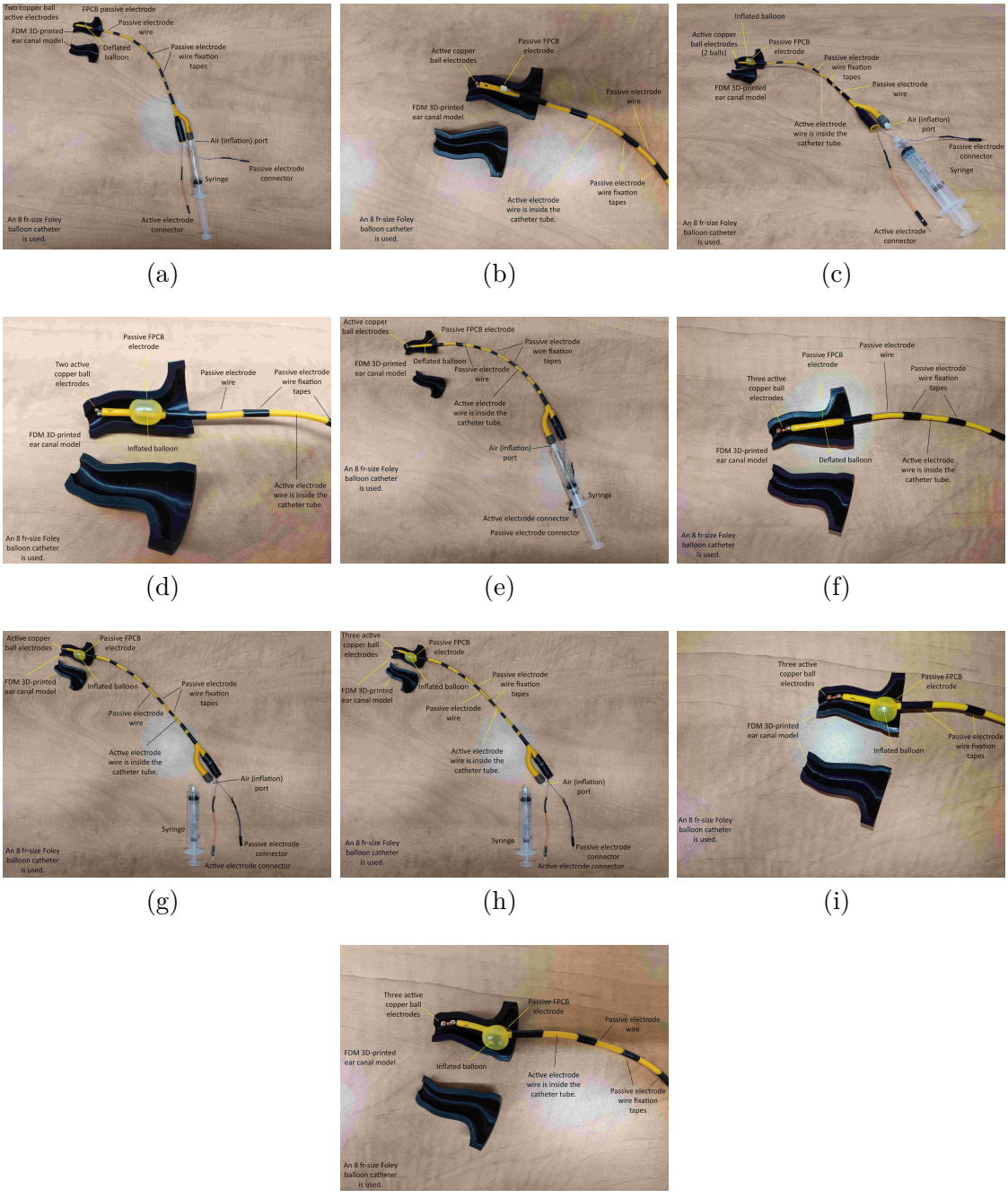

Figure 4.35: 8 fr-size latex Foley balloon catheters equipped with different types of electrodes and various configurations: (a) to (d): Using two ball tips and FPCB electrode as active and passive electrodes. (e) to (j): Using three ball tips and FPCB electrode as active and passive electrodes.

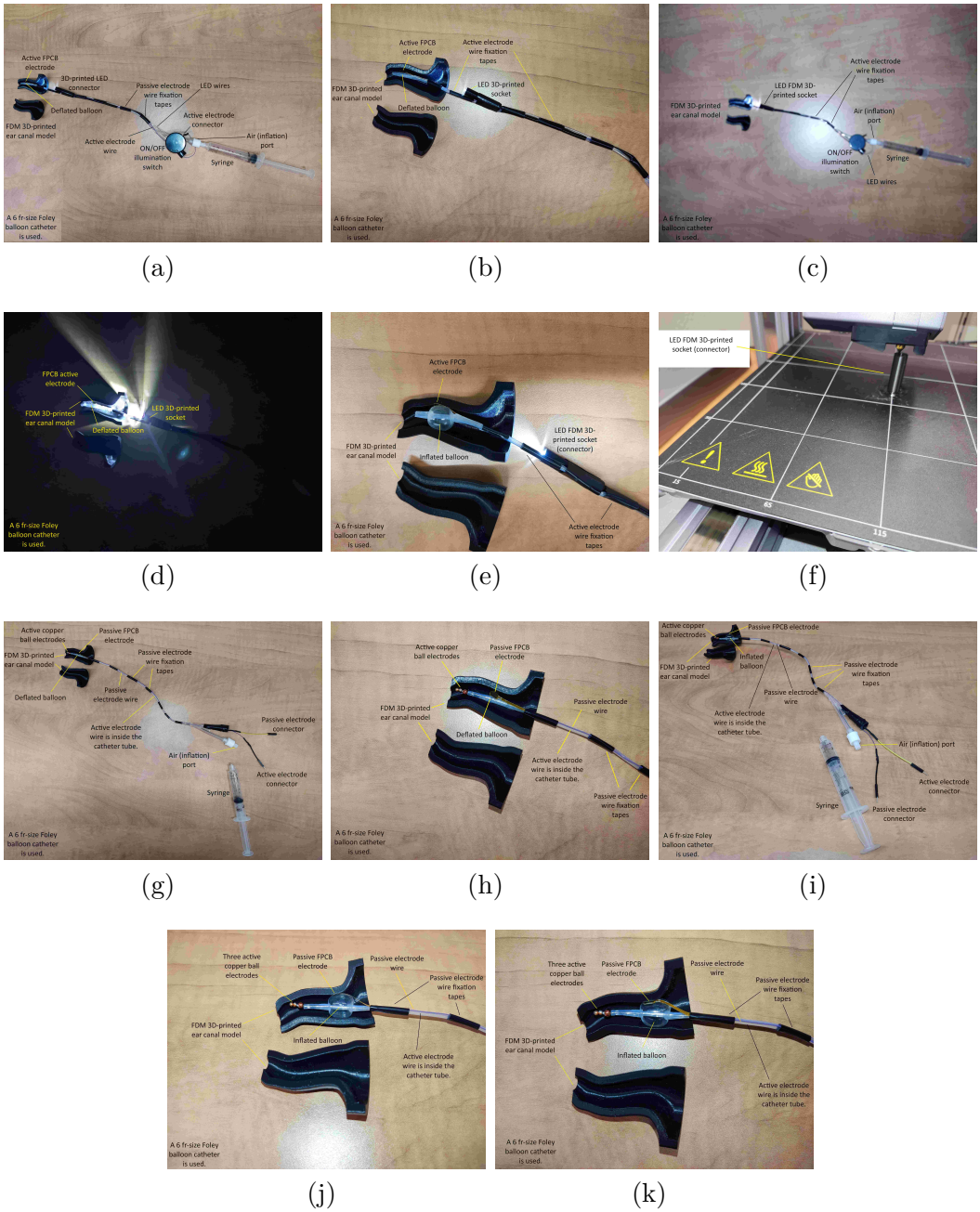

(a) (b) (c)

(d) (e) (f)

(g) (h) (i)

(j) (k)

Figure 4.36: 6 fr-size silicone Foley balloon catheters equipped with different types of electrodes and various configurations: (a) to (e): Using one single FPCB electrode as active electrode. (f) 3D-printed LED chamber. (g) to (k): Using three ball tips and FPCB electrode as active and passive electrodes.

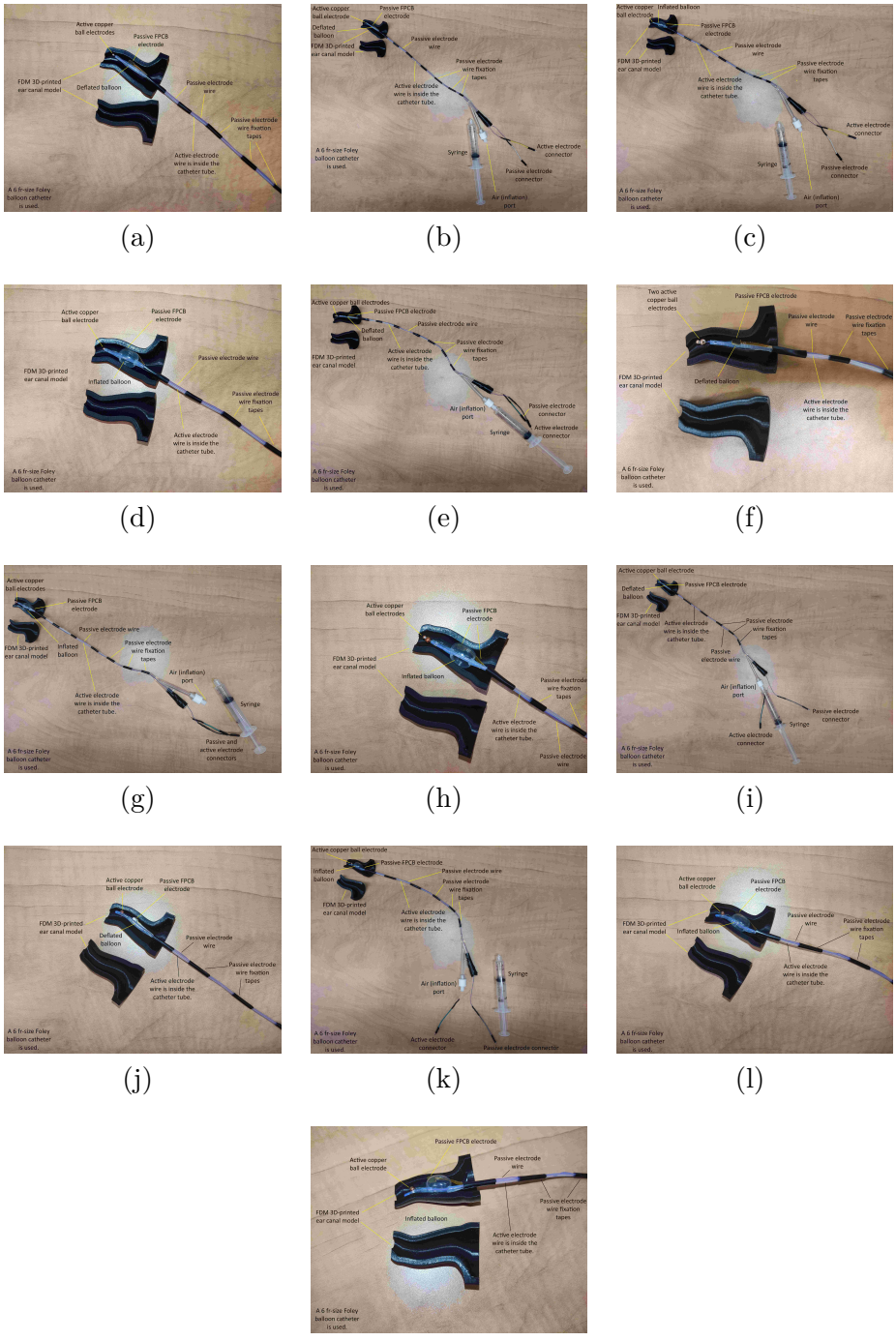

Figure 4.37: 6 fr-size silicone Foley balloon catheters equipped with different types of electrodes and various configurations: (a) to (d): Using one ball tip and FPCB electrode as active and passive electrodes. (e) to (h): Using two ball tips and FPCB electrode as active and passive electrodes. (i) to (m): Using one ball tip and FPCB electrode as active and passive electrodes.

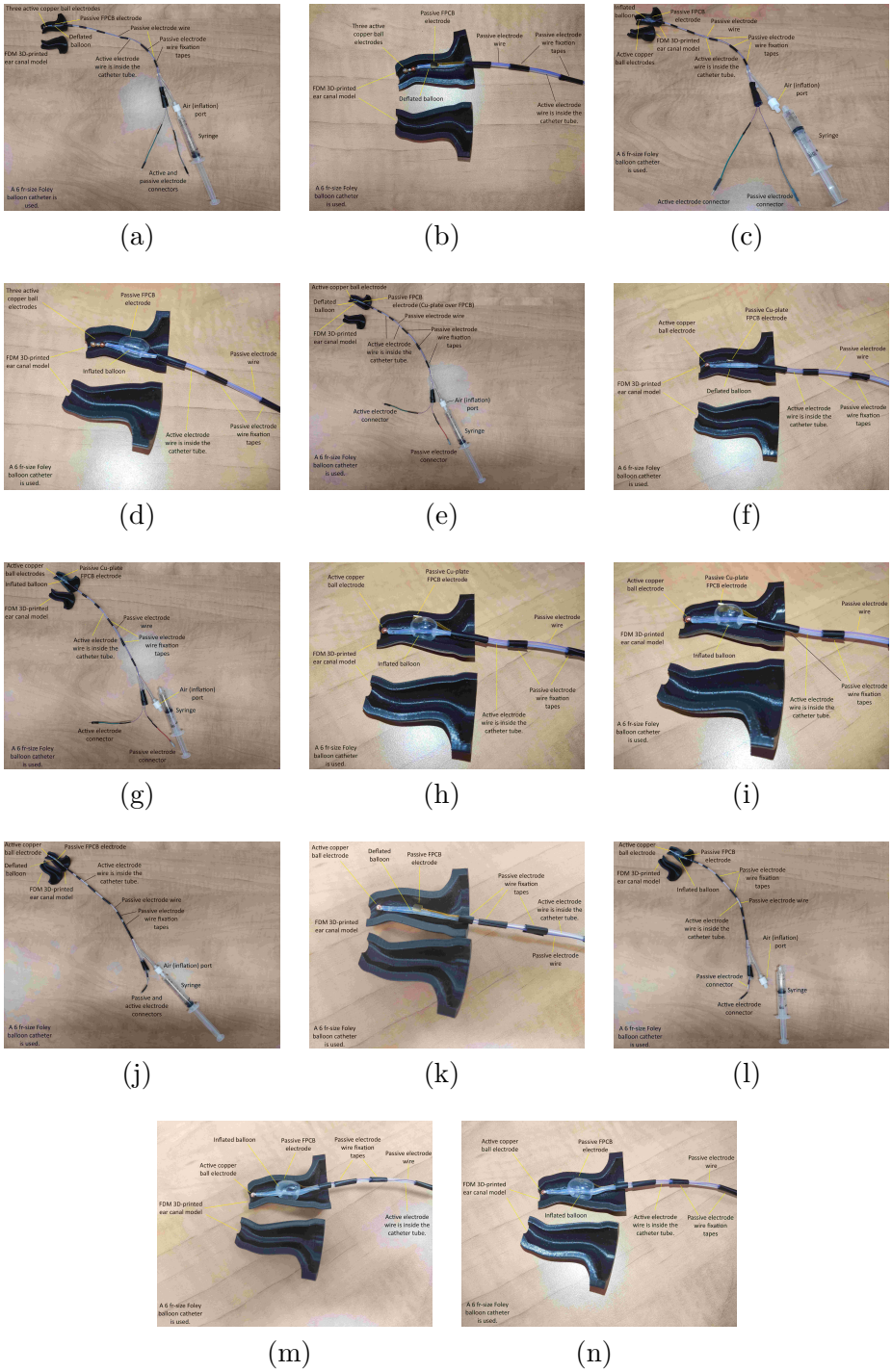

Figure 4.38: 6 fr-size silicone Foley balloon catheters equipped with different types of electrodes and various configurations: (a) to (d): Using three ball tips and FPCB electrode as active and passive electrodes. (e) to (i): Using one ball tip and FPCB-Cu-plate electrode as active and passive electrodes. (j) to (n): Using one ball tip and FPCB electrode as active and passive electrodes.

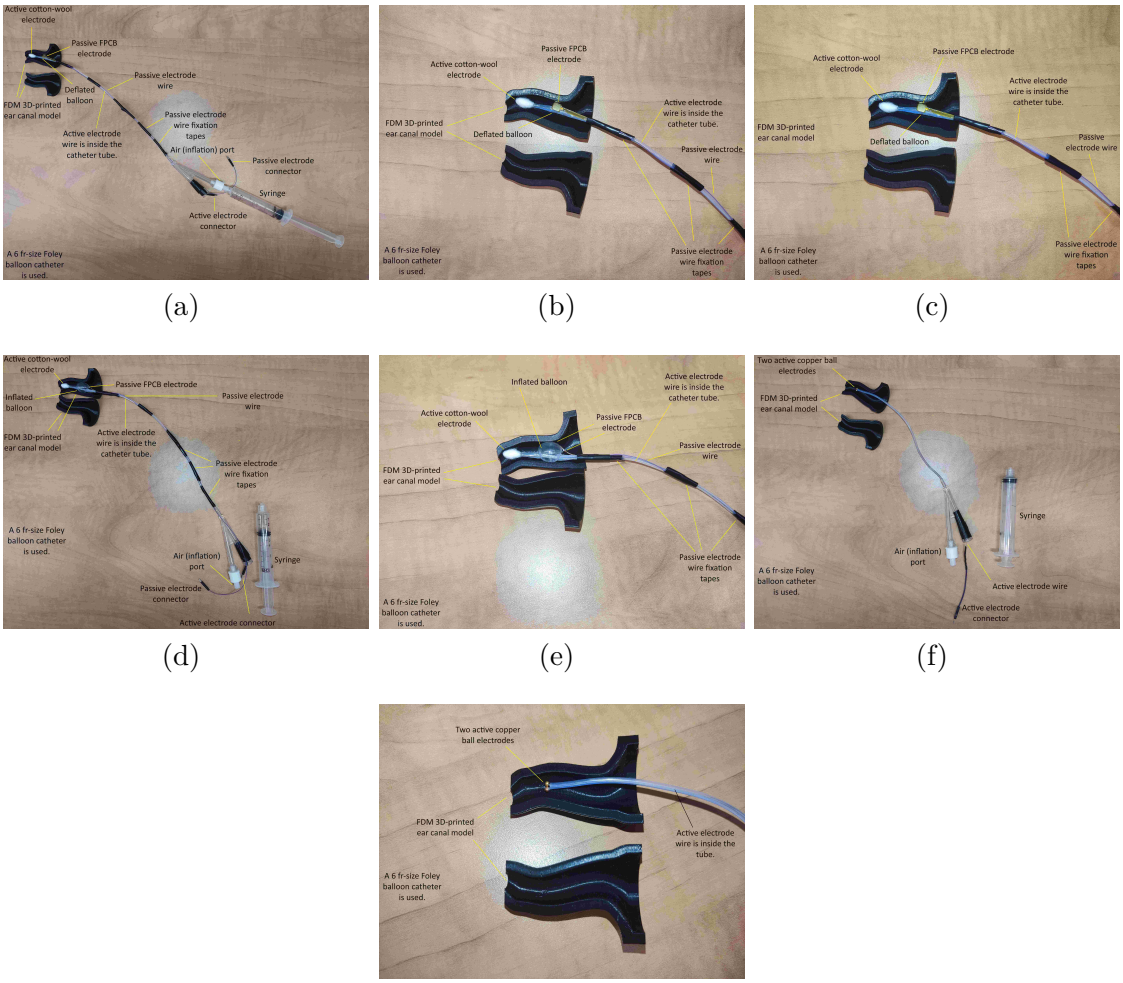

Figure 4.39: 6 fr-size silicone Foley balloon catheters equipped with different types of electrodes and various configurations: (a) to (e): Using cotton-wool tip and FPCB electrode as active and passive electrodes. (f) to (g): Using two ball tips as active electrode.

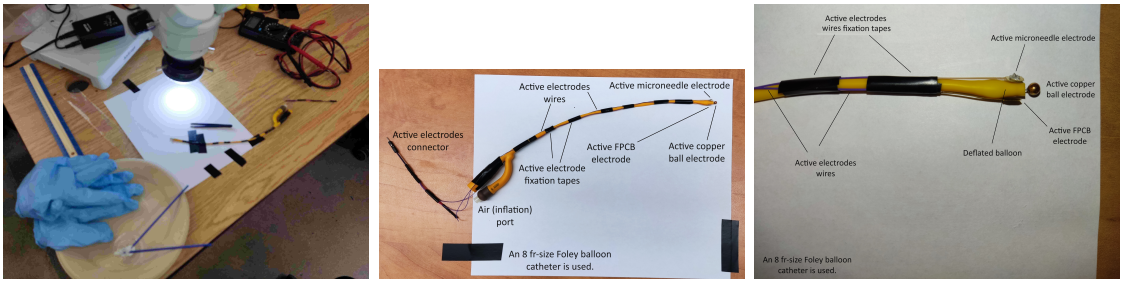

Figure 4.40: 8 fr-size latex Foley balloon catheter equipped with different types of electrodes: (a): Micro-needle attachment over the FPCB. (b) and (c): The Foley balloon catheter is equipped with three different kinds of active electrodes.

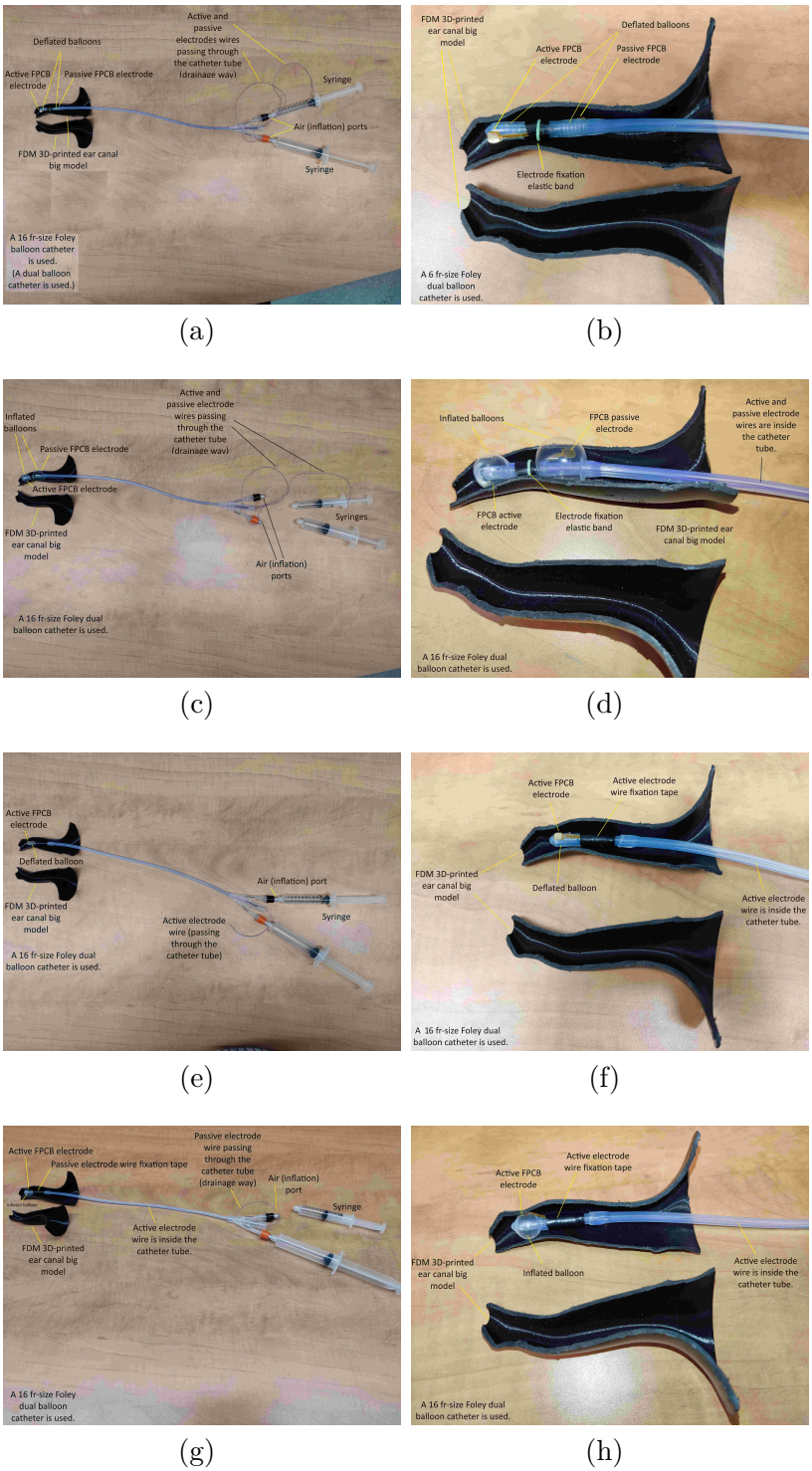

Figure 4.41: Dual-balloon two-way Foley catheter equipped with active and passive FPCB electrodes.

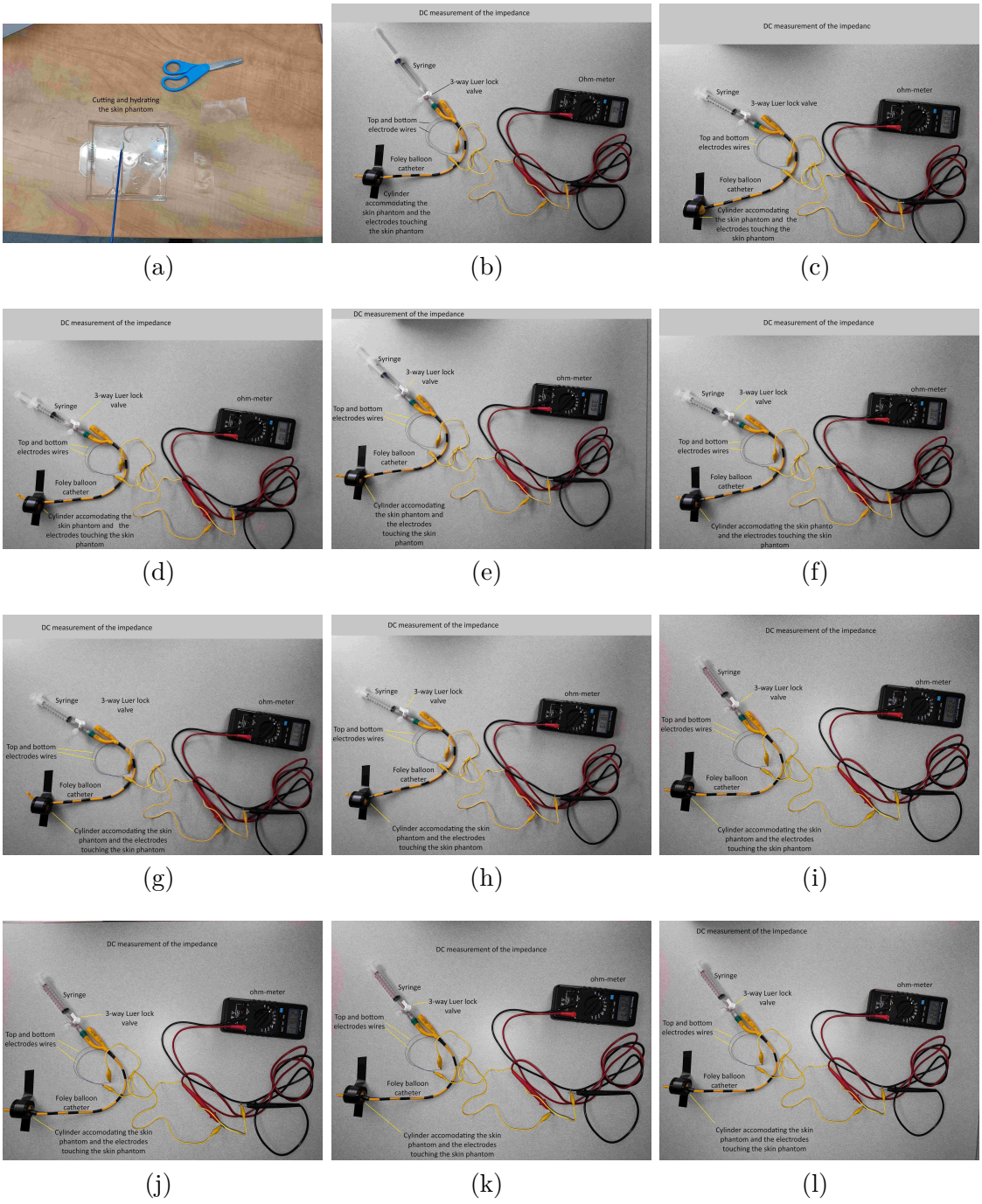

(a) (b) (c)

(d) (e) (f)

(g) (h) (i)

(j) (k) (l)

Figure 4.42: (a): Hydration of the skin phantom. (b) to (l): DC measurement (resistance measurement) of the FPCB electrode when the volume of the catheter balloon is increased. They are sequential read-outs at different times.

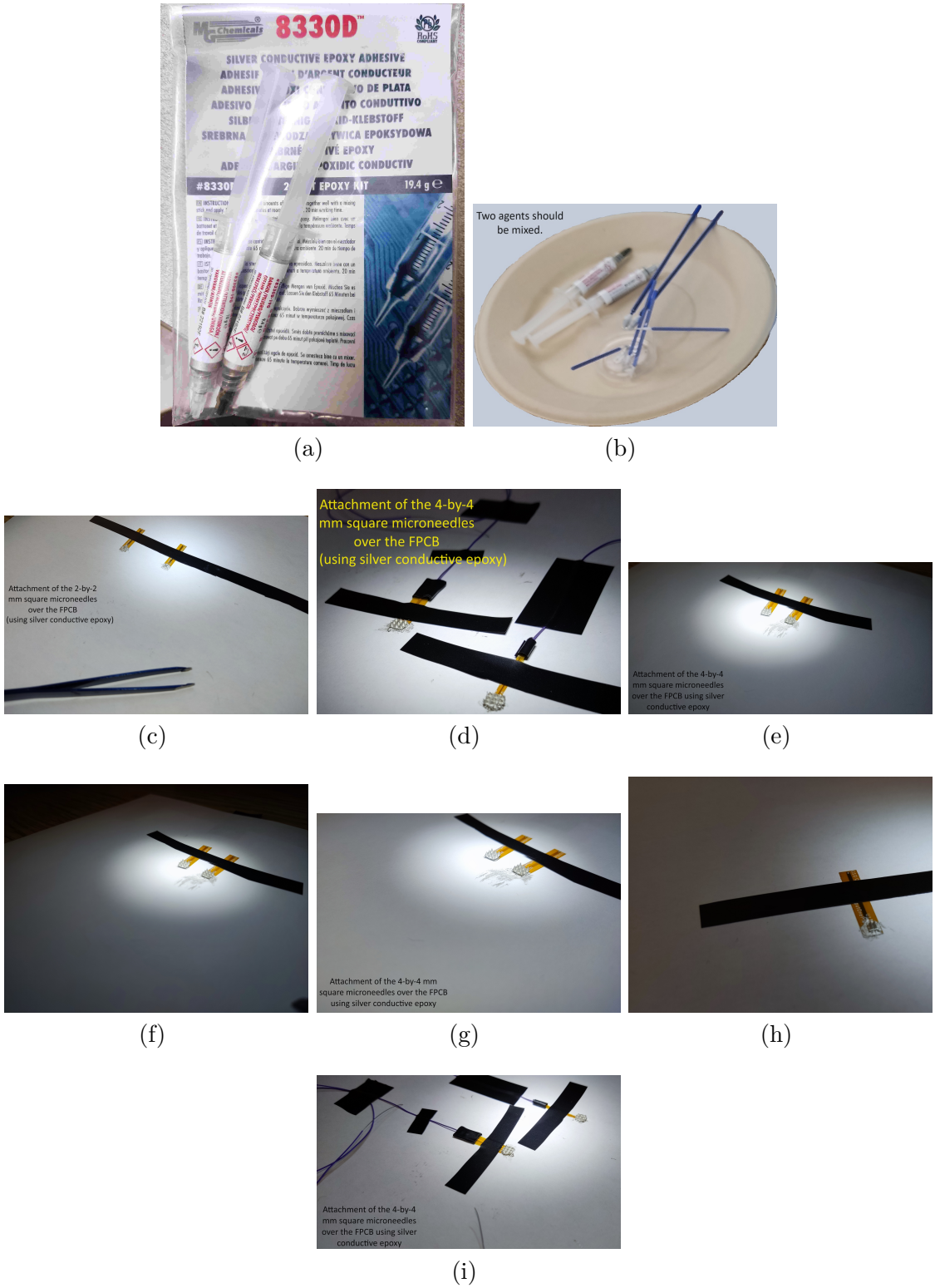

(a) (b)

(c) (d) (e)

(f) (g) (h)

(i)

Figure 4.43: (a) to (b) Using silver epoxy for attachment of micro-needles on FPCB. (c) to (i) Sample micro-needles attached via silver epoxy on FPCB electrodes.

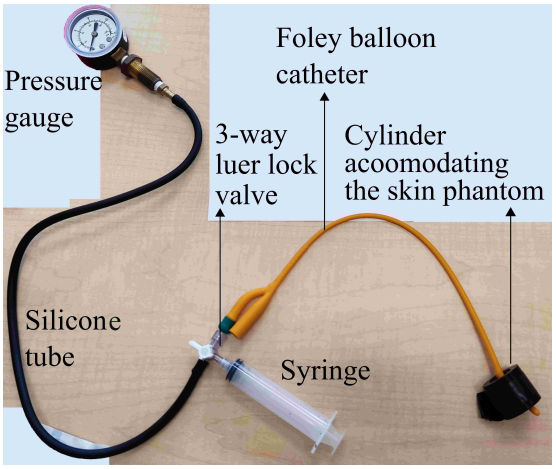

(a)

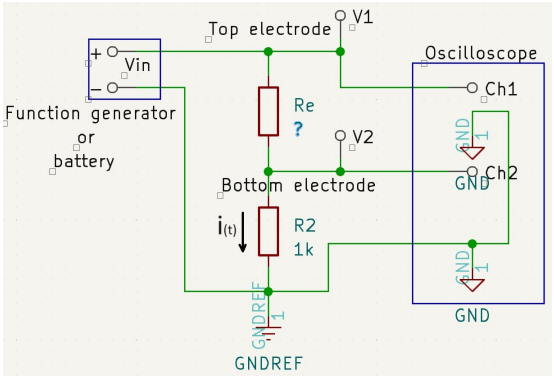

(b)

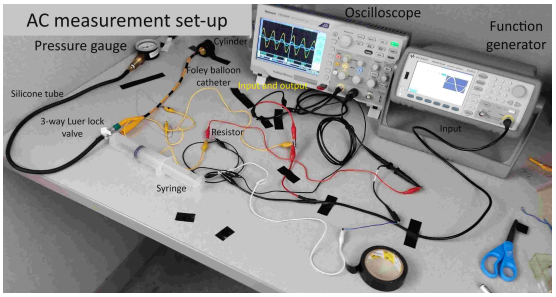

(c)

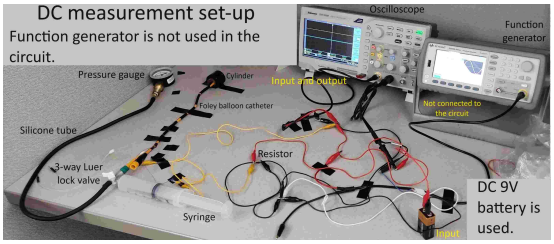

(d)

Figure 4.44: Main tools and experimental setup for measurement of impedance variation of the electrodes vs pressure change (both AC and DC measurements).

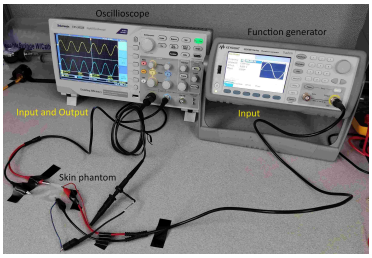

(a)

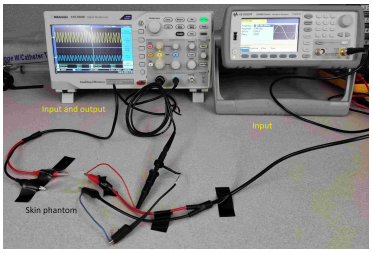

(b)

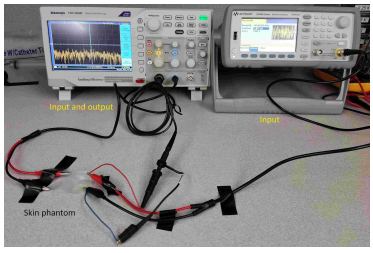

(c)

Figure 4.45: Checking the skin phantom frequency response.

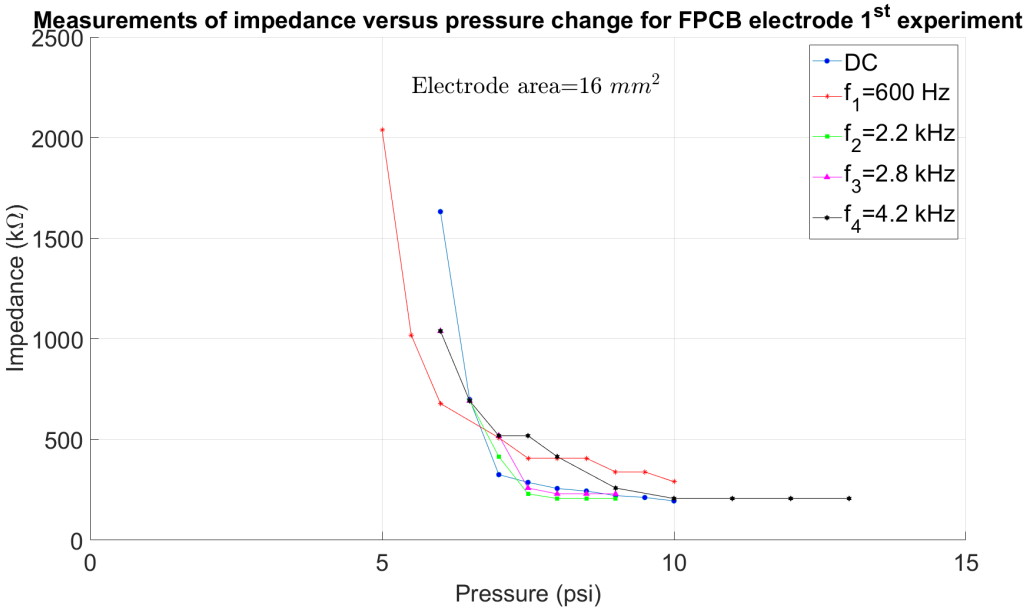

Figure 4.46: FPCB electrode impedance variation vs pressure change (thin structure with a sqaure base of 4 mm by 4 mm and a height of almost zero).

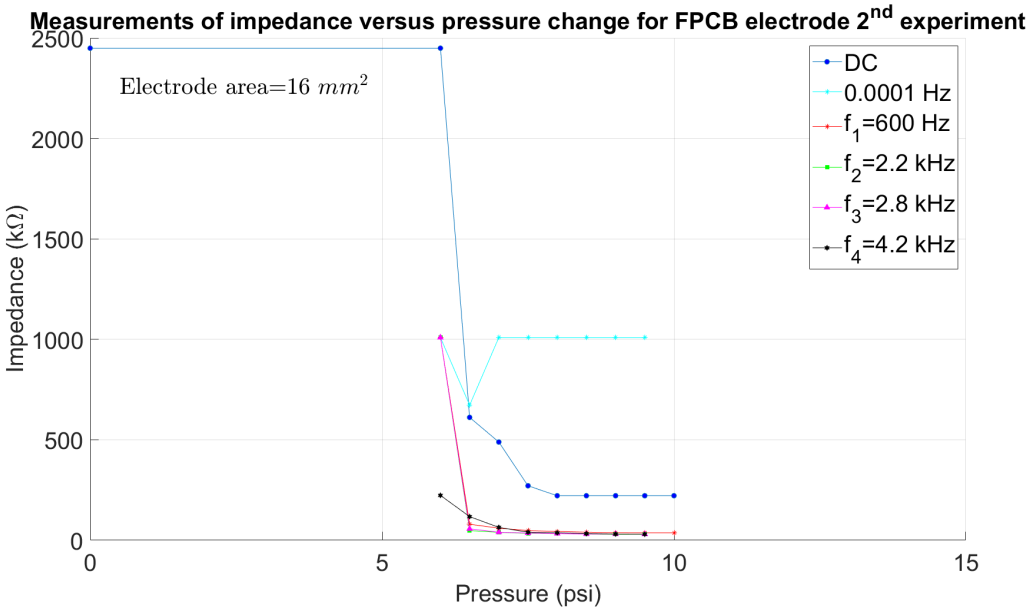

Figure 4.47: FPCB electrode impedance variation vs pressure change (thin structure with a sqaure base of 4 mm by 4 mm and a height of almost zero).

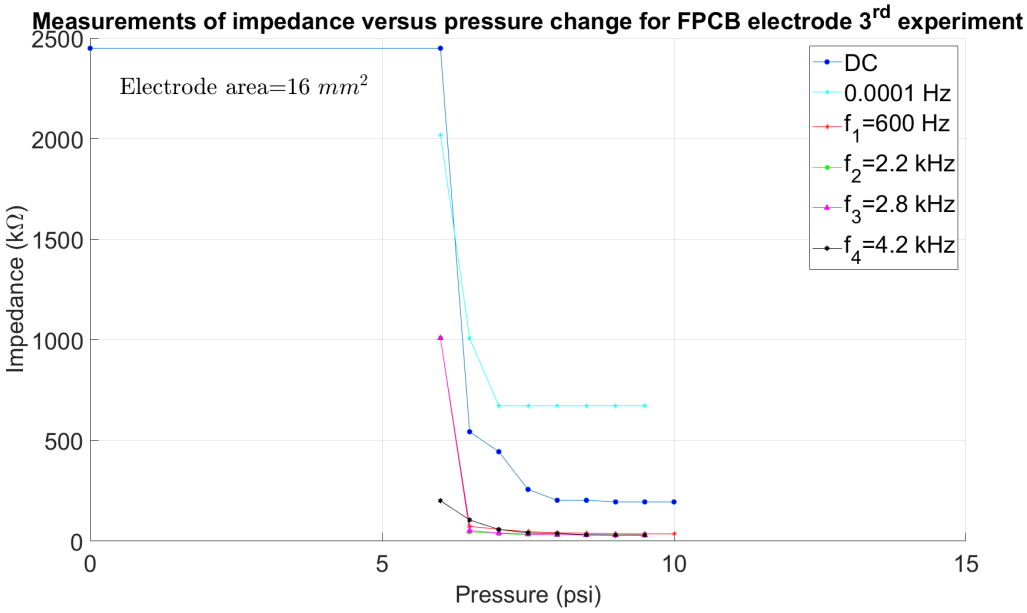

Figure 4.48: FPCB electrode impedance variation vs pressure change (thin structure with a sqaure base of 4 mm by 4 mm and a height of almost zero).

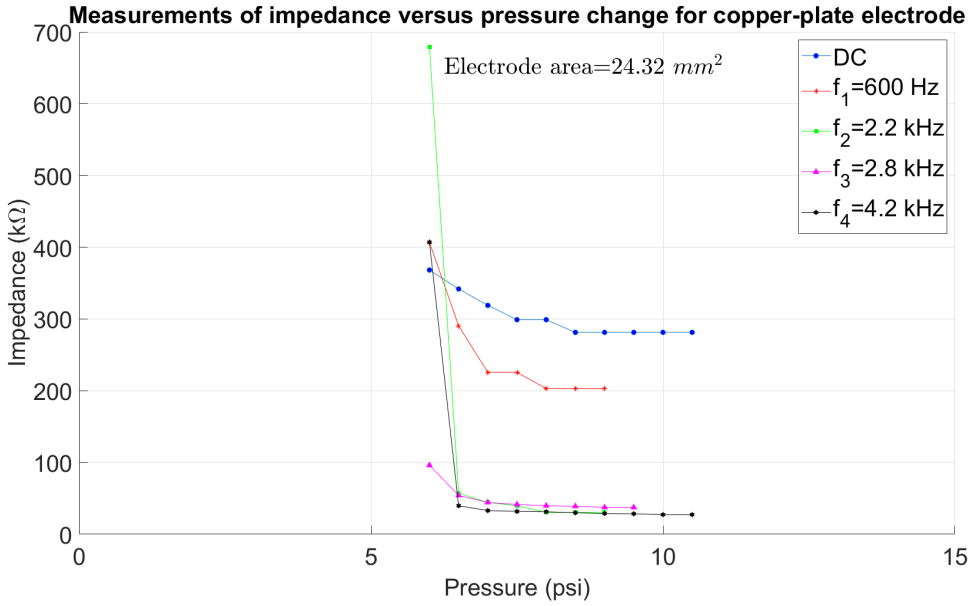

Figure 4.49: Copper-plate electrode impedance variation vs pressure change (cubic structure with a sqaure base of 4 mm by 4 mm and a height of 520 μm).

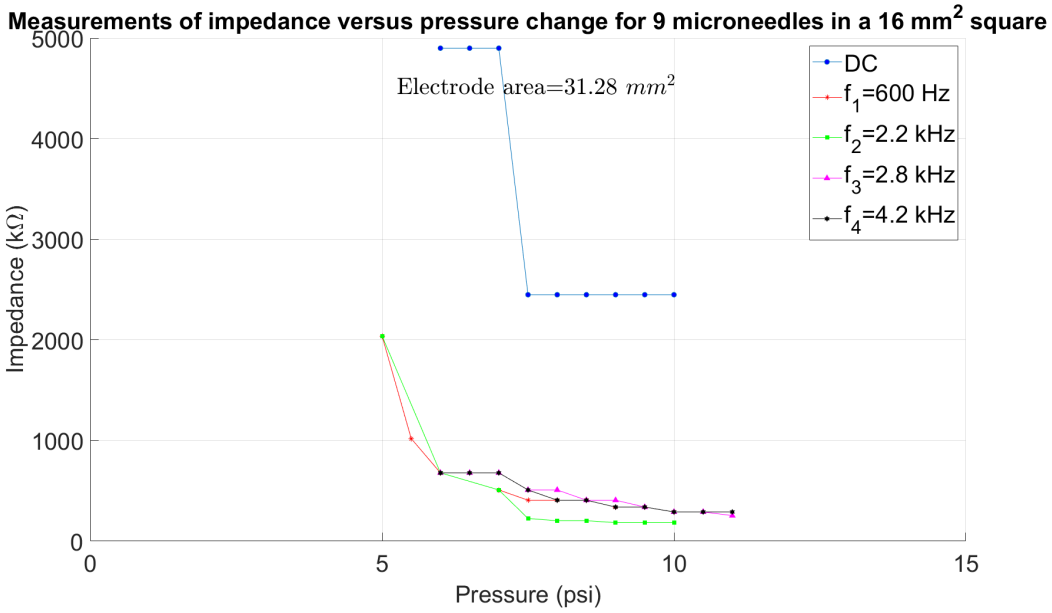

Figure 4.50: Variation of micro-needle electrode impedance vs pressure change (cone structure with a base radius of 0.5 mm and a height of 1.5 mm).

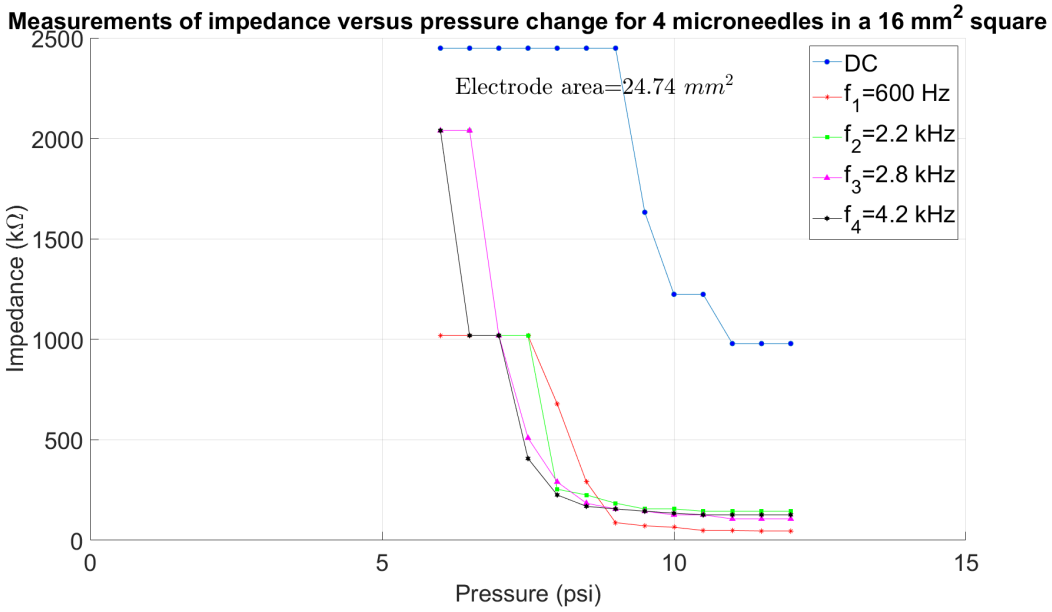

Figure 4.51: Variation of micro-needle electrode impedance vs pressure change (cone structure with a base radius of 0.75 mm and a height of 1.5 mm).

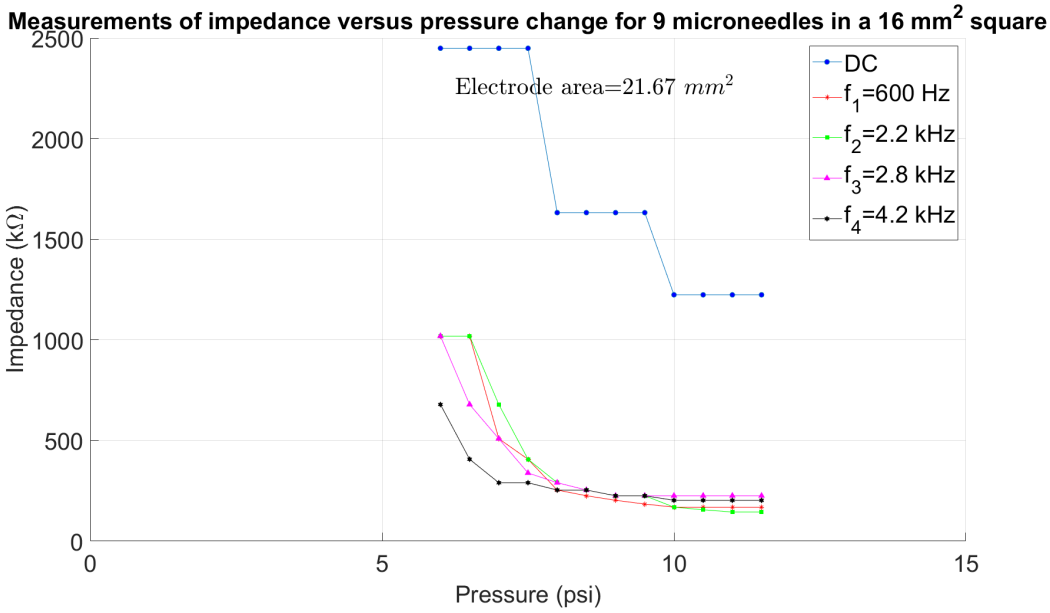

Figure 4.52: Variation of micro-needle electrode impedance vs pressure change (cone structure with a base radius of 0.5 mm and a height of 0.75 mm).

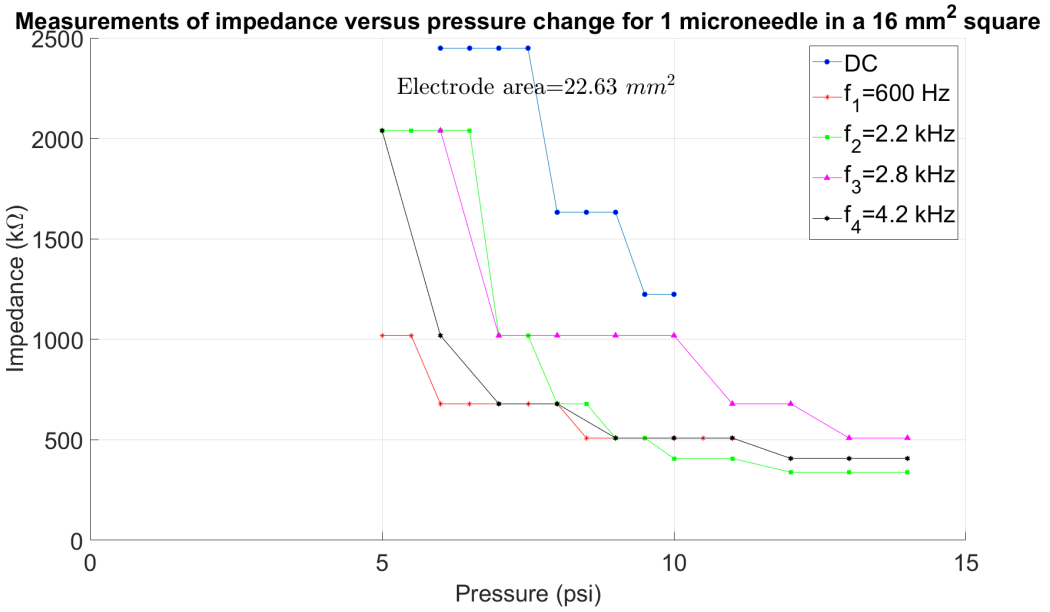

Figure 4.53: Variation of micro-needle electrode impedance vs pressure change (pyramid structure with as square base of 4 mm by 4 mm and a height of 2 mm).

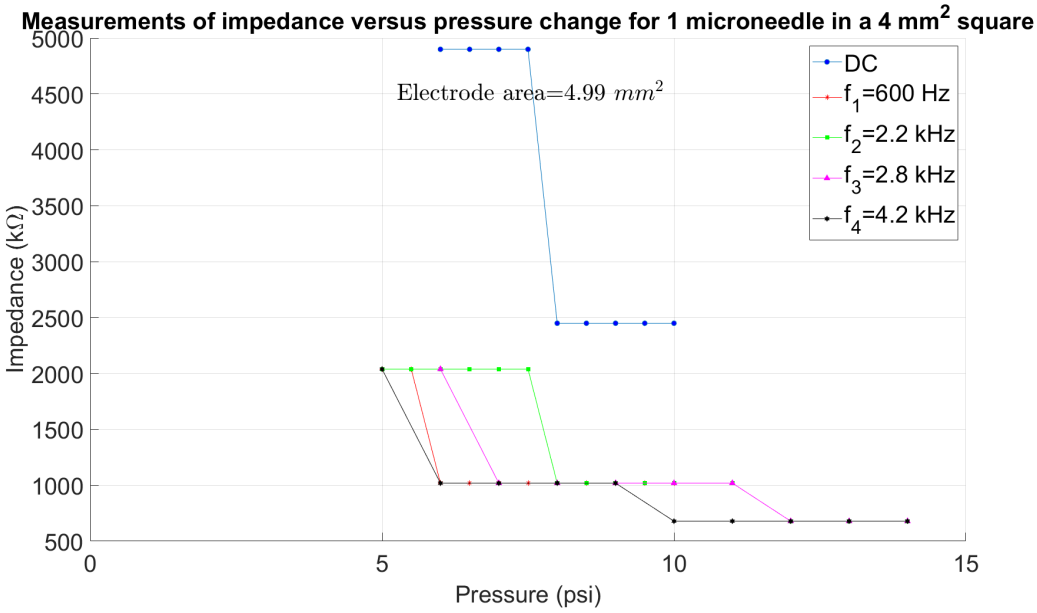

Figure 4.54: Variation of micro-needle electrode impedance vs pressure change (cone structure with a base radius of 0.75 mm and a height of 0.9 mm).

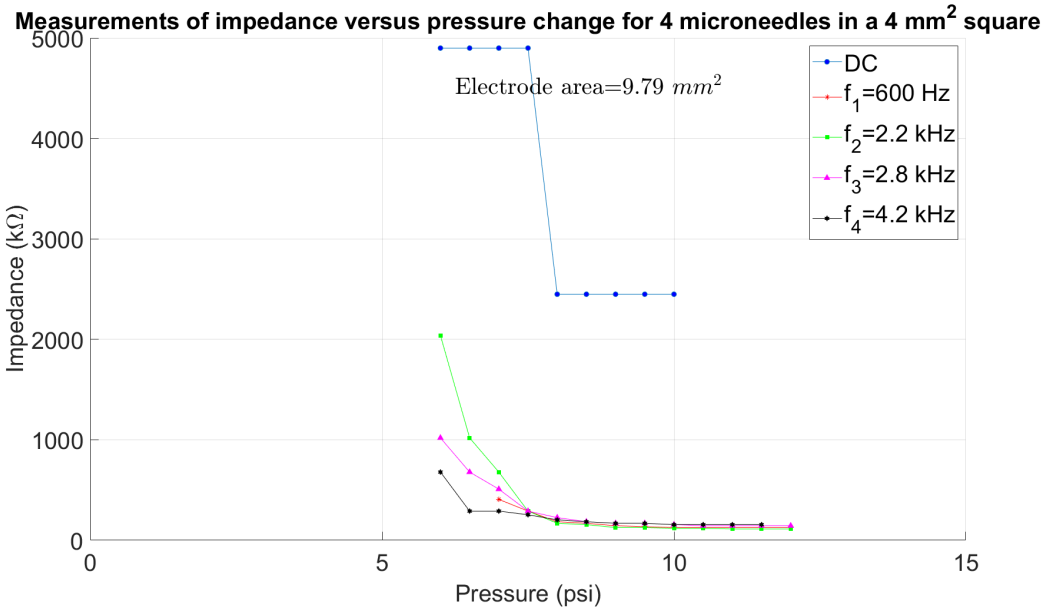

Figure 4.55: Variation of micro-needle electrode impedance vs pressure change (cone structure with a base radius of 0.4 mm and a height of 1.5 mm).

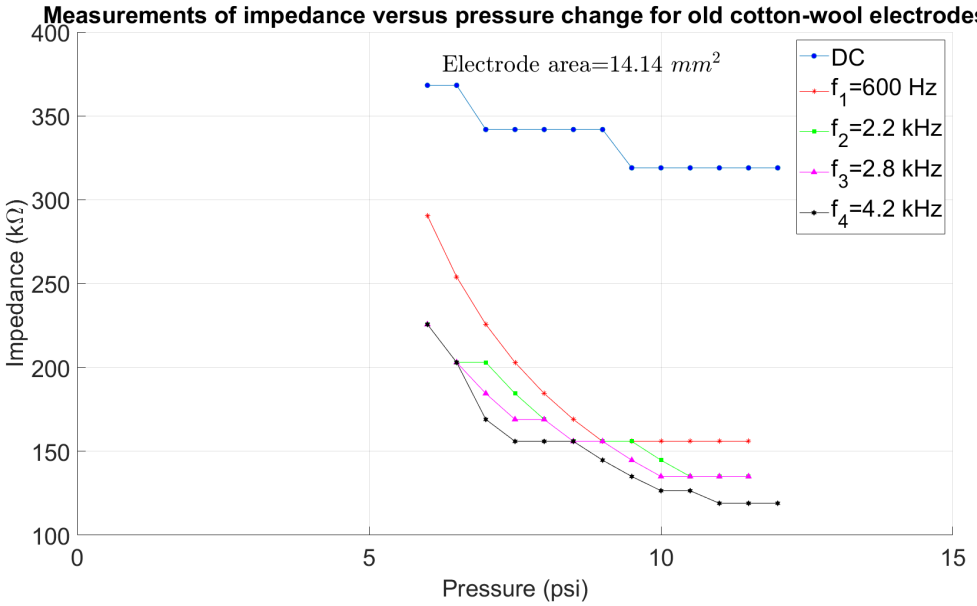

Figure 4.56: Variation of cotton-wool electrode impedance vs pressure change (an ellipse with diameters of 2.5 and 6 mm). The electrode contact with the phantom is enhanced by increasing the inflated balloon pressure.

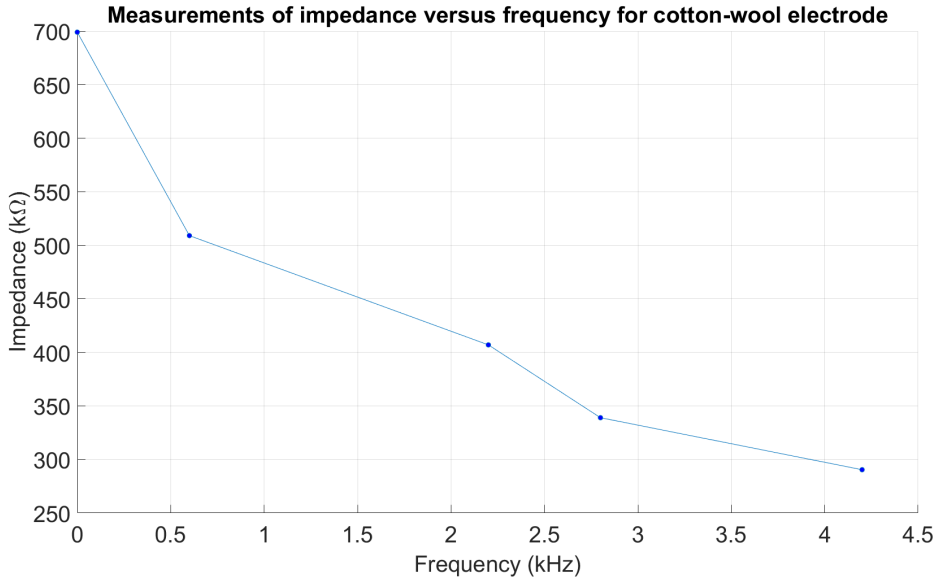

Figure 4.57: Cotton-wool electrode impedance in different frequencies without applying any pressure. The electrode is fixed on the phantom with visually complete contact via a sticking plaster. It is not subjected to the varying balloon pressure. No increasing pressure (inflated balloon) is applied here in this experiment.

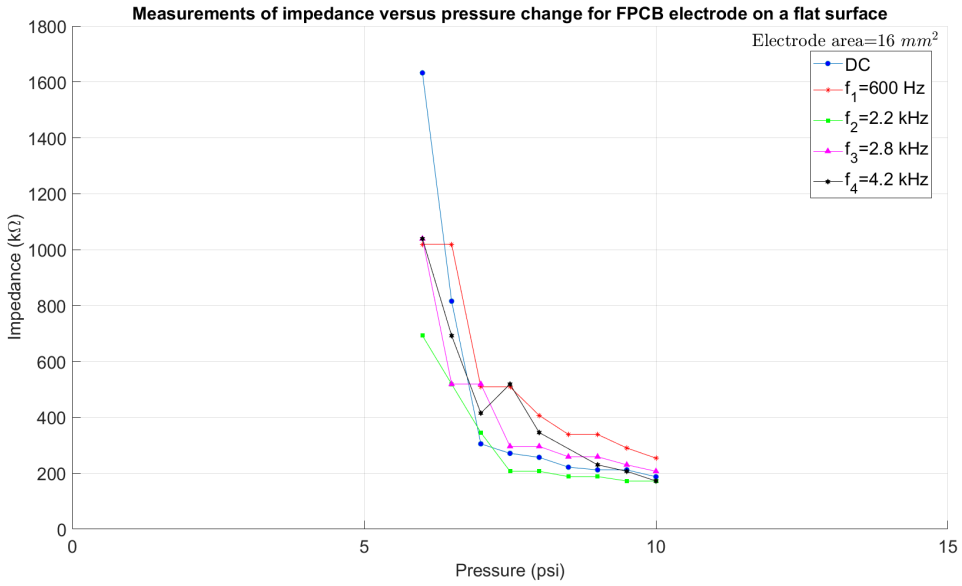

Figure 4.58: Variation of micro-needle electrode impedance vs pressure change (thin structure with a sqaure base of 4 mm by 4 mm and a height of almost zero).

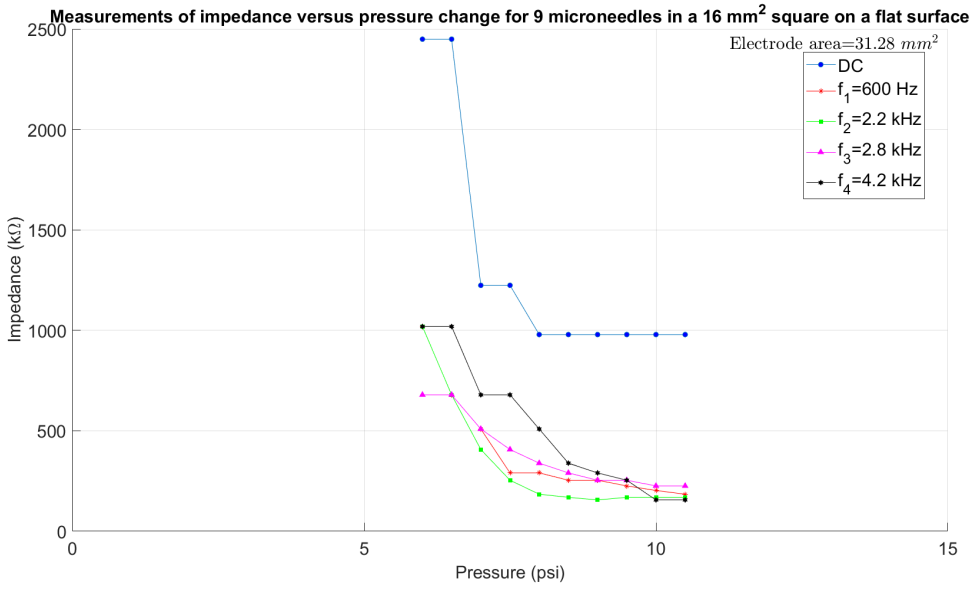

Figure 4.59: Variation of micro-needle electrode impedance vs pressure change (cone structure with a base radius of 0.5 mm and a height of 1.5 mm).

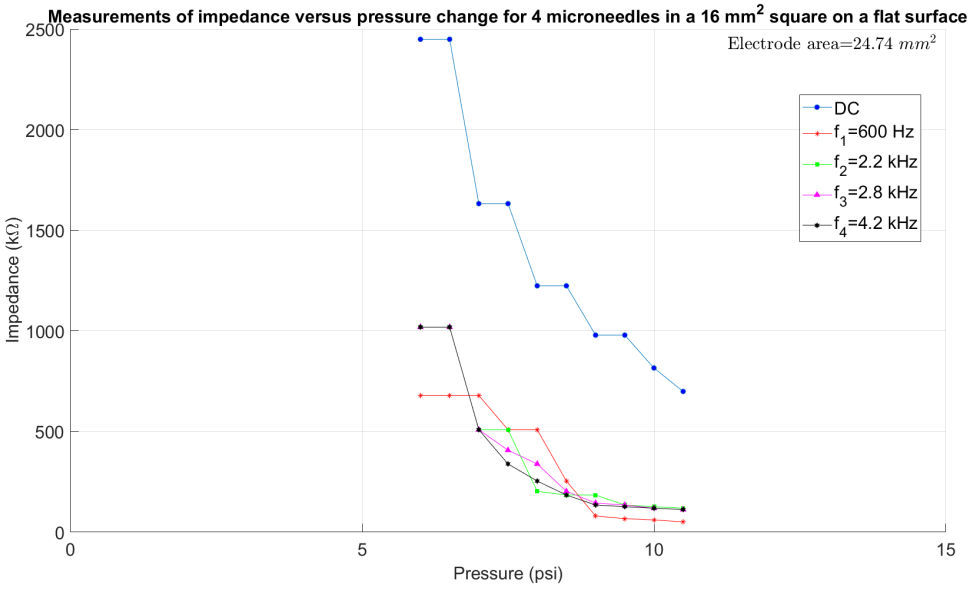

Figure 4.60: Variation of micro-needle electrode impedance vs pressure change (cone structure with a base radius of 0.75 mm and a height of 1.5 mm).

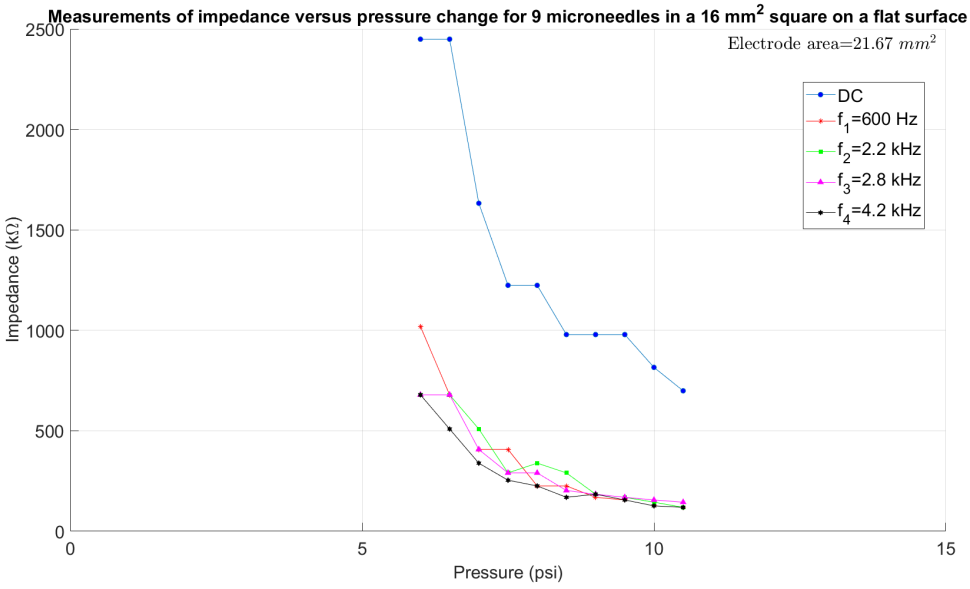

Figure 4.61: Variation of micro-needle electrode impedance vs pressure change (cone structure with a base radius of 0.5 mm and a height of 0.75 mm).

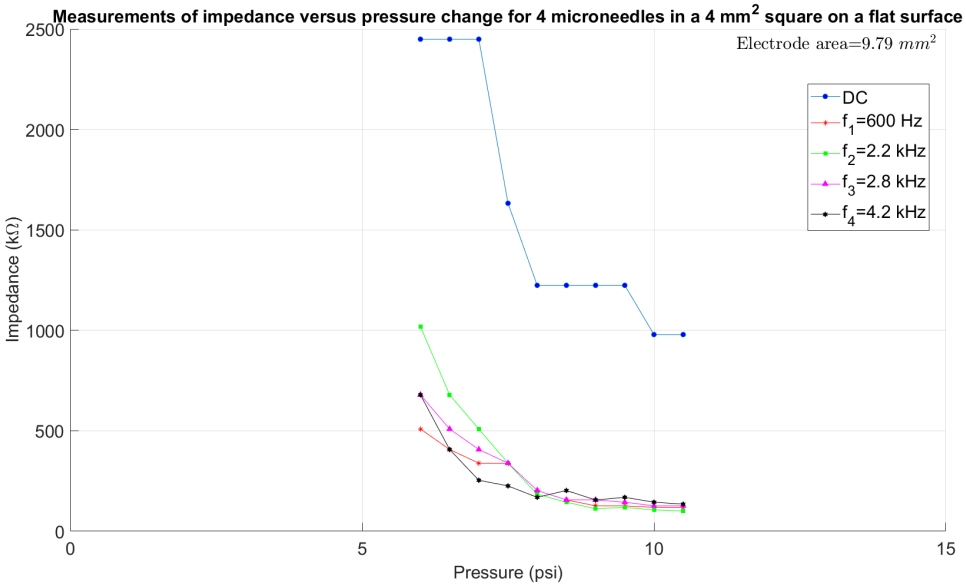

Figure 4.62: Variation of micro-needle electrode impedance vs pressure change (cone structure with a base radius of 0.4 mm and a height of 1.5 mm).

5

Results and discussion

Being concerned with proposing a novel design for an electrode with the in-canal fixation capability and pressure-controlled reducible interfacing-impedance, we did a literature review of Bio-MEMS electrodes fabrication, introduced some immature methodologies correspondingly, adopted a more focused model-reduction-based mature methodology (solution) out of them, went on a fabrication journey accordingly based on additive manufacturing (SLA-3D-printing), MEMS fabrication (sputtering) and medical balloon usage, and carried out some experiments to verify our hypothesis in the previous chapters. Our analysis of the results, discussion about the yields and conclusive remarks can be expressed and itemized separately within the following significant various but related parts and topics:

The designed and assembled structure, which is comprised of a 6 or 8 fr-size silicone/latex Foley balloon catheter, FPCB electrodes, and micro-needles, show a configuration embeddable inside the FDM 3D-printed approximate ear canal model and may be potentially adopted in future for in-vivo EVestG recording after solving bio-compatibility issues, minimizing risk factors, and acquiring (quality) medical regulatory standards.

SLA 3D-printing can be used for printing 1, 4, 5 and 9 micro-needles in an square

with an area of $4\,mm^2$ with a height of $0.75\,mm$ to $1.5\,mm$.

The plastic (cured-resin) 3D-printed micro-needles can be coated with silver which is a commonly-used metal in medical signal acquisition applications.

FPCB electrode shows good conformability with the arc shapes such as the FDM-3D-printed approximate ear canal model.

Controlled pressure of the inflatable substrate of the electrode can reduce the electrode interfacing (contact) impedance. The proposed configuration of the designed and fabricated electrode has the potentiality of removing the conductive gel usage due to impedance reduction as the test results in Fig. 4.46 to 4.55 demonstrated in Section 4.9. All this could be clarified making the following itemized analysis while affirming some other results. The surface area of the microneedle and the smoothed cotton-wool electrodes are caluculated from the following equations (regarding the diagram in Fig. 4.30):

$$S_c = a_s^2 - n_m \pi r_m^2 + n_m \pi r_m \sqrt{r_m^2 + h_m^2}\,, \tag{5.0.1a}$$

$$S_p = 2a_s \sqrt{\frac{a_s^2}{4} + h_p^2}\,, \tag{5.0.1b}$$

$$S_{cw} = \frac{\pi}{4} a_{cw} b_{cw}\,. \tag{5.0.1c}$$

S_c, S_p, and S_{cw} are the areas of conic, pyramidal and elliptic cotton-wool electrodes, respectively. a_s, n_m, r_m, and h_m are also the base square side, number of the cones, cone base radius, and cone height, respectively. h_p is the pyramid height. a_{cw} and b_{cw} are the ellipse diameters of the minor and major axes, respectively. The calculated area of the microneedles, which is a second-dimension quantity, is assumed to have maximum of two decimal digits of accuracy since the step and height resolutions in our 3D-printing are about 0.1 mm.

1. For the FPCB electrode, regarding Fig. 4.46, 4.47 and 4.48:
    - Impedance magnitude ($|Z|$) reduces as pressure increases due to better

contact of the pad with the skin phantom, regarding the following equations:

$$R = \rho \frac{l}{A}\,, \tag{5.0.2a}$$

$$C = \epsilon_0 \epsilon_r \frac{A_{cap}}{d_{cap}}\,, \tag{5.0.2b}$$

$$Z = R - \frac{j}{C\omega}\,, \tag{5.0.2c}$$

$$|Z| = \sqrt{R^2 + \frac{1}{C^2\omega^2}}\,. \tag{5.0.2d}$$

Length (l) reduction and area (A) increase for R in DC state results in resistance (R) decrease while reduction of distance (d_{cap}) for C yields increase of the capacitance (C). This happens when the pressure increases.

- The reduction rate is greater for AC status because in AC state both frequency (ω) and C increase but in DC state just one physical factor (effective area) increases with respect to pressure growth.
- Impedance of AC state is reduced more in comparison with the DC state because capacitive reactance ($X_c = \frac{1}{jC\omega}$) is inversely proportional to both the frequency and the capacitance.

2. For the copper-plate electrode, considering Fig. 4.49 in the previous chapter:
   - Results of impedance-pressure variation almost exist for the copper-plate electrodes, similar to the FPCB type.
   - Although the copper-plate electrode has more subjected area, its impedance is similar to and comparable with the FPCB type because the FPCB electrode is flexible and conformable with cylindrical shape of the phantom.
   - For the copper plate electrode, the sensitivity to pressure change is less because of the non-deformability or inflexibility of the electrode as a function of pressure since the physical characteristics such as area and distance (length) do not change as pressure alters due to the electrode

rigidness.

3. Comparison of two micro-needle electrodes with the same height (9 microneedles in a 16 mm^2 with 4 micro-needles in a 16 mm^2), regarding Fig. 4.50 and 4.51:
    - Impedance reduces as pressure increases due to better contact of the electrode with the skin phantom for the micro-needles as well.
    - The electrode area does not influence the impedance here as it is the microneedle penetration which plays a role in the impedance reduction.
4. Comparison of micro-needle electrode (9 micro-needles in a 16 mm^2 square base) with FPCB electrode (16 mm^2 square base), regarding Fig. 4.50, 4.51 and 4.52 vs Fig. 4.46, 4.47 and 4.48:
    - Although the FPCB electrode has considerably greater flexibility in contacting the surface area in comparison with the micro-needle electrodes, their impedance values are close to each other and comparable because the micro-needles penetrate the skin phantom and reduce impedance. We can see that there is a rival for impedance reduction between conformability (effective contact area) and penetration capabilities of the two types of electrodes, for an artificial skin which probably does not mimic the real behaviour of deeper conductive layers of epidermis efficiently. For more clarification, it is regarded that the flexibility of the FPCB is greater than the microneedle electrodes. However, one may pay attention to this point that in real situation, micro-needles penetrate epidermis, reaching SC and SG which show more electrical conductivity in practice. The reason for facing not more explicit results, supporting absolute out-performance of penetration over conformability in our experiment, is that the skin phantom likely does not have (probably proves not to have) a gradient texture similar to the real

skin as if the deeper penetrated, the less its impedance would be.

- For micro-needle electrodes, the sensitivity to pressure change is more in comparison with the FPCB or copper-plate electrodes because of the so-called *contact* or *touch probability function* which has more number of values in its range. Vaguely speaking, one may assign {0,1} to the range of the probability touch function while one may assign {0, 1/9, 2/9, 1/3, 4/9, 5/9, 2/3, 7/9, 8/9, 1} to it, for flat and micro-needle types of electrodes, respectively.

5. Comparison of two micro-needle electrodes; 9 micro-needles in a 16 mm^2 square base vs single micro-needle in a 16 mm^2 square base (with different shapes and surface area), regarding Fig. 4.52 and 4.53:
   - Impedance decreases as pressure grows up due to better contact of the electrode with the skin phantom.
   - Although the effective area has influence over the impedance, the number of micro-needles is also important. Single micro-needle electrode demonstrates not being useful to reduce impedance in comparison with multiple micro-needle electrode. In other words, the effective area is important when there are multiple micro-needles; one may also rephrase it like this: the efficacious area is significant when there is enough penetration.
6. Comparison of two micro-needle electrodes; 4 micro-needles in a 4 mm^2 square base vs single micro-needle in a 4 mm^2 square base, regarding Fig. 4.54 and 4.55:
   - Impedance reduces as pressure increases due to improved contact of the electrode with the skin phantom.
   - The number of micro-needles is consequential. Single micro-needle electrode shows futility to decrease impedance in comparison with

multiple-micro-needle electrode.

7. Comparison of two micro-needle electrodes; 9 micro-needles in a 16 mm^2 square base vs 4 micro-needles in a 4 mm^2 square base, regarding Fig. 4.50, 4.52 and 4.55:
    - Not only do the effective area or the number of micro-needles (penetration) play role in impedance reduction, but also the electrode total size relative to the canal (conformability with the canal or penetration to corrugations) affect the impedance reduction. Reduction of impedance in $4mm^2$-micro-needles is almost more in comparison with $16mm^2$-micro-needles as pressure increases due to better contact of the smaller electrode with the curved wall of the cylinder (better reaching of the skin in corrugations).
    - Vaguely and visually speaking, the impedance reduction might be more dynamic (sensitive) vs pressure variation because the contact or touch possibility function accepts more members in range (6 vs 11 members) or ({0, ¼, ½, ¾ ,1} vs {0, 1/9, 2/9, 1/3, 4/9, 5/9, 2/3, 7/9, 8/9, 1}), for the two types of micro-needles, respectively. This implies more spatial resolution as a function of manipulative pressure when there are more numbers of micro-needles. For verifying this discussion on the ground as a future research trend, it is required to increase the pressure with a micro-pump to enhance the sweeping steps and have more data points of (pressure,impedance).
8. Analysis of the behaviour of the cotton-wool electrode when subjected to pressure change, regarding Fig. 4.56:
    - Impedance diminishes as pressure grows up due to enhanced contact of the electrode with the skin phantom.
    - The efficiency of the conductive-gel-smeared cotton-wool electrode is comparable with all other electrodes which are not using conductive

gel. Thus, pressure-actuation for FPCB/micro-needle electrodes can most probably remove usage of conductive gel which might be bothering in bio-signal acquisition or might be making short circuits along the canal (malfunctioning the differential mode).

9. Analysis of the behavior of the cotton-wool electrode when subjected to frequency sweep in comparison with other types of proposed electrodes, regarding Fig. 4.57 and Fig. 4.56 as well as previous plots:
   - At higher frequencies, the cotton-wool electrode shows less impedance.
   - All the FPCB, copper-plate and micro-needle electrodes function as lowpass filters.
   - However, the frequency response of the electrodes are a little bit different because the materials (cotton-wool, plastic, silver, copper, electrolyte) form distinct capacitors in the circuit. They add various poles and zeros in the frequency response transfer function of the system.
10. Performance on a flat surface: The results, displayed in Fig. 4.58 to 4.62, demonstrate that micro-needles mostly show lower impedance or comparable values in comparison with FPCB electrodes. In other words, although the micro-needles have much less flexibility in contacting the surface in comparison with FPCB electrode, they show about 50 to 70 kΩ less impedance for AC frequencies.

By and large, MEMS fabrication process have been applied by many researchers to build micro bio-electrodes for recording bio-potentials ranging from μV to mV including ECG, EEG, EMG, and ECoG. They are directly used to fabricate BioMEMS (micro) electrodes or are indirectly exploited to enhance some of the most important properties of big-size electrodes such as bio-compatibility and conductivity. These big-size (millimeter-dimensions) features may be built via some other methods such as additive manufacturing (3D-printing), micro-milling, hot

embossing, injection molding, and PDMS casting. Here in our thesis, our approach mainly included additive manufacturing, enhancement of the properties of the 3D-printed electrode via MEMS PVD, and exploitation of some medical tools. In other words, an electrode device was proposed and fabricated through assembly of different elements including a medical balloon (as the inflatable actuation system), FPCB (as active/passive electrode or electrode holder/base), copper/silver ball (as active electrode), metal-coated/conductive plastic SLA-3D-printed micro-needles (as active electrode), cotton-wool tip (as active electrode) as well as LEDs and fibre optic strands (for illumination purposes). The fabricated electrode device could get fixed in a funnel-shaped canal (an approximate ear canal model). The experiments demonstrated that the impedance of the electrode could be reduced via application of pressure to the electrode balloon actuation system.

In addition to the above-paragraph conclusive remarks, we may also express some other outcomes during our fabrication journey:

- FDM 3D-printing of a single micro-needle with a height of less than 2 mm and on a base with an area of less than $16\,mm^2$ (4mm-by-4mm) with acceptable surface roughness was not possible.
- SLA 3D-printing of 4 or 5 micro-needles with the minimum height of $500\,\mu m$, $750\,\mu m$ or 1 mm on a basis with an area of $4\,mm^2$ (2mm by 2mm) with acceptable surface roughness is quite feasible and was obtained. The height and plane step resolutions could be considered as $100\,\mu m$, and $80\,\mu m$, respectively.
- SLA-3D-printed micro-needles dramatically outperforms the FDM-3D-printed ones in terms of surface roughness and resolution, and even bio-compatibility due to the possibility of usage of bio-compatible resins.
- Silver can be sputtered over the plastic SLA-3D-printed and FDM-3D-printed micro-needles with acceptable step coverage to make them conductive without melting the (PLA or cured-resin) plastic micro-needles inside the chamber

during the sputtering process, through setting the chiller temperature, power supply energy and timing management.

- Silver epoxy conductive glue can be used for mounting the micro-needles on the FPCB showing great (shear) mechanical resistance against increasing pressure (without separation and any failure) and bringing about nice conductivity.
- FPCB technology can be considered as an outstanding asset to be used for building polyamide-metal micro-structures instead of using the conventional lab MEMS fabrication process (photolithography, electroplating, RIE, and wet etch) with preference in terms of cost and time-efficiency.
- Foley balloon catheter can be exploited as a bio-compatible inflatable actuation system to move the electrodes up and down, showing good conformability and acceptable reliability for the low pressure application.
- Although the FPCB can be applied as a reliable holder for the micro-needles, the trimmed FPCB by itself would be used as a good conformable electrode.
- G-code parameters can enhance resolution and reduce surface roughness in FDM 3D-printing of micro-needles to some extent.

6

Future research directions

In addition to the research questions, mentioned as hints in Section 3.1, one may also consider the following questions for developing and establishing a research framework in future to reach an evolved design for an EVestG electrode:

5. How can we reduce the antenna effects between electrodes and signal acquisition electronics?
6. What are the optimized designs for signal acquisition electronic hardware to reduce environmental noise and boost CMRR?
7. What is the suitable distance of the electrode from the ED to record the signal?
8. What is an efficient electrode design for picking up the signals from the described areas?
9. What are the desired electrode sizes including surface area and height from the actuation platform?
10. What types of material can be used as substrates, metal electrode micro pads/needles, adhesives, electrode actuation bodies, etc.?

There are some assumptions, addressing the above questions. First off, we have access to the stimulation tilted chair and noise-protected chamber for EVestG recording purposes. Secondly, there is a tested amplifier for EVestG recording. However, they

suffer from antenna and CMRR problems to some extent. Thirdly, there is software for EVestG signal processing and analysis. Lastly, there is also an implementation ongoing design for the electronic signal acquisition and instrumentation hardware hinted as the headset in Fig. 2.5 and 2.6 (part D and E).

The EVestG electrode design can be dealt with by fabricating a miniaturized electrode device which is guided through the ear canal to reach the wall near the TM (point A) as well as the outer ear canal (point B). The points are displayed in Fig. 2.4 and 2.5. Another complementary solution is shortening the antenna (C wires in Fig. 2.5a), exploiting a Compact Discrete Component (CDC) design of instrumentation and signal conditioning units all packed in a headset worn over the patient's ear as depicted in Fig. 2.5b (part D and E). The other ambitious solution is an Integrated Circuit (IC) design which entails all the electronics of instrumentation, amplification, filtration, Analog-to-Digital (A/D) conversion and digital storage micro-controller all in one or two ICs.

Deeming the above challenges, it is believed that this research may be continued to optimize the design and enhance it in such a way that it can finally lead to fabrication of an efficient and bio-compatible medically tested (standard) electrode for EVestG recording. The research major prospectives are suggested as the following future work topics and milestones:

Simulator: Designing and building an EVestG simulator for testing the electrodes, inside the ear canals subjected to up-down and tilting movements, is possibly one of the research future trends. It should be capable of applying EVestG signal in coordination with the type of the movement and synchronously with it. Figure 6.1 conceptually suggests a basic solution for such a testing platform. An m-file code may generate the field potential in MATLAB, and send it to an Arbitrary Waveform Generator (AWG); see Fig. 6.2. Then, the signal is attenuated to the ear canal models while the MATLAB code controls the movement/positioning of the

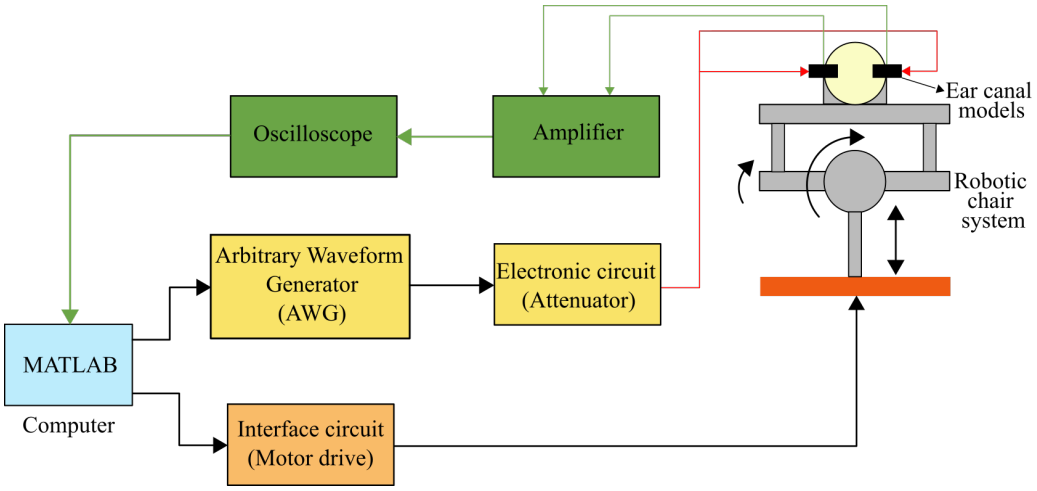

Figure 6.1: Concept of a simulation platform for EVestG electrode testing inside the ear canal models.

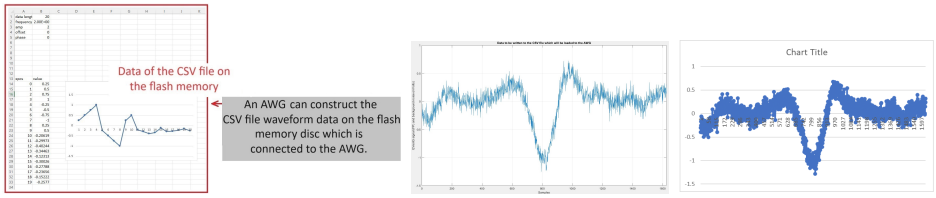

(a) (b) (c)

Figure 6.2: (a) Reconstruction of a signal via a CSV file from an AWG: the data can be sent to the AWG via a flash memory disc or a LAN port from the computer (MATLAB). A noisy EVestG signal can be generated by MATLAB (Fig. 6.2b), converted to CSV (Fig. 6.2c) and sent to AWG.

stimulation chair.

Integration: One of the best solution to enhance CMRR is to reduce the distance between the amplifier and the electrodes or even to integrate the electrodes with the instrumentation amplifier. Figure 6.3 basically draws such an integration in a block diagram. The circuits inside the blocks are presented in details in Fig. 6.4. For notch filter, one may use UAF42 application circuit [4, 109].

Change of metal coatings: Sputtering different metal targets such as copper, gold, and titanium over the plastic micro-needles should be investigated and a comparison of the quality of the coated micro-needles should be done. Especially, titanium coating is of great interest because of remarkable bio-compatibility and less

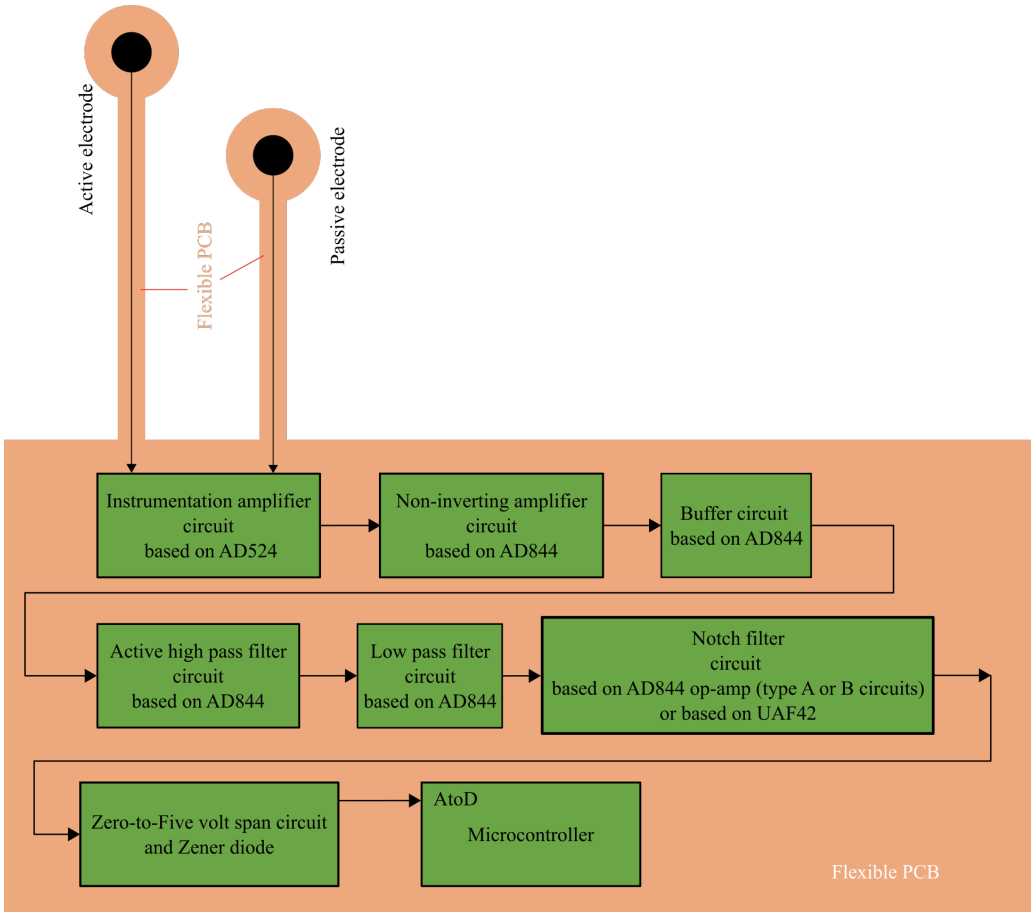

Figure 6.3: Schematic block diagram of an integrated amplifier-electrode circuit on a single FPCB to reduce noise and enhance CMRR.

toxicity when the micro-needles penetrate the SC and SG. It should be investigated whether it is necessary or not to deposit any adhesion layer before sputtering other main metal layers, including gold, copper, and titanium, over the plastic micro-needles. The micro-needle can also be SLA-3D-printed out of a medical-grade resin. Note that we used silver in our experiments since it is a commonly used material in the structure of many commercial standard bioelectrodes and it has low toxicity in the human body. The wire of the currently used tub-wise unactuated electrode is also a silver wire. This may be significant in the comparative studies in the future in in-vivo tests.

Application of conductive bio-compatible paint: One of the interesting and significant future research developments which can be followed is painting the

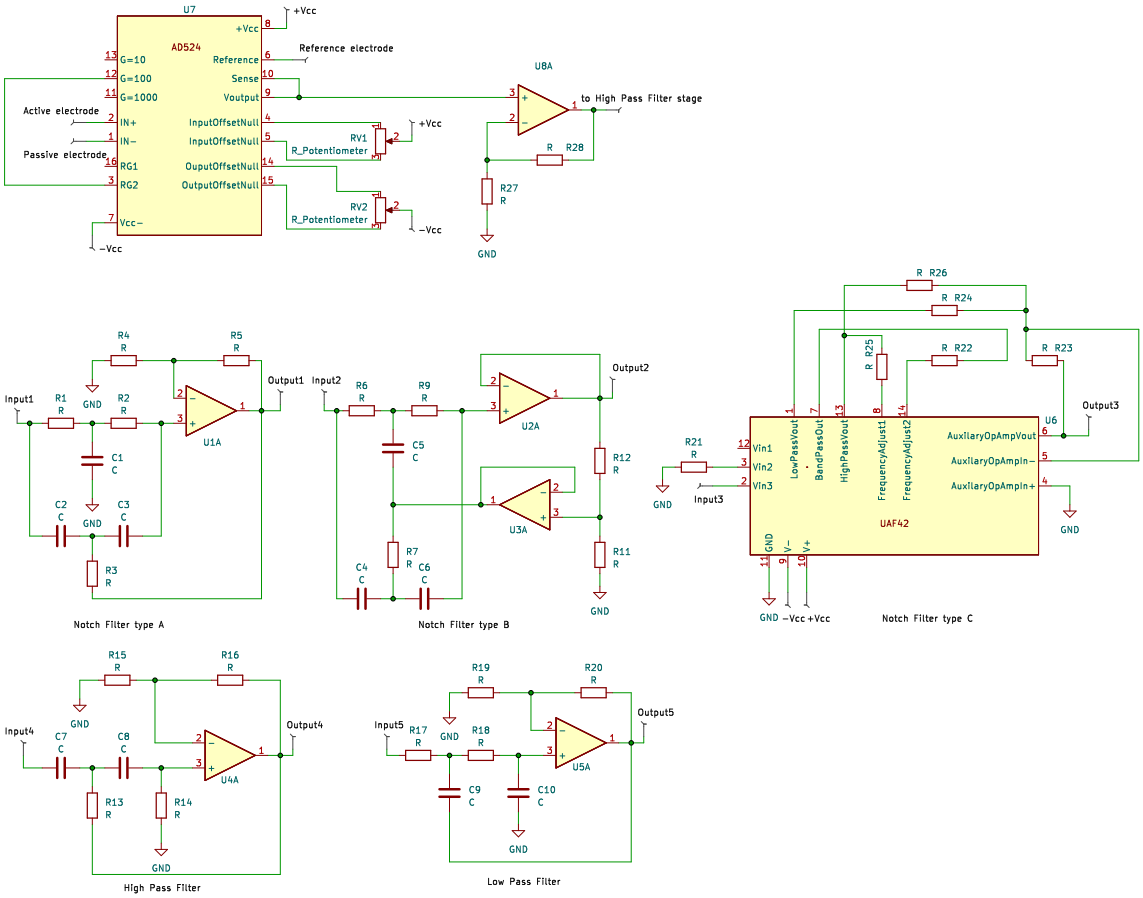

Figure 6.4: Circuits of the block diagram in Fig. 6.3 including AD524 instrumentation amplifier, high pass filter, low pass filter, and notch filter. We may recommend AD844 or AD829 op-amps for building the filter circuits as well as secondary stage gains/buffers, regarding low noise, low offset, great slew rate and high bandwidth.

plastic micro-needles with conductive coating because not only the used conductive paint in our experiments is bio-incompatible, but also the sputtering process is time consuming and costs considerably. One of the interesting alternatives might be using a kind of spray, dispersible bio-compatible coating such as PEDOT:PSS. One may think of using Clevios PH 1000 Aqueous PEDOT / PSS dispersion, blue liquid in similar applications [86, 32, 43].

Application of bio-compatible glue: The epoxy silver conductive glue used for attachment of the micro-needles over the FPCB is not bio-compatible. Although it is under the micro-needle base and is not in direct touch with the skin, more high standard safety considerations and contamination on side-walls during

assembly/fabrication require one to think over a bio-compatible conductive glue.

3D-printing conductive polymers: Feasibility of SLA 3D-printing of PEDOT:PSS resin can be studied as an interesting alternative to directly build conductive plastic micro-needles.

Micro-needle geometry reduction vs redundancy increase: For achieving micro-needles with smaller dimensions, less height and more numbers of them over a square or circular FPCB, the micro-needle fabrication methodology should be changed. Additive metal laser technologies such as SLS and DMLM should be considered as alternatives, regarding their capabilities in 3D-printing fine metal features. However, silicon lithography and sputtering always remain as a reliable method for building ultra-fine micro-needles at the cost of time and money.

Conductive foam: We also think if we can make the ear plugs conductive through sputtering. If so, they shrink for insertion into the ear canal and expand later to conform with the ear canal to establish the contact.

Dog-bone structure: The feasibility of fabrication of 6 or 8 fr-size dog-bone Foley balloon catheter is of great interest and importance. It should be designed in such a way that each balloon can accommodate active and passive FPCB-based micro-needles, independently.

TM Sensor: Another interesting enhancement to the electrode is adding MEMS proximity sensor at the tip of the catheter. One may also consider passing two fibre optic strands through the active ball tip electrode: one for Infra-red (IR) sender and one for IR receiver to detect TM as the obstacle. The fibre optic strands reach the sender and receiver LEDs on the obstacle detection electronic circuit out of the ear canal installed on the catheter. The required circuit for detecting the obstacle is a 555 timer application circuit [3]. Figure 6.5 should be integrated with the electrode FPCB.

Removing sharp tips of ball electrodes: We have used balls already having

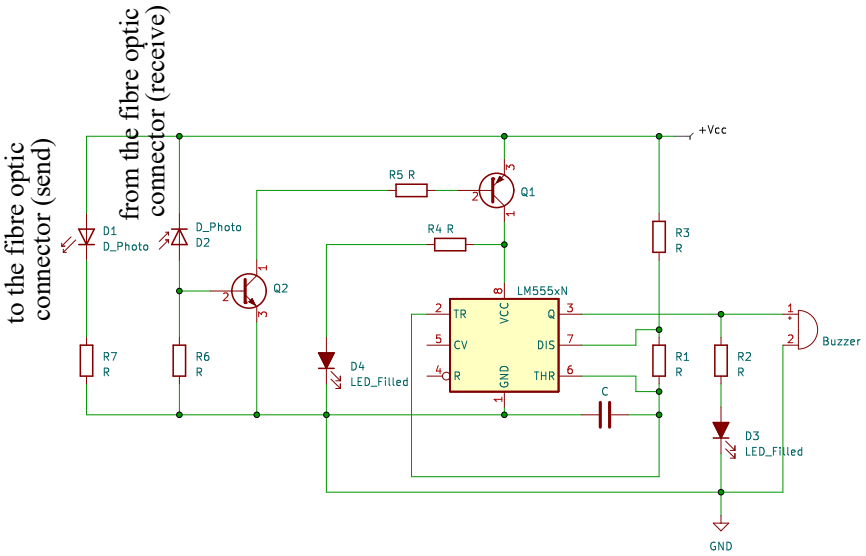

Figure 6.5: IR send/receive obstacle detection/sensing circuit.

through-all holes since drilling such small balls is hard due to difficult fixation of the ball while drilling. This sometimes causes sharp bumps/corners while soldering the wire to the copper ball. A scheme in Fig. 6.6 is presented to accommodate 2, 3, or 4 mm balls and hold them for drilling 0.25, 0.5, 0.75, and 1 mm holes, instead of through-whole drill of the balls.

Usage of stretchable materials: Two fantastic approaches might be adopted as future research activities on usage of not only flexible but also conformable, compressible and stretchable materials. The first one is redesign of the FPCB into a Stretchable PCB (SPCB) as the base for the micro-needle. The second is SLA 3D-printing of micro-needles with stretchable, flexible and conformable type of medical grade resin. In this case, the SPCB can be attached over the balloon via glue just on two end points of the SPCB, leading to solve the problem of glue curl-up due to less volume of glue application. The conformable micro-needle may also demonstrate better impedance reduction due to better conformability with the corrugated walls of the ear canal. See Fig. 6.7. In case of a successful experiment and implementation of the SPCB-based electrode, one may think of transformation of the design in Fig. 3.13 and 3.12 to an SPCB based one as well. In this case, sputtering over

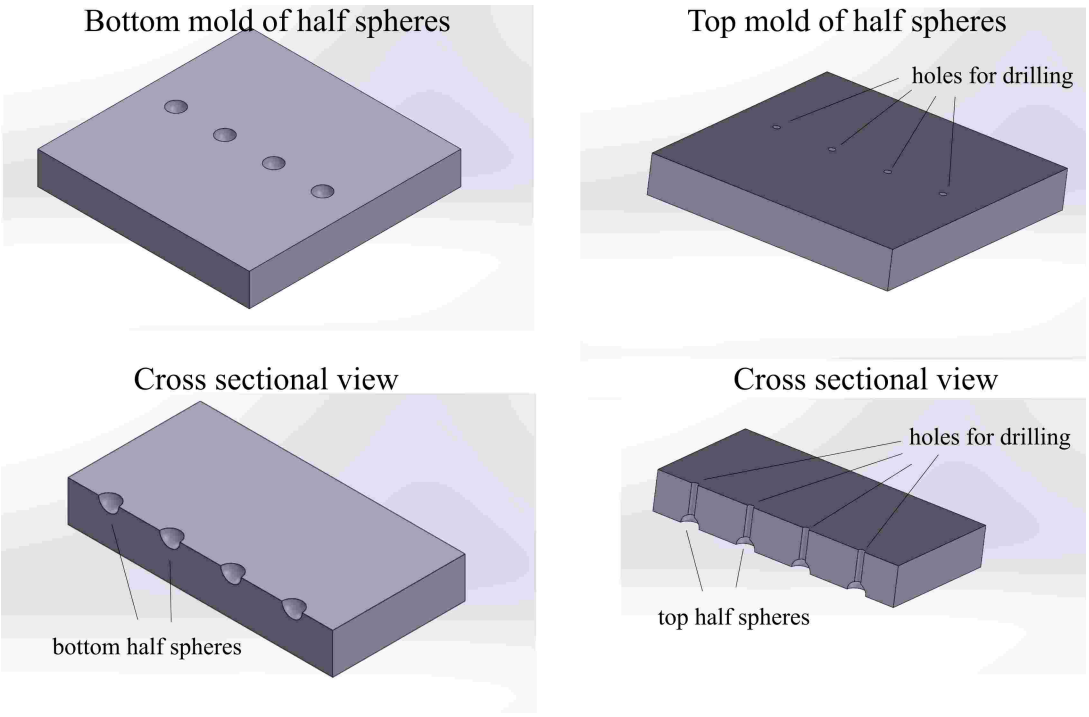

Figure 6.6: SLA 3D-printed molds with cut-extruded half spheres and drilling holes to make holes inside the balls.

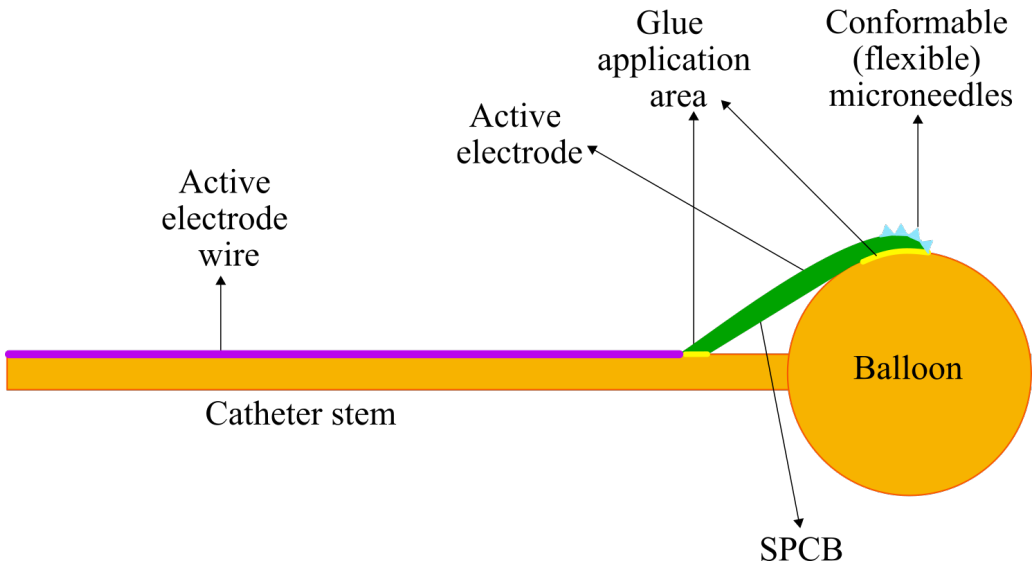

Figure 6.7: Schematics of application of SPCB and flexible micro-needles to reduce glue usage and decrease glue curl-up.

the stretchable/flexible micro-needle should be investigated from the aspect of pre-mentioned concerns in the coating process such as melting of plastic in the chamber, metal-adherence-on-plastic, etc.

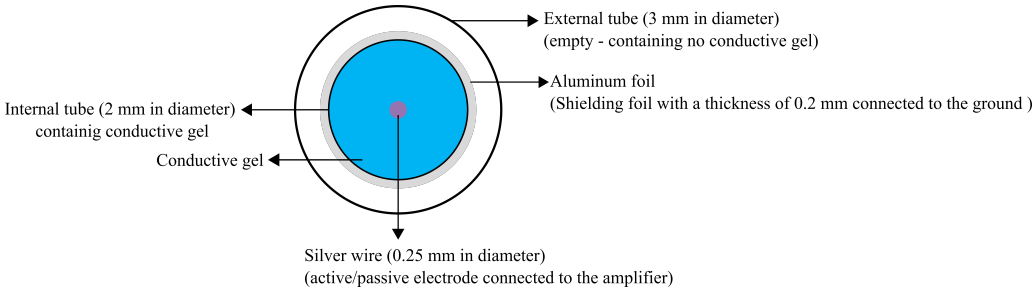

Figure 6.8: Diagram of the shielded unactuated tube-wise electrode for reducing noise (cross-sectional view).

Fabrication of copper/silver/titanium discs: It might be worthwhile exploiting a jewelry metal disc cutter to cut 2, 3, and 4 mm (in diameter) discs out of 0.5 mm thick copper, silver and titanium metal plates. The main plate might be plastic or copper and can be sliver or titanium-sputtered before disc-cutting.

Shielding for noise reduction: Figure 6.8 demonstrates one probable diagram solution clarifying how a shielding structure to cope with noise effects for an unactuated tube-wise electrode (the currently used electrode) to be implemeneted and tested in the future.

By and large, the further developments are grouped into three main categories: 1) developments to optimize the design, 2) enhancement to make the design biocompatible, and 3) design and fabrication of in-vitro test platforms. Having reached a successful development of the mentioned categories, one may prepare other necessities and get the ethics approval for doing in-vivo tests and evaluate the design in a real practical situation.

References

[1] Applications of High-Pressure Balloons in the Medical Device Industry. https://www.mddionline.com/news/applications-high-pressure-balloons-medical-device-industry. Accessed: 2023-10-12.

[2] Biomedical Balloons: Understanding Their Physical and Mechanical Properties. https://www.medicaldesignbriefs.com/component/content/article/mdb/pub/features/articles/40249. Accessed: 2023-10-12.

[3] IR Detector Circuit Using 555 Timer IC. https://www.circuits-diy.com/ir-detector-circuit-using-555-timer-ic/. Accessed: 2023-10-11.

[4] Use Monolithic Universal Active Filter ICs to Speed IoT Analog Front-End Design. https://www.digikey.be/fr/articles/use-monolithic-universal-active-filter-ics-to-speed-iot-analog-front-end-design. Accessed: 2023-10-11.

[5] JE Abele. Balloon catheters and transluminal dilatation: technical considerations. *American Journal of Roentgenology*, 135(5):901–906, 1980. PMID: 6778167.

[6] Parinaz Abiri, Yuan Luo, Zi-Yu Huang, Qingyu Cui, Sandra Duarte-Vogel, Mehrdad Roustaei, Chih-Chiang Chang, Xiao Xiao, Rene Packard, Susana Cavallero, Ramin Ebrahimi, Peyman Benharash, Jun Chen, Yu-Chong Tai, and Tzung K. Hsiai. 3-dimensional electrical impedance spectroscopy for in situ

endoluminal mapping of metabolically active plaques. *Sensors and Actuators B: Chemical*, 354:131152, 2022.

[7] M. Arai, Y. Nishinaka, and N. Miki. Long-term electroencephalogram measurement using polymer-based dry microneedle electrode. In *2015 Transducers 2015 18th International Conference on Solid-State Sensors, Actuators and Microsystems (TRANSDUCERS)*, pages 81–84, 2015.

[8] Mehrangiz Ashiri, Brian Lithgow, Abdelbaset Suleiman, Behzad Mansouri, and Zahra Moussavi. Electrovestibulography (EVestG) application for measuring vestibular response to horizontal pursuit and saccadic eye movements. *Biocybernetics and Biomedical Engineering*, 41(2):527–539, 2021.

[9] J.N.Y. Aziz and R. Genov. Multi-channel integrated neural interfaces for distributed electro-chemical sensing. In *48th Midwest Symposium on Circuits and Systems, 2005.*, pages 1782–1785 Vol. 2, 2005.

[10] Vivekanand Bhatt and Sudhir Chandra. Silicon dioxide films by RF sputtering for microelectronic and MEMS applications. *Journal of Micromechanics and Microengineering*, 17(5):1066, Apr 2007.

[11] H Biederman. RF sputtering of polymers and its potential application. *Vacuum*, 59(2):594–599, 2000. Proceedings of the Fifth International Symposium on Sputtering and Plasma Processes.

[12] Tomasz Blachowicz and Andrea Ehrmann. 3D printed MEMS technology—recent developments and applications. *Micromachines*, 11(4), 2020.

[13] Axel Blau. Prospects for neuroprosthetics: Flexible microelectrode arrays with polymer conductors. In Gaetano D. Gargiulo and Alistair McEwan, editors, *Applied Biomedical Engineering*, chapter 5. IntechOpen, Rijeka, 2011.

[14] Bruno Castilho, Alisson M. Rodrigues, Pedro Renato Tavares Avila, Raíra Chefer Apolinario, Tamires Nossa, Magdalena Walczak, Jucielle Fernandes, Romualdo Menezes, Gelmires Neves, Haroldo Pinto, and Pedro Avila. Hybrid magnetron sputtering of ceramic superlattices for application in a next generation of combustion engines. *Scientific Reports*, 12(1):2342, 02 2022.

[15] Felipe Cemin, Gregory Abadias, Tiberiu Minea, and Daniel Lundin. Tuning high power impulse magnetron sputtering discharge and substrate bias conditions to reduce the intrinsic stress of tin thin films. *Thin Solid Films*, 688:137335, 2019. A Special Issue "Thin Film Advances", dedicated to the 75th birthday of Professor Joe Greene.

[16] Chih-Wei Chang, Li-Wei Ko, Fu-Chang Lin, Tung-Ping Su, Tzyy-Ping Jung, Chin-Teng Lin, and Jin-Chern Chiou. Drowsiness monitoring with EEG-based MEMS biosensing technologies. *GeroPsych*, 23(2):107–113, 2010.

[17] C.W. Chang and J.C. Chiou. Surface-mounted dry electrode and analog-frontend systems for physiological signal measurements. In *2009 IEEE/NIH Life Science Systems and Applications Workshop*, pages 108–111, 2009.

[18] Karen C. Cheung, Yang-Kyu Choi, Tim Kubow, and Luke P. Lee. Nanostructured electrodes for improved neural recording. *MRS Proceedings*, 729:U4.11, 2002.

[19] Karen C. Cheung and Philippe Renaud. BioMEMS for medicine: On-chip cell characterization and implantable microelectrodes. *Solid-State Electronics*, 50(4):551–557, 2006. Special Issue: Papers Selected from the 35th European Solid-State Device Research Conference ESSDERC'05.

[20] Yu Mike Chi, Tzyy-Ping Jung, and Gert Cauwenberghs. Dry-contact and

noncontact biopotential electrodes: Methodological review. *IEEE Reviews in Biomedical Engineering*, 3:106–119, 2010.

[21] Seow Yong Chin, Vishwesh Dikshit, Balasankar Meera Priyadarshini, and Yi Zhang. Powder-based 3D printing for the fabrication of device with micro and mesoscale features. *Micromachines*, 11(7), 2020.

[22] Jin-Chern Chiou, Li-Wei Ko, Chin-Teng Lin, Chao-Ting Hong, Tzyy-Ping Jung, Sheng-Fu Liang, and Jong-Liang Jeng. Using novel MEMS EEG sensors in detecting drowsiness application. In *2006 IEEE Biomedical Circuits and Systems Conference*, pages 33–36, 2006.

[23] Tien-Min Chu, Allen Brady, Weiguo Miao, John Halloran, Scott Hollister, and Diann Brei. Ceramic SFF by direct and indirect stereolithography. *MRS Proceedings*, 542(1):119–123, 01 1999.

[24] N. Circelli and G. Queirolo. A stable tin reactive sputtering deposition process. *Applied Surface Science*, 38(1):304–311, 1989.

[25] S. Crump. Apparatus and method for creating three-dimensional objects, U.S. Patent, No. 512129, June. 1992.

[26] Guanghui Dai, Qingqing Zhang, and Guobao Jin. A model developed for predicting uniformity of kyphoplasty balloon wall thickness based on the orthogonal test. *Advances in Materials Science and Engineering*, 2020:1–8, 05 2020.

[27] Z. A. Dastgheib, B. Lithgow, and Z. Moussavi. Diagnosis of parkinson's disease using electrovestibulography. *Medical and Biological Engineering and Computing*, 50(5):483–491, 05 2012.

[28] Z. A. Dastgheib, B. Lithgow, and Z. Moussavi. Vestibular spontaneous response as a potential signature for Parkinson's disease. In *2012 Annual International*

Conference of the IEEE Engineering in Medicine and Biology Society, pages 3704–3707, 2012.

[29] Giorgio De Pasquale. Additive manufacturing of micro-electro-mechanical systems (MEMS). *Micromachines*, 12(11), 2021.

[30] Giorgio De Pasquale. Design and modeling of MEMS microgrippers for laser based additive manufacturing. *Micro*, 2(2):225–239, 2022.

[31] Carl R. Deckard, Joseph J. Beaman, and James F. Darrah. Method for selective laser sintering with layerwise cross-scanning, U.S. Patent, No. 5155324, Oct. 1992.

[32] Yuping Deng, Hui Qi, Yuan Ma, Shangbin Liu, Mingyou Zhao, Zhenhu Guo, Yongsheng Jie, Rui Zheng, Jinzhu Jing, Kuntao Chen, He Ding, Guoqing Lv, Kaiyuan Zhang, Rongfeng Li, Huanyu Cheng, Lingyun Zhao, Xing Sheng, Milin Zhang, and Lan Yin. A flexible and highly sensitive organic electrochemical transistor-based biosensor for continuous and wireless nitric oxide detection. *Proceedings of the National Academy of Sciences*, 119(34):e2208060119, 2022.

[33] Robin Elo, Staffan Jacobson, and Tomas Kubart. Tailoring residual stresses in crnx films on alumina and silicon deposited by high-power impulse magnetron sputtering. *Surface and Coatings Technology*, 397:125990, 2020.

[34] Aya Ezzelregal. Audio-vestibular findings in pregnancy. 04 2016.

[35] Jiaxin Fan, Carlo Montemagno, and Manisha Gupta. 3D printed high transconductance organic electrochemical transistors on flexible substrates. *Organic Electronics*, 73:122–129, 2019.

[36] Dario Farina, Ken Yoshida, Thomas Stieglitz, and Klaus Peter Koch. Multichannel thin-film electrode for intramuscular electromyographic

recordings. *Journal of Applied Physiology*, 104(3):821–827, 2008. PMID: 18048591.

[37] Andreas Frigg, Andreas Boes, Guanghui Ren, Duk-Yong Choi, Silvio Gees, and Arnan Mitchell. Low stress, anomalous dispersive silicon nitride waveguides fabricated by reactive sputtering. In *2019 Conference on Lasers and Electro-Optics Europe and European Quantum Electronics Conference*, page cep38. Optica Publishing Group, 2019.

[38] Y. Garnier, V. Viel, J.-F. Roussel, and J. Bernard. Low-energy Xenon ion sputtering of ceramics investigated for stationary plasma thrusters. *Journal of Vacuum Science & Technology A*, 17(6):3246–3254, 1999.

[39] Amber Garrett, Brian J. Lithgow, Caroline Gurvich, and Paul Fitzgerald. EVestG™: Responses in depressed patients. In *2008 30th Annual International Conference of the IEEE Engineering in Medicine and Biology Society*, pages 1707–1710, 2008.

[40] James J. Glazier, Alice J. Jiang, Richard J. Crilly, and J.Richard Spears. Laser balloon angioplasty combined with local intracoronary heparin therapy: Immediate and short-term follow-up results. *American Heart Journal*, 134(2):266–273, 1997.

[41] Hua Gong, Adam T. Woolley, and Gregory P. Nordin. High density 3D printed microfluidic valves, pumps, and multiplexers. *Lab Chip*, 16:2450–2458, 2016.

[42] Saman Haghgooie, Brian J Lithgow, Caroline Winograd-Gurvich, and Jayashri Kulkarni. EVestG: a diagnostic measure for schizophrenia. In *30th Annual International IEEE EMBS Conference*, pages 4142–4145, August 2008.

[43] Chao Han, Junfei Huang, Aodi Zhangji, Xufeng Tong, Kaige Yu, Kai Chen, Xinlan Liu, Yang Yang, Yuxin Chen, Waqar Ali Memon, Kamran

Amin, Wanlei Gao, Zexing Deng, Kun Zhou, Yuheng Wang, and Xiangdong Qi. Accelerated skin wound healing using flexible photovoltaic-bioelectrode electrical stimulation. *Micromachines*, 13(4), 2022.

[44] Hany Hassanin, Khamis Essa, Amr Elshaer, Mohamed Imbaby, Heba H. El-Mongy, and Tamer A. El-Sayed. Micro-fabrication of ceramics: Additive manufacturing and conventional technologies. *Journal of Advanced Ceramics*, 10(1):1–27, Feb 2021.

[45] Enhui He, Shengwei Xu, Guihua Xiao, Yuchuan Dai, Xinrong Li, Yilin Song, Fei Gao, Yu Zhang, Shihong Xu, and Xinxia Cai. MWCNTs/PEDOT:PSS nanocomposites-modified microelectrode array for spatial dynamics recording of epileptic discharges in multi-subregion of hippocampal slice. *Sensors and Actuators B: Chemical*, 329:129190, 2021.

[46] Li-Sheng Hsu, Shu-Wei Tung, Che-Hsi Kuo, and Cheng-Wen Ma. Bared microtip arrays for ECG measurement. *International Journal of Automation and Smart Technology*, 6(3), 2016.

[47] Charles W. Hull. Apparatus for production of three dimensional objects by stereolithography, U.S. Patent, No. 4575330, March. 1984.

[48] Nathan Jackson, Arati Sridharan, Sindhu Anand, Michael Baker, Murat Okandan, and Jit Muthuswamy. Long-term neural recordings using MEMS based movable microelectrodes in the brain. *Frontiers in neuroengineering*, 3(10):10, 06 2010.

[49] Jack Judy. Microelectromechanical systems (MEMS): Fabrication, design and applications. *Smart Materials and Structures*, 10:1115–1134, 12 2001.

[50] Amar M. Kamat, Yutao Pei, Bayu Jayawardhana, and Ajay Giri Prakash Kottapalli. Biomimetic soft polymer microstructures and piezoresistive

graphene MEMS sensors using sacrificial metal 3D printing. *ACS Applied Materials & Interfaces*, 13(1):1094–1104, 2021.

[51] R. S. Khandpur. Bioelectrodes: ECG electrodes. *Compendium of Biomedical Instrumentation*, 33:177–182, 2020.

[52] Hong-Lae Kim, Yong-Ho Kim, and Yong-Jun Kim. Miniature electrocardiography sensor using a flexible printed circuit and MEMS technology. In *2008 IEEE International Conference on Multisensor Fusion and Integration for Intelligent Systems*, pages 545–550, 2008.

[53] Stephanie Knowlton, Chu Hsiang Yu, Fulya Ersoy, Sharareh Emadi, Ali Khademhosseini, and Savas Tasoglu. 3D-printed microfluidic chips with patterned, cell-laden hydrogel constructs. *Biofabrication*, 8(2):025019, Jun 2016.

[54] Tom Korsmeyer, Jun Zeng, and Ken Greiner. Design tools for BioMEMS. In *Proceedings Design Automation Conference*, DAC '04, pages 622–628. ACM, 2004.

[55] K. Kavi Krishnaa, B. Muthu Vignesh, and A. Praveen Kumar. A review on DC magnetron sputter deposition over various alloys. *International Journal of Research in Engineering, Science and Management*, 1(11):439–443, Nov 2018.

[56] Ondřej Kylián, Artem Shelemin, Pavel Solař, Pavel Pleskunov, Daniil Nikitin, Anna Kuzminova, Radka Štefaníková, Peter Kúš, Miroslav Cieslar, Jan Hanuš, Andrei Choukourov, and Hynek Biederman. Magnetron sputtering of polymeric targets: From thin films to heterogeneous metal/plasma polymer nanoparticles. *Materials*, 12(15), 2019.

[57] P. Ledochowitsch, R. J. Félus, R. R. Gibboni, A. Miyakawa, S. Bao, and M. M. Maharbiz. Fabrication and testing of a large area, high density, parylene MEMS

Micro-ECoG array. In *2011 IEEE 24th International Conference on Micro Electro Mechanical Systems*, pages 1031–1034, 2011.

[58] Seung Woo Lee, Jong-Mo Seo, Seungmin Ha, Eui Tae Kim, Hum Chung, and Sung June Kim. Development of microelectrode arrays for artificial retinal implants using liquid crystal polymers. *Investigative Ophthalmology & Visual Science*, 50(12):5859–5866, 12 2009.

[59] Tao Li, Zhuo Zhang, Wenyuan Wang, Aijia Mao, Yu Chen, Yan Xiong, and Fei Gao. Simulation and experimental investigation of balloon folding and inserting performance for angioplasty: A comparison of two materials, polyamide-12 and pebax. *Journal of Functional Biomaterials*, 14(6), 2023.

[60] Xinrong Li, Yilin Song, Guihua Xiao, Enhui He, Jingyu Xie, Yuchuan Dai, Yu Xing, Yun Wang, Yiding Wang, Shengwei Xu, Mixia Wang, Tiger H. Tao, and Xinxia Cai. PDMS–parylene hybrid, flexible Micro-ECoG electrode array for spatiotemporal mapping of epileptic electrophysiological activity from multicortical brain regions. *ACS Applied Bio Materials*, 4(11):8013–8022, 2021.

[61] Zong'an Li, Jiquan Yang, Kelou Li, Li Zhu, and Wencheng Tang. Fabrication of PDMS microfluidic devices with 3D wax jetting. *RSC Adv.*, 7:3313–3320, 2017.

[62] B. Lithgow, M. Shoushtarian, and D. Heibert. Electrovestibulogram (EVestG): The Separation of Benign Paroxysmal Positional Vertigo and Meniere's Disease. In *2006 IET 3rd International Conference On Advances in Medical, Signal and Information Processing MEDSIP 2006*, pages 1–4, 2006.

[63] Brian Lithgow. A Methodology for Detecting Field Potentials from the External Ear Canal: NEER and EVestG. *Annals of Biomedical Engineering*, 40(8):1835–1850, 02 2012.

[64] Brian J. Lithgow, Amber Garrett, and Daniel Heibert. EVestG™: A measure for Meniere's Disease. In *2008 30th Annual International Conference of the IEEE Engineering in Medicine and Biology Society*, pages 4162–4165, 2008.

[65] G D Liu, C H Wang, Z L Jia, and K X Wang. An integrative 3D printing method for rapid additive manufacturing of a capacitive force sensor. *Journal of Micromechanics and Microengineering*, 31(6):065005, May 2021.

[66] Giacomo Lorenzin, Lars P. H. Jeurgens, and Claudia Cancellieri. Stress tuning in sputter-grown Cu and W films for Cu/W nanomultilayer design. *Journal of Applied Physics*, 131(22):225304, 2022.

[67] Matteo Massetti, Silan Zhang, Harikesh Padinare, Bernhard Burtscher, Chiara Diacci, Daniel T. Simon, Xianjie Liu, Mats Fahlman, Deyu Tu, Magnus Berggren, and Simone Fabiano. Fully 3D-printed organic electrochemical transistors, 2022.

[68] Dakurah Mathias, Jaesoon Park, Eungbo Kim, and Yeun-Ho Joung. Development of a novel noncontact ECG electrode by MEMS fabrication process. *Transactions on Electrical and Electronic Materials*, 17:150–154, 06 2016.

[69] S. Misumi, A. Okada, Y. Okamoto, and M. Inoue. Fundamental study on sputter deposition of ceramic film by large-area electron beam irradiation. *Procedia CIRP*, 6:486–491, 2013. Proceedings of the Seventeenth CIRP Conference on Electro Physical and Chemical Machining (ISEM).

[70] J. Musil and J. Vlček. Magnetron sputtering of alloy and alloy-based films. *Thin Solid Films*, 343-344:47–50, 1999.

[71] Balasubramanian Nagarajan, Zhiheng Hu, Xu Song, Wei Zhai, and Jun Wei.

Development of micro selective laser melting: The state of the art and future perspectives. *Engineering*, 5(4):702–720, 2019.

[72] René Packard, Yuan Luo, Parinaz Abiri, Nelson Jen, Olcay Aksoy, William Suh, Yu-Chong Tai, and Tzung Hsiai. 3-D electrochemical impedance spectroscopy mapping of arteries to detect metabolically active but angiographically invisible atherosclerotic lesions. *Theranostics*, 7(9):2431–2442, 06 2017.

[73] René Packard, Xiaoxiao Zhang, Yuan Luo, Teng Ma, Nelson Jen, Jianguo Ma, Linda Demer, Qifa Zhou, James Sayre, Rongsong Li, Yu-Chong Tai, and Tzung Hsiai. Two-point stretchable electrode array for endoluminal electrochemical impedance spectroscopy measurements of lipid-laden atherosclerotic plaques. *Annals of Biomedical Engineering*, 44(9):2695–2706, 02 2016.

[74] Sai Krishna Padamata, Andrey Yasinskiy, Valentin Yanov, and Gudrun Saevarsdottir. Magnetron sputtering high-entropy alloy coatings: A mini-review. *Metals*, 12:319, 02 2022.

[75] D. Padmaraj, Wanda Zagozdzon-Wosik, Lei-Ming Xie, D. Pijanowka, John Miller, Piotr Grabiec, and Jarek Wosik. BioMEMS for mitochondria medicine. *TechConnect Briefs*, 1:464–467, May 2009.

[76] Simone Pagliano, David E. Marschner, Damien Maillard, Nils Ehrmann, Göran Stemme, Stefan Braun, Luis Guillermo Villanueva, and Frank Niklaus. Micro 3D printing of a functional MEMS accelerometer. *Microsystems & Nanoengineering*, 8(1):105–126, Sep 2022.

[77] Oliver Paul, João Gaspar, and Patrick Ruther. Advanced silicon microstructures, sensors, and systems. *IEEJ Transactions on Electrical and Electronic Engineering*, 2:199 – 215, 05 2007.

[78] Shuo Qu, Junhao Ding, Jin Fu, Mingwang Fu, Baicheng Zhang, and Xu Song. High-precision laser powder bed fusion processing of pure copper. *Additive Manufacturing*, 48:102417, 2021.

[79] Swaminathan Rajaraman, Julian A Bragg, James D Ross, and Mark G Allen. Micromachined three-dimensional electrode arrays for transcutaneous nerve tracking. *Journal of Micromechanics and Microengineering*, 21(8):085014, Jun 2011.

[80] Nilabh Roy, Dipankar Behera, Obehi Dibua, Chee Foong, and Michael Cullinan. A novel microscale selective laser sintering (micro-SLS) process for the fabrication of microelectronic parts. *Microsystems & Nanoengineering*, 5(1):64, 12 2019.

[81] Birthe Rubehn, Conrado Bosman, Robert Oostenveld, Pascal Fries, and Thomas Stieglitz. A MEMS-based flexible multichannel ECoG-electrode array. *Journal of Neural Engineering*, 6(3):036003, May 2009.

[82] Farhad Sadeghi and David Le. Characterization of polymeric biomedical balloon: physical and mechanical properties. *Journal of Polymer Engineering*, 41(9):799–807, 2021.

[83] E Seker, Jong Hwan Sung, M. L Shuler, and M. L Yarmush. Solving medical problems with BioMEMS. *IEEE pulse*, 2(6):51–59, 2011.

[84] M.A. Signore, A. Sytchkova, D. Dimaio, A. Cappello, and A. Rizzo. Deposition of silicon nitride thin films by RF magnetron sputtering: a material and growth process study. *Optical Materials*, 34(4):632–638, 2012.

[85] Ramin Soltanzadeh, Elnaz Afsharipour, Neda Anssari, Behzad Mansouri, and Cyrus Shafai. Structural and performance comparison between SU-8

microfabricated and 3D-printed microneedle electrodes. *Journal of 3D Printing in Medicine*, 4(1):29–44, 2020.

[86] George D. Spyropoulos, Jennifer N. Gelinas, and Dion Khodagholy. Internal ion-gated organic electrochemical transistor: A building block for integrated bioelectronics. *Science Advances*, 5(2):eaau7378, 2019.

[87] Thomas Stieglitz and Matthias Gross. Flexible BIOMEMS with electrode arrangements on front and back side as key component in neural prostheses and biohybrid systems. *Sensors and Actuators B: Chemical*, 83(1):8–14, 2002. Selected Papers from TRANSDUCERS '01 EUROSENSORS XV.

[88] Abdelbaset Suleiman, Brian Lithgow, Behzad Mansouri, and Zahra Moussavi. Investigating the validity and reliability of electrovestibulography (EVestG) for detecting post-concussion syndrome (PCS) with and without comorbid depression. *Scientific Reports*, 8(1):1–11, 09 2018.

[89] Abdelbaset Suleiman, Brian Lithgow, Behzad Mansouri, and Zahra Moussavi. Using EVestG assessments for detection of symptomology consequent to a lateral-impact concussion. *Journal of Medical and Biological Engineering*, 39(2):218–223, 04 2019.

[90] Paul Tabet, Ahlem Elblidi, and Issam Saliba. Vestibular Migraine versus Ménière's Disease: Diagnostic Utility of Electrocochleography. *Audiology Research*, 13(1):12–22, 2023.

[91] James Teena, Manu Sebastian Mannoor, and Dentcho Ivanov. BioMEMS—advancing the frontiers of medicine. *Sensors*, 8(9):6077–6107, 09 2008.

[92] Kwok Siong TEH. Additive direct-write microfabrication for MEMS: A review. *Frontiers of Mechanical Engineering*, 12(4):490–509, 2017.

[93] Sanitta Thongpang, Thomas Richner, Sarah Brodnick, Amelia Schendel, Jiwan Kim, Adam Wilson, Joseph Hippensteel, Lisa Krugner-Higby, Dan Moran, Azam Ahmed, David Neimann, Karl Sillay, and Justin Williams. A micro electrocorticography platform and deployment strategies for chronic BCI applications. *Clinical EEG and neuroscience : official journal of the EEG and Clinical Neuroscience Society (ENCS)*, 42(4):259–265, 10 2011.

[94] A M Tothill, M Partridge, S W James, and R P Tatam. Fabrication and optimisation of a fused filament 3D-printed microfluidic platform. *Journal of Micromechanics and Microengineering*, 27(3):035018, Feb 2017.

[95] Kevin C. Tseng, Bor-Shyh Lin, Lun-De Liao, Yu-Te Wang, and Yu-Lin Wang. Development of a wearable mobile electrocardiogram monitoring system by using novel dry foam electrodes. *IEEE Systems Journal*, 8(3):900–906, 2014.

[96] Kevin Vittayarukskul and Abraham Phillip Lee. A truly lego®-like modular microfluidics platform. *Journal of Micromechanics and Microengineering*, 27(3):035004, Jan 2017.

[97] I-Jan Wang, Lun-De Liao, Yu-Te Wang, Chi-Yu Chen, Bor-Shyh Lin, Shao-Wei Lu, and Chin-Teng Lin. A wearable mobile electrocardiogram measurement device with novel dry polymer-based electrodes. In *TENCON 2010 2010 IEEE Region 10 Conference*, pages 379–384, 2010.

[98] Long-Fei Wang, Jing-Quan Liu, Hui-Ling Peng, Bin Yang, Hong-Ying Zhu, and Chun-Sheng Yang. MEMS-based flexible capacitive electrode for ECG measurement. *Electronics Letters*, 49(12):739–740, 2013.

[99] Long-Fei Wang, Jingquan Liu, Xiao-Xiao Yan, Bin Yang, and Chun-Sheng Yang. A MEMS-based pyramid micro-needle electrode for long-term EEG measurement. *Microsystem Technologies*, 19, 02 2012.

[100] Yanjie Wang, Hualing Chen, Jiayu Liu, Zicai Zhu, Longfei Chang, Dichen Li, and Shuhai Jia. Aided manufacturing techniques and applications in optics and manipulation for ionic polymer-metal composites as soft sensors and actuators. *Journal of Polymer Engineering*, 35(7):611–626, 2015.

[101] Zongjie Wang, Raafa Abdulla, Benjamin Parker, Roya Samanipour, Sanjoy Ghosh, and Keekyoung Kim. A simple and high-resolution stereolithography-based 3D bioprinting system using visible light crosslinkable bioinks. *Biofabrication*, 7(4):045009, Dec 2015.

[102] C. Wu, Di Chen, R.-J Hu, Jingdong Chen, X. Chen, X.-W Wang, and B.-L Lü. Fabrication of dry electroencephalography electrode using flexible substrate MEMS technique. *Shanghai Jiaotong Daxue Xuebao/Journal of Shanghai Jiaotong University*, 45:1035–1040, 07 2011.

[103] Chenglai Xin, Wenbo Liu, Ning Li, Jiazhen Yan, and Sanqiang Shi. Metallization of Al_2O_3 ceramic by magnetron sputtering Ti/Mo bilayer thin films for robust brazing to kovar alloy. *Ceramics International*, 42, 03 2016.

[104] L. M. Yu, Francis E. H. Tay, D. G. Guo, L. Xu, M. N. Nyan, F. W. Chong, K. L. Yap, and B. Xu. A MEMS-based bioelectrode for ECG measurement. In *SENSORS, 2008 IEEE*, pages 1068–1071, 2008.

[105] Tao Yuan, Di Chen, Jingdong Chen, Xiang Chen, Xiaowei Wang, and Baoliang Lu. A novel MEMS elastic-based dry electrode for electroencephalography measurement. *Microsystem Technologies*, 20(6):1125–1129, 06 2014.

[106] Arash Zargaran Yazd. Improvement of longevity and signal quality in implantable neural recording systems. Master's thesis, University of British Columbia, 2008.

[107] ANDREY ZDANOVICH. BIOMEMS glucose sensors. Master of applied sciences, School of Graduate Studies, McMaster University, Hamilton, Ontario, Canada, June 2010.

[108] Jinjin Zhang, Luyang Wei, Xiuxia Meng, Fangyong Yu, Naitao Yang, and Shaomin Liu. Digital light processing-stereolithography three-dimensional printing of yttria-stabilized zirconia. *Ceramics International*, 46(7):8745–8753, 2020.

[109] Pinwei Zhu. Design of surface electromyography detection circuit. In *2010 International Conference on Future Information Technology and Management Engineering*, volume 1, pages 459–462, 2010.

[110] Zheng Han Zhu, Jing Quan Liu, Yue Feng Rui, and Chun Sheng Yang. A research on implantable microelectrodes for EMG signal acquisition. In *MEMS/NEMS Nano Technology*, volume 483 of *Key Engineering Materials*, pages 387–391. Trans Tech Publications Ltd, 11 2011.

[111] Muneeb Zia, Bryce Chung, Samuel Sober, and Muhannad S. Bakir. Flexible multielectrode arrays with 2-D and 3-D contacts for *in vivo* electromyography recording. *IEEE Transactions on Components, Packaging and Manufacturing Technology*, 10(2):197–202, 2020.

[112] Muneeb Zia, Bryce Chung, Samuel J. Sober, and Muhannad S. Bakir. Fabrication and characterization of 3D multi-electrode array on flexible substrate for in vivo EMG recording from expiratory muscle of songbird. In *2018 IEEE International Electron Devices Meeting (IEDM)*, pages 29.4.1–29.4.4, 2018.